

Electrical and Mechanical Design Principle of  
Self-Healing Metal Interconnect and  
Its Application for Flexible Device

自己修復型金属配線の電氣的・機械的  
設計原理とフレキシブルデバイスへの応用

February 2019

Tomoya KOSHI

古志 知也



Electrical and Mechanical Design Principle of  
Self-Healing Metal Interconnect and  
Its Application for Flexible Device

自己修復型金属配線の電氣的・機械的  
設計原理とフレキシブルデバイスへの応用

February 2019

Research on Micro and Nano Mechanics  
Department of Applied Mechanics  
Graduate School of Fundamental Science and Engineering  
Waseda University

Tomoya KOSHI

古志 知也



# Contents

Chapter 1	General Introduction .....	1
1.1	Background .....	1
1.1.1	Flexible Devices .....	1
1.1.2	Bendability and Stretchability .....	2
1.2	Previous Studies.....	2
1.2.1	Ultrathin Devices with Out-of-Plane Wrinkle Structure.....	2
1.2.2	Elastic Conductors as Conductive Interconnects.....	4
1.2.3	Wave-Shaped Metal Interconnects .....	7
1.2.4	Self-Healing Ability of Broken Conductive Interconnects.....	7
1.2.5	Comparison of Previous Approaches.....	9
1.3	Objective.....	11
1.4	Thesis Structure .....	12
Chapter 2	Nanoparticle Chain Formation using Dielectrophoresis.....	14
2.1	Introduction.....	14
2.2	Theoretical Analysis.....	15
2.2.1	Trapping Process .....	15
2.2.2	Bridging Process.....	17
2.3	Observation of Nanoparticle Chain Formation.....	19
2.3.1	Fabrication.....	19
2.3.2	Observation Setup.....	20
2.3.3	Results and Discussion .....	21
2.4	Measurement of Maximum Allowable Current and Resistance of Nanoparticle chain .....	25

---

*Contents*

---

2.4.1	Measurement Setup .....	26
2.4.2	Results and Discussion .....	27
2.5	Measurement of Forming Time.....	30
2.5.1	Measurement Setup .....	31
2.5.2	Results and Discussion .....	31
2.6	Summary .....	32
<b>Chapter 3</b>	<b>Crack Configuration of Metal Interconnect.....</b>	<b>34</b>
3.1	Introduction.....	34
3.2	Theoretical Analysis.....	35
3.2.1	Theoretical Calculation.....	35
3.2.2	Relationship between Elongation Stiffness Ratio and Crack Configuration in Previous Studies.....	39
3.3	Observation of Crack Configuration Transition.....	39
3.3.1	Fabrication.....	40
3.3.2	Observation Setup.....	41
3.3.3	Results and Discussions.....	41
3.4	Measurement of Crack Width and Breaking Elongation .....	47
3.4.1	Fabrication.....	47
3.4.2	Measurement Setup .....	49
3.4.3	Results and Discussion .....	49
3.5	Summary .....	50
<b>Chapter 4</b>	<b>Flexible Device using Self-Healing Metal Interconnect.....</b>	<b>52</b>
4.1	Introduction.....	52
4.2	Healing Property Evaluation under Cyclic Stretching Deformation.....	53
4.2.1	Design.....	54
4.2.2	Fabrication.....	54
4.2.3	Measurement Setup .....	55
4.2.4	Results and Discussion .....	58

4.3	Demonstration of Flexible Device using Self-Healing Metal Interconnect .....	60
4.3.1	Design.....	61
4.3.2	Fabrication.....	63
4.3.3	Measurement Setup .....	65
4.3.4	Results and Discussion .....	66
4.4	Summary.....	66
Chapter 5	Conclusion .....	68
5.1	Overall Summary .....	68
5.2	Future Prospect .....	71
Appendix A	Fabrication Process .....	73
Appendix B	Materials and Equipment .....	80
Appendix C	Embodiment Informatics .....	85
References.....		87
Achievements.....		97
Acknowledgements .....		102





# Chapter 1      General Introduction

## 1.1      Background

---

### 1.1.1      Flexible Devices

Flexible devices such as displays [1]–[5], sensor array sheets [6]–[10], photovoltaic sheets [11]–[16], and batteries [17]–[22] have been actively studied recently [23]–[35]. The features of flexible devices include lightweight, thinness, and mechanical bendability/stretchability. Because of these properties, flexible devices that can adhere to the human skin for bio-information sensing [36]–[44] have been of great interest in realizing comfortable healthcare monitoring systems. The previous studies on flexible devices have reported that these devices lack stretchability, but exhibit bendability. Devices that only exhibit bendability can be used on cylinder-shaped surfaces such as the human tibia; however, bio-information sensing is performed on most areas of the human body that have complex shapes such as a free-form surface or a constant compression or stretching deformation. Therefore, flexible devices require both stretchability and bendability for sensing bio-information in a stable manner.

### 1.1.2 Bendability and Stretchability

A key point related to flexible devices is how they achieve bendability and stretchability while maintaining their original performance and function as measurement devices. In comparison to achieving the stretchability for flexible devices, bendability is considerably easier to achieve. From the viewpoint of the mechanics of materials, in a bending deformation, a flexible device experiences compression stress on one side of a neutral axis and stretching stress on the other side. The stresses caused in the device increase with an increase in the device thickness, and therefore, flexible devices can be made bendable by decreasing their thickness. On the other hand, in stretching deformation, a flexible device experiences stretching stresses throughout its entire structure. In this case, decreasing the device thickness cannot decrease the stress; hence, other approaches are necessary to achieve stretchability.

## 1.2 Previous Studies

---

Approaches presented in previous studies to achieve stretchability in flexible devices can be classified into three categories: ultrathin devices with an out-of-plane wrinkle structure [45]–[48], devices using an elastic conductor as an interconnect [4], [49]–[51], and devices using wave-shaped metal interconnects [52]–[56]. In previous studies, electronic components were electrically and mechanically connected with conductive interconnects on a thin and bendable/stretchable substrate such as polyethylene terephthalate (PET), polyethylene naphthalate (PEN), polydimethylsiloxane (PDMS), polyurethane (PU), or acrylic foam (AF). These approaches were adopted to develop new stretchable materials or stretchable structures for devices to achieve stretchability. In addition to these three approaches, some research groups proposed a new approach: providing a self-healing ability for a broken conductive interconnect [57]–[62]. Some remarkable previous studies on device stretchability are described below.

### 1.2.1 Ultrathin Devices with Out-of-Plane Wrinkle Structure

During the fabrication of ultrathin devices with an out-of-plane wrinkle structure, both thin (several tens to several hundreds of nanometers in thickness) conductive interconnects and electronic components are formed on a thin flexible substrate such as PEN [47] or parylene-C [45] (approximately 1  $\mu\text{m}$  thick). Then,

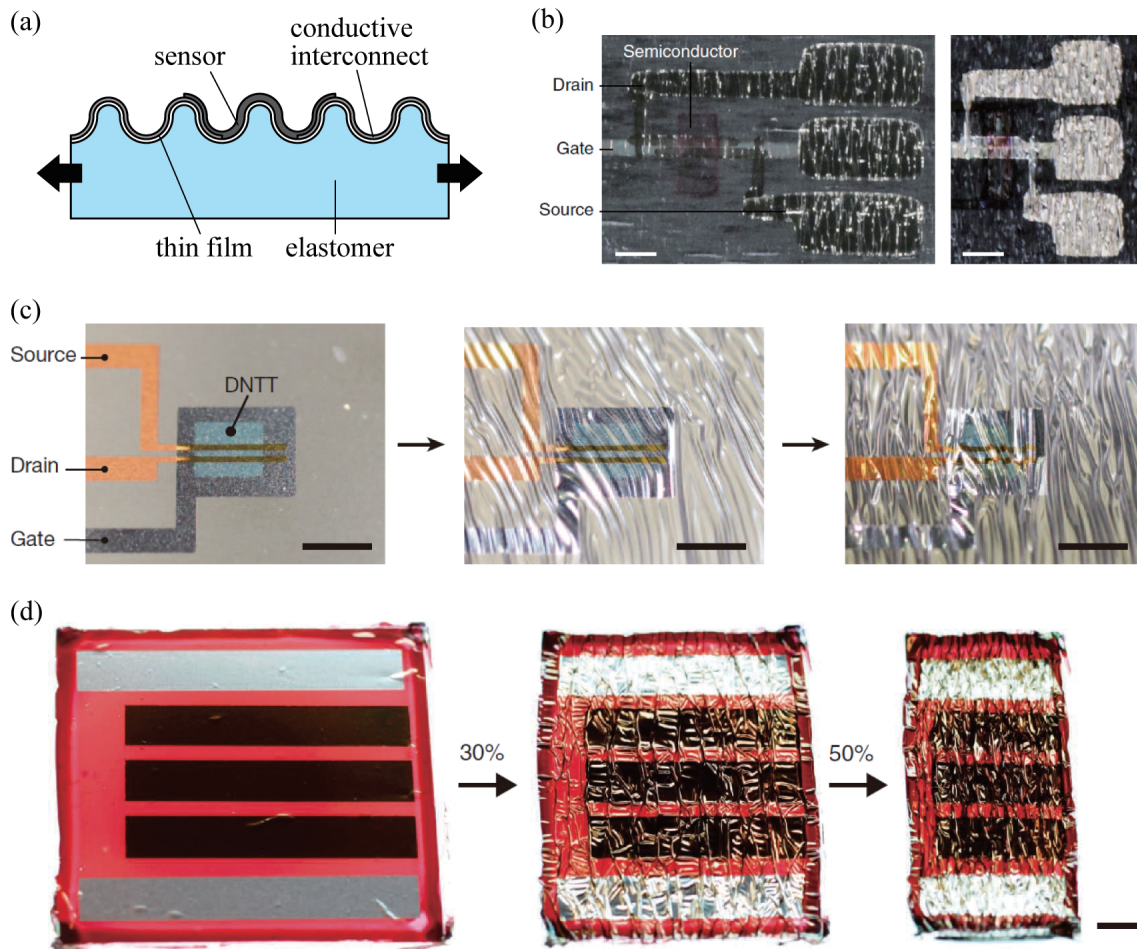


Figure 1.1 Schematic illustration and optical images of ultrathin devices with out-of-plane wrinkle structure: (a) cross-sectional view of devices, (b) printed flexible transistor (scale bars, 1 mm) [45], (c) flexible transistor using dinaphtho thieno thiophene (DNTT) as gate dielectric (scale bars, 1 mm) [47], and (d) organic solar cell (scale bar, 2 mm) [14].

the fabricated device is laminated to a prestretched elastomer such as an AF adhesive tape. When the prestrain in the AF tape is released, an out-of-plane wrinkle is formed on the device, as shown in Figure 1.1a. The out-of-plane wrinkle enables the device to be stretchable. To form the wrinkle structure, the conductive interconnects and electronic components must be thin and bendable; hence, organic-material-based electronic components such as organic light-emitting diodes (OLEDs) and organic field-effect transistors (OFETs) are used as shown in Figures 1.1b–d. The organic-material-based electronic components can be formed on a substrate through a relatively simple fabrication process (e.g., coating or

inkjet printing) and they themselves have bendability. Hence, large-area and lightweight OLEDs and OFETs are expected to be available at low costs in the future. For thin conductive interconnects, evaporated thin metals or printed metal conductive inks are used. The optical images in Figure 1.1b show electronic circuits in a fabricated device that are based on organic materials composed of conductive interconnects of Ag nanoparticle ink and OFETs ( $1.0 \text{ cm}^2/\text{Vs}$ ) on  $1\text{-}\mu\text{m}$ -thick parylene-C films, as reported by Fukuda *et al.* [45]. The devices were fabricated using inkjet printing, and the total thickness of the device was less than  $2 \mu\text{m}$ . Hence, the device can adhere to the human skin without an adhesive. However, the performance and life span of organic-material-based electronic components are inferior to that of components composed of inorganic materials. Therefore, various studies are ongoing to improve the performance of organic materials.

### 1.2.2 Elastic Conductors as Conductive Interconnects

In this approach, stretchable devices can be realized by connecting each rigid electronic component with stretchable conductive interconnects on a stretchable substrate. That is, even if the components are not stretchable (but rigid and relatively small), a device can be made stretchable on the whole when its components are connected using stretchable conductive interconnects. Commercial electronic components, including chip-mounted LEDs and transistors, are already small, and therefore, they are used in some stretchable devices; previous studies have focused on stretchable conductive interconnects. Current mainstream implementations are as follows: elastic conductors as conductive interconnects composed of nonconductive elastomers and carbon nanotubes [4] or metal nanowires/flakes [49], [50], and wave-shaped metal interconnect using the deformation of the wave shape [52]–[56].

Figure 1.2 shows some devices that use elastic conductors. Sekitani *et al.* reported on a printable elastic conductor that was a mixture of an elastomer and single-walled carbon nanotubes (SWNTs) [4]. They authors fabricated stretchable conductive interconnects by printing them on a PDMS substrate. The conductivity and stretchability were determined by the proportion of the elastomer and the SWNTs. A stretchability of more than 100% and conductivity of  $10^3 \text{ S/m}$  were achieved when the proportion of the SWNTs was as low as 1.4%, while a stretchability of more than 20% and conductivity of  $10^4 \text{ S/m}$  were observed when the proportion of the SWNTs was increased to 15.8%. Matsuhisa *et al.* reported on a stretchable conductive interconnect with conductivities of  $4.0 \times 10^5 \text{ S/m}$  before stretching, and  $9.4 \times 10^4$

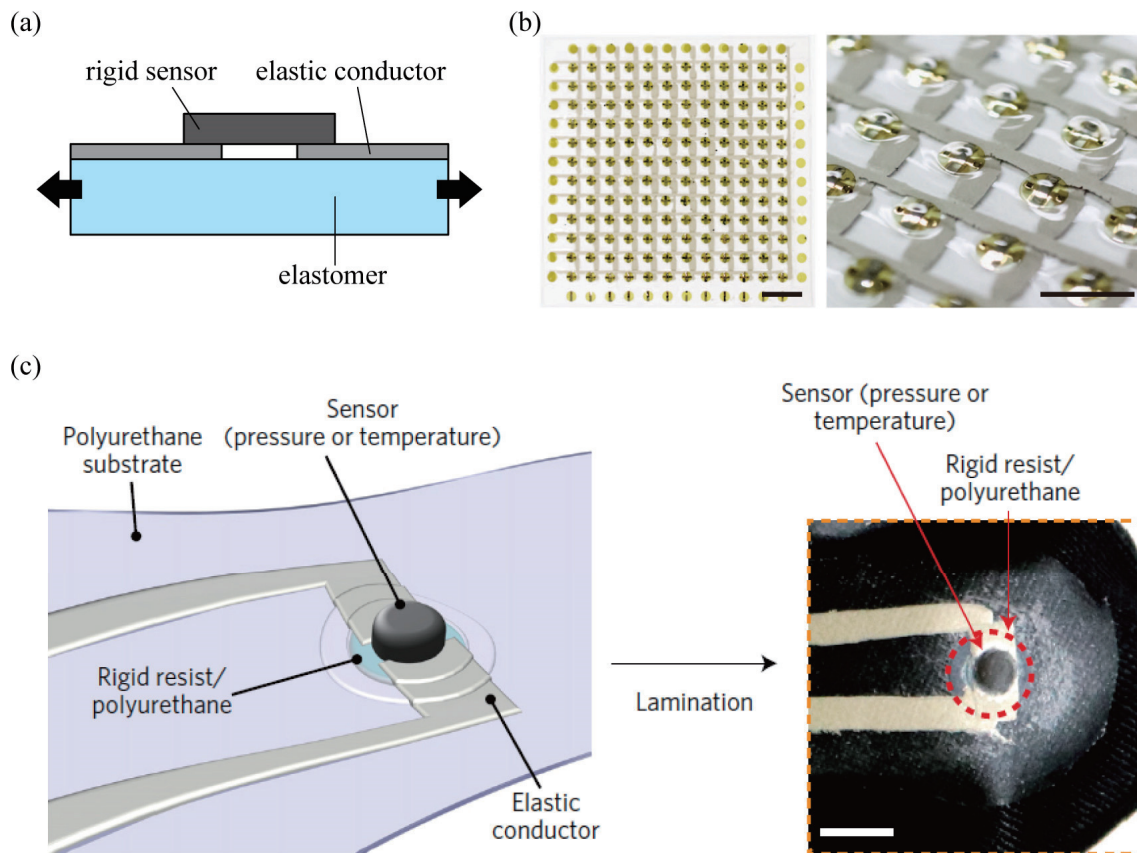


Figure 1.2 Schematic illustration and optical images of devices using elastic conductors and rigid electronic components: (a) cross-sectional view of the device, (b) stretchable organic thin-film transistor matrix (scale bars, 5 mm) [50], and (c) stretchable and fully printed sensor (scale bar, 5 mm) [49].

S/m when stretched to 400% strain, by printing a conductive ink material that was a combination of fluorinated elastomer, silver flake, and surfactant [49]. This conductive interconnect achieved the best conductivity and stretchability among various elastic conductors in 2017. However, its conductivity was  $10^2$  lower compared with the conductivities of metals (for example, the electrical conductivity of copper is  $5.9 \times 10^7$  S/m).

The approach using a combination of elastic conductors and rigid electronic components is similar to an approach called flexible hybrid electronics, which has also been developed in recent years. This approach aims to achieve a quicker realization of flexible devices by combining the advantages of organic materials technology (such as printable conductive interconnects and antennas) and conventional

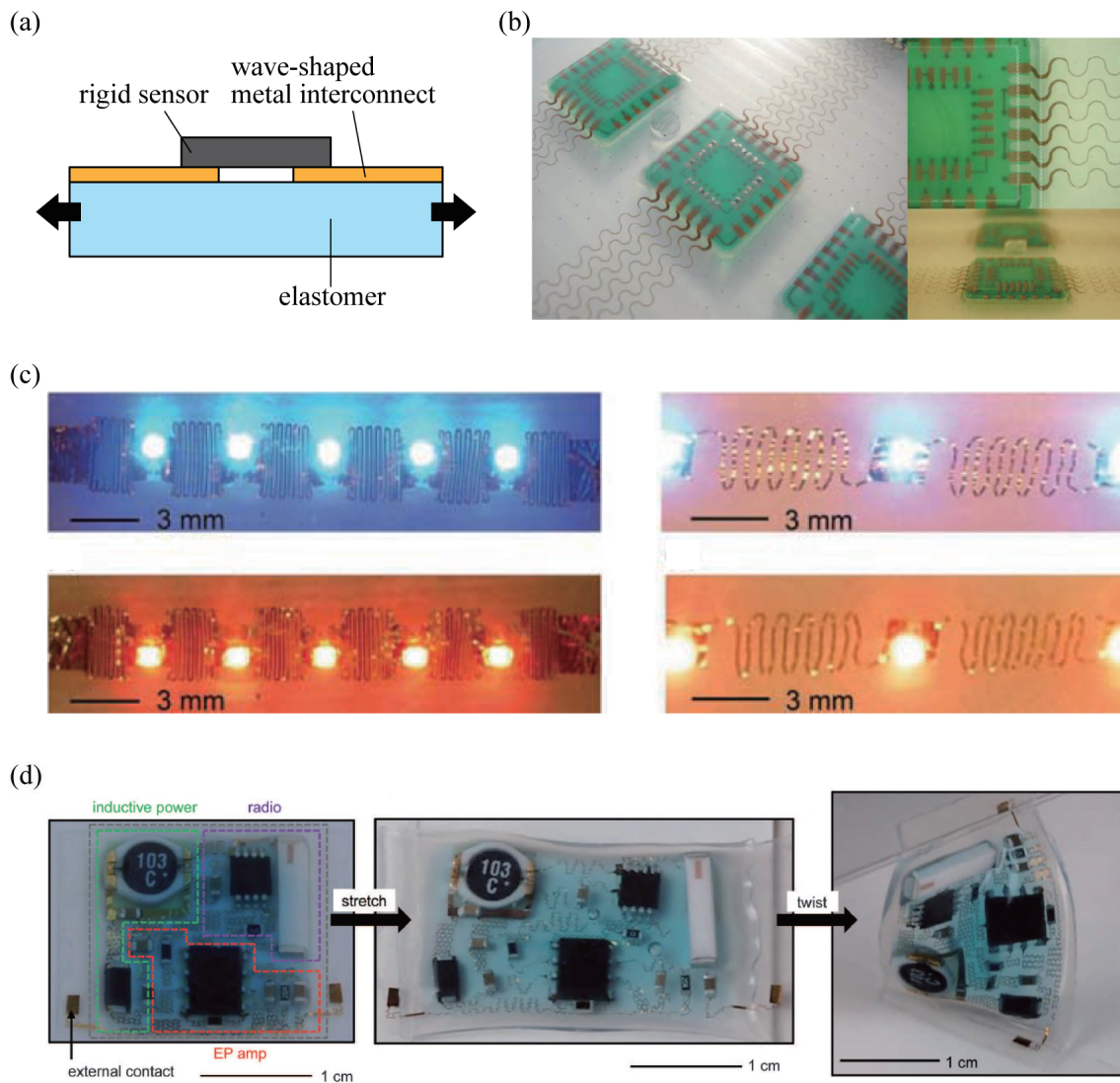


Figure 1.3 Schematic illustration and optical images of devices using wave-shaped metal interconnect and rigid electronic components: (a) cross-sectional view of the device, (b) wave-shaped copper interconnects and functional islands [54], (c) stretchable LED array on ecoflex substrate [5], and (d) soft stretchable electronic system in thin elastomeric microfluidic enclosure [56].

inorganic materials technology (such as silicon integrated circuit chips and microelectromechanical systems (MEMS) sensor chips). In 2015, the Flexible Hybrid Electronics Manufacturing Innovation Institute was established in the United States to study flexible hybrid electronics. A total of 162 companies and universities from around the world participate in this consortium.

### 1.2.3 Wave-Shaped Metal Interconnects

Similar to devices using elastic conductors, in this approach, each rigid electronic component is connected to a wave-shaped metal interconnect to achieve stretchability, as shown in Figure 1.3a. For example, Gray *et al.* reported on gold interconnects embedded in a PDMS sheet that were curved into the shape of a sine wave [53]. They reported that the maximum stretchability of the interconnects was determined by the interconnect width, thickness, and amplitude of the sine wave shape. Stretchability was slightly lower than 60% at maximum. In addition, electrical conductivity was extremely high at  $4.6 \times 10^7$  S/m, because gold was used as the material. Jones *et al.* also fabricated out-of-plane wave-shaped (wrinkled) gold interconnects on a stretchable substrate by evaporating 25-nm-thick gold on a PDMS substrate, which was prestretched by 15% [55]. No breaking was found in the interconnects after 100 cycles of repeated stretching/compression deformation with a strain ranging from 0% to 15%. However, breaking was detected when a 25% strain was added to the interconnects. Kim *et al.* fabricated wave-shaped metal interconnects composed of a gold layer and polyimide layers [52]. The interconnect used out-of-plate deformation for stretching, and the authors reported that the maximum stretchability of the interconnect varied depending on Young's modulus of the PDMS that sealed the device. No interconnect breakages were found, even under a 110% elongation, when the device was sealed with a precured PDMS. In general, wave-shaped metal conductors have extremely high conductivity; however, the maximum stretchability is lower than that of elastic conductors. In addition, wave-shaped metal conductors are easily cracked and finally lose their conductivity because of cyclical deformation.

### 1.2.4 Self-Healing Ability of Broken Conductive Interconnects

The above three approaches focused on developing new materials or new structures to achieve stretchability. In contrast, an approach providing a new ability (the self-healing ability of broken conductive interconnect) has been proposed [57], as shown in Figure 1.4. For instance, self-healing elastic conductors using self-healing polymers [58], self-healing metal interconnect using microcapsules of liquid metal [59], and self-healing metal interconnect using dielectrophoresis of metal nanoparticles [60]–[62] have been reported. A self-healing elastic conductor using a self-healing polymer was composed of a self-healing polymer and nickel nanostructured microparticles. The conductivity varied depending on the mixing rate of the self-healing polymer and the nickel nanostructured microparticles, and the maximum conductivity was  $4.0 \times 10^3$  S/m. This conductivity was considerably lower than that of the metal

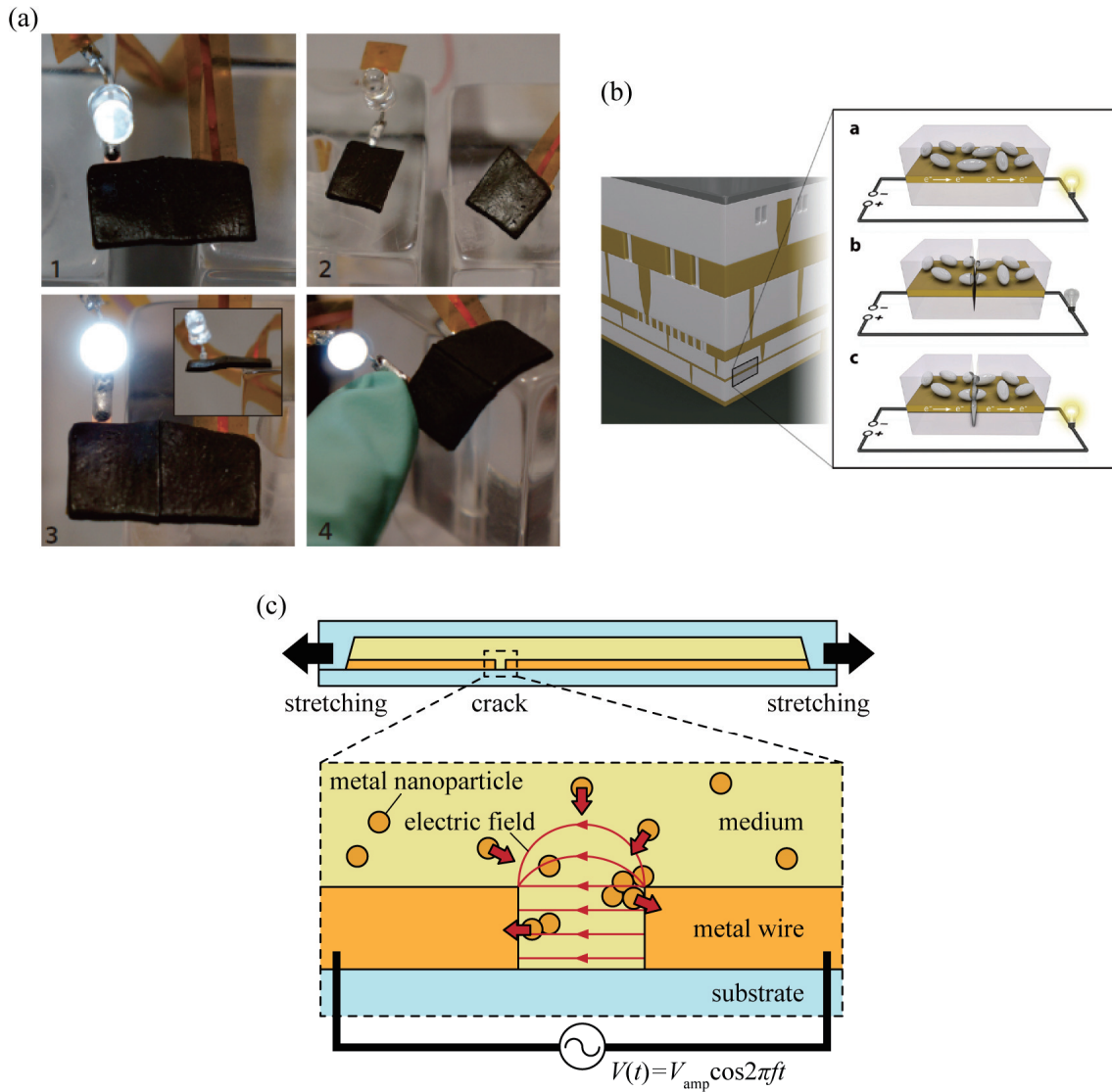


Figure 1.4 Conductive interconnects with self-healing ability: (a) self-healing elastic conductors using self-healing polymers [57], (b) self-healing metal interconnect using microcapsules of liquid metal [59], and (c) self-healing metal interconnect using dielectrophoresis of metal nanoparticles [60]–[62].

interconnect. Moreover, a self-healing polymer cannot heal without contact with the broken point because the polymer uses physical molecular reconnection on the surfaces of the breaks for self-healing. In the case of self-healing metal interconnect using the microcapsules of liquid metal, metal interconnects are covered with the microcapsules of gallium-indium (Ga-In) liquid metal. When the metal interconnect



cracks, the microcapsules release Ga-In liquid metal into the crack. The metal interconnect regains its conductivity with nearly full recovery of conductivity at less than 1 ms after damage; however, when the healed point is broken again, the metal interconnect cannot recover conductivity again because the microcapsules can release the Ga-In liquid metal only once. In the case of self-healing metal interconnect using the dielectrophoresis of metal nanoparticles reported by Koshi *et al.*, metal interconnects on a substrate are covered with metal nanoparticle dispersion in the device. When one of the interconnects is cracked and completely loses its conductivity by deformation, a voltage is applied to the interconnect and an electric field is generated only around the crack. The nanoparticles near the crack experience a dielectrophoretic force caused by the electric field, and the nanoparticles are trapped in the crack. The trapped nanoparticles form chain structures in the crack and the nanoparticle chains bridge the crack. Thus, the broken interconnect regains its conductivity again on the application of voltage to the interconnect. The self-healing ability obtained thus using the dielectrophoresis of metal nanoparticles can realize high conductivity and healing without contact with the broken section. In addition, even if the healed point is broken again, the interconnect can recover its conductivity any number of times because the nanoparticles around the broken point are trapped and bridge the broken point on the application of voltage to the interconnect. Hence, the self-healing ability obtained using the dielectrophoresis of metal nanoparticles has several advantages compared with the self-healing abilities obtained using the other two approaches.

### 1.2.5 Comparison of Previous Approaches

Table 1.1 lists a comparison of the three major approaches and the approach adopted to obtain the self-healing ability using the dielectrophoresis of metal nanoparticles in terms of the stretchability and performance of a flexible device. As can be seen in Table 1.1, the performance is further classified into two parameters: the conductivity of interconnects and the performance of electronic components. In the case of ultrathin devices with an out-of-plane wrinkle structure, the performance of electronic components is lower than that of devices using a combination of stretchable conductive interconnects and rigid electronic components, because the components use organic-based materials. On the other hand, devices using a combination of stretchable conductive interconnects and rigid electronic components perform better because of their inorganic-based electronic components. However, elastic conductors as conductive interconnects exhibit lower conductivity than metal interconnects, and wave-shaped metal interconnects show lower stretchability than elastic conductors. In contrast, metal interconnects with self-healing ability can achieve high stretchability, high conductivity, and high performance; hence, flexible devices using

Table 1.1 Comparison of three major approaches and self-healing ability using dielectrophoresis of metal nanoparticles to achieve stretchability of flexible devices (✓: not bad, ✓✓: good, ✓✓✓: excellent).

device structure		stretchability	performance	
			conductivity of interconnect	sensitivity of sensor
ultrathin devices with out-of-plane wrinkle structure [45]–[48]		✓ good for cyclic stretching	✓✓ metal ink or metal $10^6$ – $10^7$ S/m	✓ organic semiconductor
rigid sensor and stretchable conductor	elastic conductor as conductive interconnect [4], [49]–[51]	✓✓✓ good for cyclic stretching	✓ organic material $10^5$ S/m	✓✓✓ inorganic semiconductor
	wave-shaped metal interconnect [52]–[56]	✓ easily cracked	✓✓✓ metal $10^7$ S/m	✓✓✓ inorganic semiconductor
	metal interconnect with self-healing ability [60]–[62]	✓✓✓ self-healing ability of crack	✓✓✓ metal $10^7$ S/m	✓✓✓ inorganic semiconductor

self-healing metal interconnects offer several advantages. However, applying self-healing metal interconnects to flexible devices remains a significant challenge (details are described in Section 1.3). At present, flexible devices that combine high stretchability and high performance have not been achieved.

### 1.3 Objective

---

The objective of this research is to identify the fundamental design principles of self-healing metal interconnects and to develop a flexible device using self-healing metal interconnects based on the design principles identified. The key points to be considered when applying the self-healing metal interconnect to flexible devices are as follows: understanding the conditions forming a nanoparticle chain using dielectrophoresis, and understanding the factors determining the number of cracks and crack widths caused in the metal interconnect. In previous studies, a decrease in the impedance of a metal interconnect broken with a single small crack was experimentally verified [60]–[62]. The studies reported that a nanoparticle chain was successfully formed in a crack up to 4  $\mu\text{m}$  wide when a voltage of approximately 4 V was applied. However, when the crack width was 4  $\mu\text{m}$  or greater, a nanoparticle chain was not formed in the crack, and the broken interconnect was not healed. That is, the self-healing ability obtained using dielectrophoresis of metal nanoparticles has a limit with regard to the healable crack width. In experiments, a single small crack was intentionally prepatterned in a metal interconnect on a glass substrate by a micromachining process as an initial step to verify self-healing. In previous studies on flexible devices, cracks caused in a metal interconnect on a stretchable substrate by bending or stretching deformation displayed different crack configurations. For example, many smaller cracks (several submicrometers to micrometers in width) were caused in a metal interconnect in some studies, and a single larger crack (several tens of micrometers to hundreds of micrometers) was caused in a metal interconnect in other studies. In the former case, it is considered that a much higher applied voltage is needed for self-healing; in the latter case, a nanoparticle chain was not formed in the crack. Hence, a broken metal interconnect is not necessarily healed by the dielectrophoresis of metal nanoparticles. Therefore, it is still difficult to heal a broken metal interconnect in a flexible device at this time. For these reasons, it is significant to understand both the conditions forming a nanoparticle chain and the factors that determine crack configurations.

In this research, based on the two key points, complementary approaches were adopted: studying the conditions forming a nanoparticle chain to form a nanoparticle chain in a larger crack, and studying the factors that determine the crack configurations of a metal interconnect to control the number of cracks and crack width. Voltage and current applied to metal interconnect must be important parameters for nanoparticle chain formation; hence, studying the condition forming a nanoparticle chain is required to understand the electrical design principle of self-healing metal interconnect. In addition, the stiffness of the metal interconnect must be an important parameter for crack configuration; hence, studying the factors

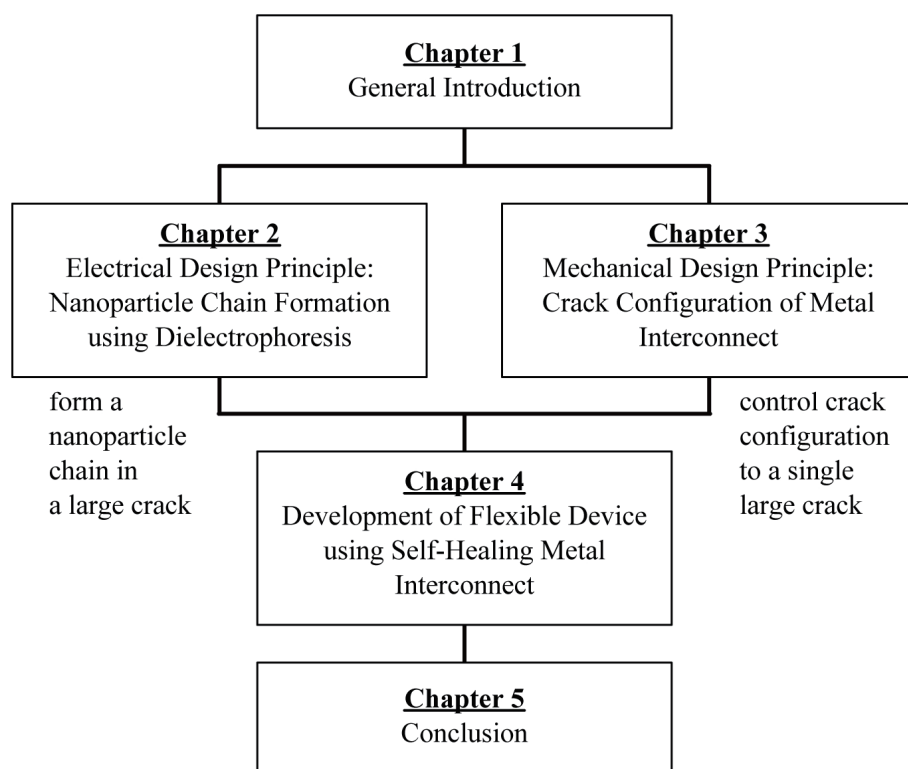


Figure 1.5 Flow chart explaining the organization of this thesis.

determining crack configuration is required to understand the mechanical design principle of self-healing metal interconnect. By forming a nanoparticle chain in the larger crack and controlling the crack configurations to a single larger crack based on the electrical and mechanical design principles, self-healing metal interconnect is applied to flexible devices.

## 1.4 Thesis Structure

This thesis is organized as shown in Figure 1.5. Chapter 1 provides a general introduction that includes the background, related previous studies, and objective of this research. To facilitate the understanding of the electrical design principle of self-healing metal interconnect, Chapter 2 examines the condition of nanoparticle chain formation using dielectrophoresis. Theoretical analysis and experiments to verify the analysis results were conducted. Chapter 3 describes the study of a crack configuration of metal interconnect to facilitate the understanding of the mechanical design principle. Theoretical analysis and

experiments to verify the analysis results were conducted, as with the condition analysis of dielectrophoresis. Based on the results presented in Chapter 2 and Chapter 3, flexible devices using self-healing metal interconnect were developed as described in Chapter 4. Chapter 5 summarizes the thesis and describes future research direction.

# Chapter 2 Nanoparticle Chain Formation using Dielectrophoresis

## 2.1 Introduction

---

In this chapter, the condition for nanoparticle chain formation using dielectrophoresis is studied to understand the electrical design principle of a self-healing metal interconnect. In previous studies, trapping some types of nanoparticles in a gap of electrodes through dielectrophoresis was used to form nano/microstructures of assembled nanoparticles [63]–[68]. In particular, the electrical property measurement of formed structure has been of great interest [69]–[73]. The formation of a nanoparticle chain structure is used for its application to micro and nano devices [74]–[76]. In this phenomenon, the gap width is one of the important parameters. Some previous studies [60]–[62] reported that a gold nanoparticle chain was successfully formed in a several- $\mu\text{m}$ -wide gap between gold electrodes and was not formed in a larger gap. However, other studies reported that a gold nanoparticle chain was formed even in a larger gap between gold electrodes (gap width of several tens of micrometers or more) [77]–[79]. The conditions enabling nanoparticle chain formation with such a large gap width remains unclear. This might be because many previous studies mainly focused on measuring the electrical properties of the formed

nanoparticle structure.

To understand the conditions that form a metal nanoparticle chain in a large crack of a broken metal interconnect such as a crack that is several tens of micrometers wide, a theoretical analysis and experiments were conducted. In this research, it was considered that the formation process of a nanoparticle chain using dielectrophoresis consists of two processes: trapping and bridging. In the trapping process, a nanoparticle is trapped and adheres to the crack surface of a broken interconnect. In the bridging process, the contentiously trapped nanoparticles form a nanoparticle chain structure and finally bridge the crack. In the theoretical analysis section, the forces acting on a nanoparticle during the trapping process and the physical phenomena during the bridging process are analyzed to clarify the conditions for nanoparticle trapping and bridging, respectively. In the experiment section, nanoparticle chain formation is observed to verify the analysis results obtained in the modeling section. Additionally, important parameters for the self-healing ability using dielectrophoresis, such as the resistance of the nanoparticle chain and forming time, are measured in the experimental section.

## 2.2 Theoretical Analysis

---

In this section, the forces acting on nanoparticles during the trapping process are analyzed to clarify the conditions for trapping the nanoparticle into a large crack. Then, the physical phenomena during the bridging process are analyzed to clarify the conditions for nanoparticle bridging.

### 2.2.1 Trapping Process

The forces acting on a nanoparticle during the trapping process were analyzed to clarify the conditions for trapping the nanoparticle in a large crack. Figure 2.1a illustrates the metal nanoparticle trapping using dielectrophoresis. A cracked metal interconnect on a substrate is covered with metal nanoparticle dispersion, and an AC voltage is applied to the interconnect. A high-frequency voltage is suitable because the effect of the interfacial polarization caused by the voltage applied to the metal interconnect surfaces is almost negligible. In this research, it is assumed that both the metal interconnects and metal nanoparticles have the same material properties. For example, gold nanoparticles in a citrate-buffered aqueous medium are usually negatively charged because citrate in the aqueous medium adheres to the surface of the gold nanoparticles. When gold nanoparticles and gold interconnects are used as the metal nanoparticles and the metal interconnects, respectively, they are charged with same sign; therefore, the nanoparticles are stably

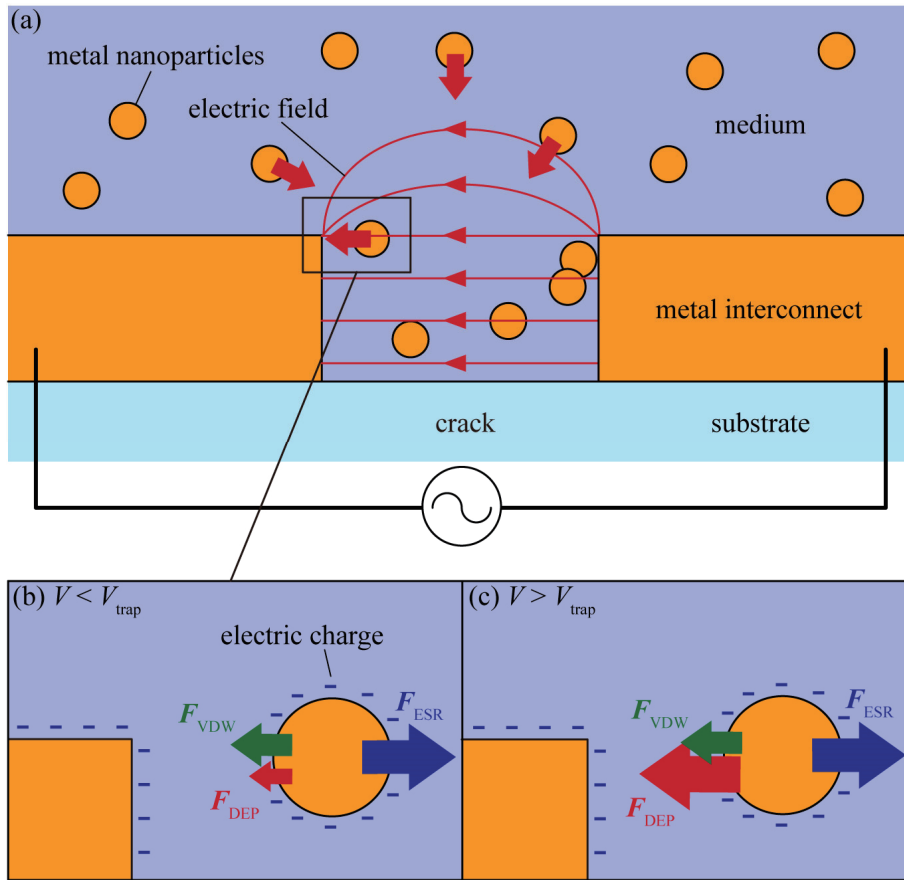


Figure 2.1 (a) Schematic illustration of metal nanoparticle trapping using dielectrophoresis. (b, c) Forces acting on nanoparticle in case of (b) low voltage and (c) higher than trapping voltage.

dispersed in the medium. In this case, the total force  $F_{\text{total}}$  acting on a nanoparticle near the crack is mainly composed of

$$F_{\text{total}} = F_{\text{VDW}} + F_{\text{ESR}} + F_{\text{DEP}} \quad (2.1)$$

where  $F_{\text{VDW}}$ ,  $F_{\text{ESR}}$ , and  $F_{\text{DEP}}$  are the Van der Waals force, electrostatic repulsive force, and dielectrophoresis forces, respectively. In Equation (2.1),  $F_{\text{VDW}}$  and  $F_{\text{ESR}}$  are forces between the nanoparticle surface and the surface of the cracked interconnect, and are given by the following:

$$F_{\text{VDW}} = \frac{Ar_{\text{par}}}{6D^2} \quad (2.2)$$



$$F_{\text{ESR}} = -\kappa r_{\text{par}} \left[ 64\pi\epsilon_{\text{med}} \left( \frac{kT}{e} \right)^2 \tanh^2 \left( \frac{ze\psi}{4kT} \right) \right] \exp^{-\kappa D} \quad (2.3)$$

where  $A$  is the Hamaker constant,  $r_{\text{par}}$  is the radius of the nanoparticle,  $D$  is the distance between the nanoparticle and the crack surface,  $\kappa$  is the inverse of the Debye length,  $\epsilon_{\text{med}}$  and  $z$  are the permittivity and the valence of the medium, respectively,  $k$  is the Boltzmann constant ( $= 1.38 \times 10^{-23} \text{ J} \cdot \text{K}^{-1}$ ),  $T$  is the absolute temperature,  $e$  is the elementary charge ( $= 1.60 \times 10^{-23} \text{ C}$ ), and  $\psi$  represents the surface potentials of the nanoparticle and crack surfaces [80]. Equations (2.2) and (2.3) show that  $F_{\text{VDW}}$  and  $F_{\text{ESR}}$  are mainly determined by the material properties of the metal nanoparticles and the medium. The time average of  $F_{\text{DEP}}$  is given by the following:

$$\langle F_{\text{DEP}} \rangle = 2\pi\epsilon_{\text{med}} r_{\text{par}}^3 \text{Re}[\underline{\mathbf{K}}(2\pi f)] \nabla E_{\text{rms}}^2 \quad (2.4)$$

where  $f$  is the frequency of the applied voltage,  $\underline{\mathbf{K}}(2\pi f)$  is the Clausius–Mosotti factor (which indicates the polarizability of the nanoparticle), and  $E_{\text{rms}}$  is the effective value of the electric field [81]. When the value of  $\text{Re}[\underline{\mathbf{K}}(2\pi f)]$  is positive,  $F_{\text{DEP}}$  is an attractive force directed to the crack. In this research,  $\text{Re}[\underline{\mathbf{K}}(2\pi f)]$  comes to 1 because metal nanoparticles are highly conductive [82]. Regarding Equation (2.4),  $E_{\text{rms}}$  is determined by the voltage applied to the crack,  $V_{\text{amp}}$ . Therefore, Equation (2.4) shows that the strength of  $F_{\text{DEP}}$  can be controlled by adjusting the applied voltage. When  $F_{\text{DEP}}$  increases with increasing voltage,  $F_{\text{total}}$  becomes an attractive force directed to the crack, according to Equation (2.1). Even in the case of a large crack, the metal nanoparticle is trapped and adheres to the surface of the cracked metal interconnect when a certain voltage or higher is applied to the interconnect, as shown in Figures 2.1b and 2.1c. In this research, the amplitude of the critical voltage is defined as a trapping voltage,  $V_{\text{trap}}$ .

### 2.2.2 Bridging Process

The physical phenomena during the bridging process were analyzed to clarify the conditions for nanoparticle bridging. Figure 2.2 illustrates the process of nanoparticle chain formation. A theoretical analysis of the trapping process indicates that an applied voltage higher than  $V_{\text{trap}}$  can trap the nanoparticles and form a nanoparticle chain even in a large crack because a higher applied voltage causes a stronger dielectrophoresis force on the nanoparticles as illustrated in Figure 2.2a. However, in previous studies [60]–[62], a large crack was not bridged by a nanoparticle chain even when a higher applied voltage was

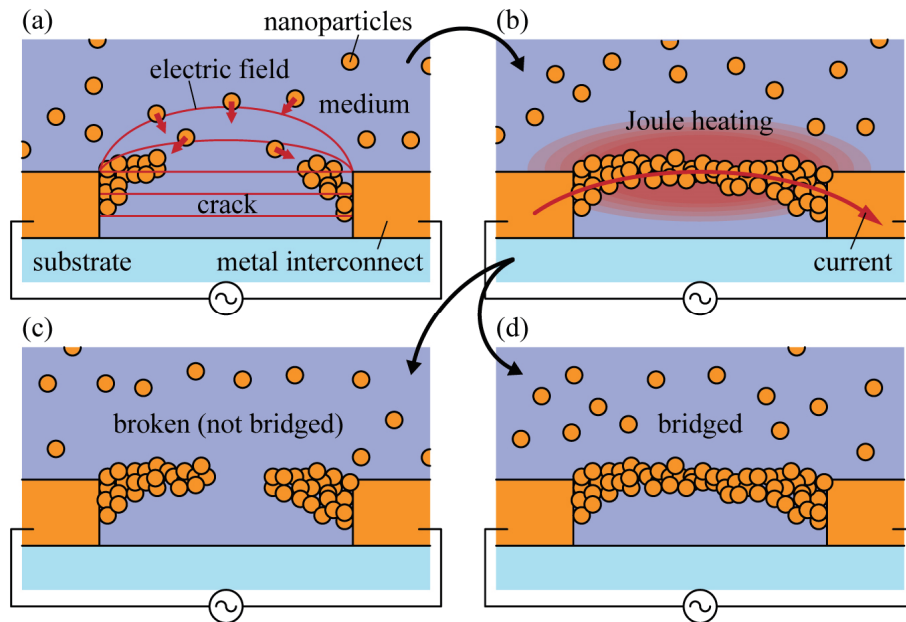


Figure 2.2 Schematic illustration of nanoparticle chain formation through dielectrophoresis. (a) Trapping of nanoparticles in cracked metal interconnect by dielectrophoresis. (b) Joule heating by current in nanoparticle chain. (c) Nanoparticle chain is broken when high voltage with high current is applied. (d) Nanoparticle chain is formed when high voltage with low current is applied.

applied. Therefore, in this research, it is considered that the current flowing just when a nanoparticle chain bridges a crack may play an important role as shown in Figure 2.2d. That is, Joule heating owing to the current was caused in each nanoparticle of the nanoparticle chain, and Joule heating under a large applied voltage might break the nanoparticle chain, as illustrated in Figure 2.2c. When the energy of Joule heating per unit time caused in each nanoparticle is larger than the energy released from the nanoparticle to the medium, the nanoparticle chain is not formed in the crack. Conversely, when the energy of Joule heating is lower than the released energy, the nanoparticle chain is formed in the crack, as illustrated in Figure 2.2d. The energy of Joule heat per unit time caused in each nanoparticle,  $P$ , is given by the following:

$$P = R_{\text{par}} I^2 \quad (2.5)$$

where  $R_{\text{par}}$  is the resistance of a single nanoparticle and  $I$  is the current flowing after nanoparticle chain bridging. As shown in Equation (2.5), Joule heating is proportional to both the resistance of each nanoparticle and the square of the current.  $R_{\text{par}}$  are determined by only the physical property and shape of

the nanoparticle. Therefore, the current must have a critical value for nanoparticle chain formation as well as the voltage causing the nanoparticle trapping. A nanoparticle chain is formed in a crack when the current is lower than the critical value. In this research, the critical value is defined as the maximum allowable current  $I_{\max}$ . In the theoretical analysis, it is considered that a nanoparticle chain can be formed in a crack several tens of micrometers wide only when a voltage higher than  $V_{\text{trap}}$  with a current lower than  $I_{\max}$  is applied.

## 2.3 Observation of Nanoparticle Chain Formation

---

Observations of a nanoparticle chain were conducted to verify the results obtained in the theoretical analysis section. First, certain voltages with changing current were applied to a cracked metal interconnect with a 10- $\mu\text{m}$ -wide crack that was covered with metal nanoparticle dispersion to confirm the nanoparticle chain formation in the large crack. In this section, a metal interconnect with a prepatterned crack on a glass substrate was used for the observation. Second, for a better understanding of the behavior of nanoparticle chain formation when a lower voltage, higher voltage with higher current, and higher voltage with lower current are applied, the process of nanoparticle chain formation was observed directly with high-magnification and high-speed microscopy. In this research, gold was used for both the metal electrodes and metal nanoparticle dispersion because of the availability and chemical stability of gold.

### 2.3.1 Fabrication

Figure 2.3 illustrates the fabrication process of a gold interconnect with a large crack on a glass substrate. First, a 0.01- $\mu\text{m}$ -thick chromium layer as an adhesion layer and 0.5- $\mu\text{m}$ -thick gold layer were deposited on a glass substrate using an electron-beam evaporation system (EBX-6D, Ulvac), as shown in Figure 2.3a. Second, a photoresist (OFPR800 20cp, Tokyo Ohka Kogyo) was spin-coated on the gold layer. Then, a photoresist was patterned in the shape of gold interconnect with a 10- $\mu\text{m}$ -wide crack, as shown in Figure 2.3b. Subsequently, the deposited gold and chromium layers were patterned in the electrode shape through a wet-etching process (Figure 2.3c). Finally, the photoresist was removed, as shown in Figure 2.3d. Figure 2.4 depicts the fabricated gold interconnect with a large crack on a glass substrate. The width of the gold interconnect was 25  $\mu\text{m}$ . Contact pads for electrical contact with an external circuit were formed at both ends of the interconnect.

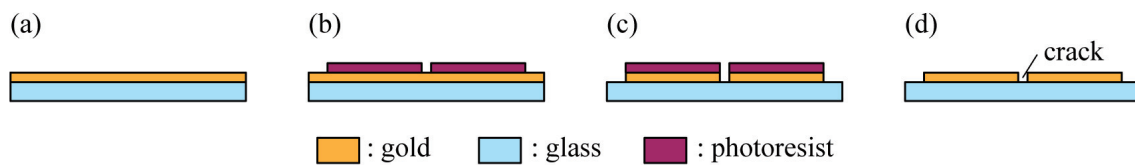


Figure 2.3 Fabrication process of cracked gold interconnect on glass substrate. (a) Deposition of chromium layer (0.01  $\mu\text{m}$  in thickness) and gold layer (0.5  $\mu\text{m}$  in thickness). (b) Spin-coating and patterning of photoresist. (c) Wet-etching gold layer and chromium layer. (d) Removal of photoresist.

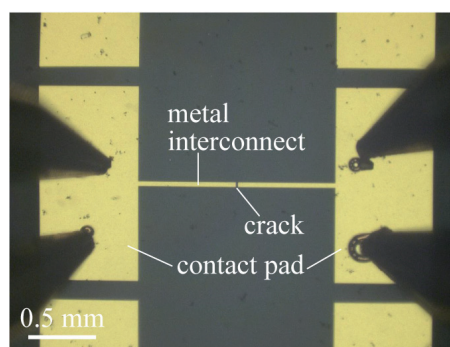


Figure 2.4 Optical image of fabricated pre-cracked gold interconnect on glass substrate.

### 2.3.2 Observation Setup

Figure 2.5 depicts the setup of observation for the nanoparticle chain formation. A gold interconnect with a 10- $\mu\text{m}$ -wide crack was covered with gold nanoparticles in a citrate-buffered aqueous medium (150 nm in diameter) (Au colloid solution-SC 150 nm, Tanaka Kikinzoku Kogyo). The pH of the medium was 3, and content rate of the gold was  $6\text{--}7 \times 10^{-3}$  wt%. A resistor was connected to the cracked interconnect in series, and AC voltage was applied across both the gold interconnect and resistor. A combination of a waveform generator (33500B, Agilent) and an amplifier (HAS 4101, NF) was used as electric power source, and the voltage was applied to the interconnect for approximately 3 min. The frequency of the applied voltage was 100 kHz because a previous study reported that the number of trapped gold nanoparticles was determined by the frequency, and 100 kHz was suitable for nanoparticle chain formation [83]. The voltage applied across the crack,  $V_{\text{crack}}$ , and the current flowing in the assembled nanoparticles were changed by changing both the resistance of the resistor,  $R_{\text{res}}$ , and the voltage applied to the circuit,

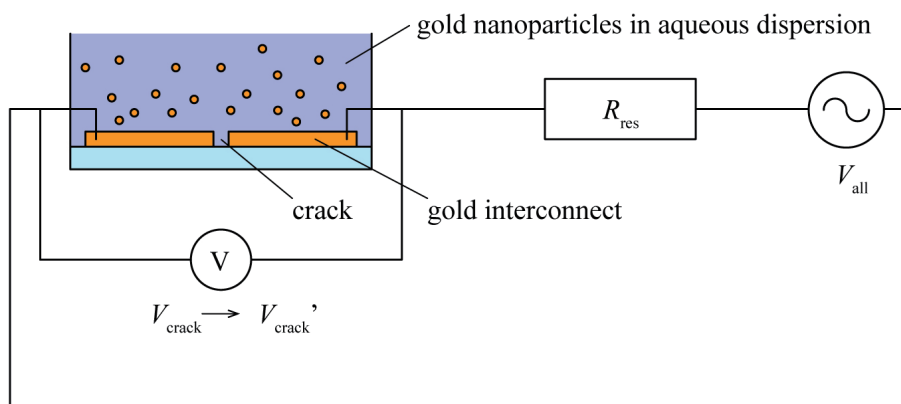


Figure 2.5 Observation setup for gold nanoparticle chain formation.

$V_{\text{all}}$ . The values of  $R_{\text{res}}$  were 4.6 k $\Omega$ , 1.8 k $\Omega$ , 0.99 k $\Omega$ , 0.46 k $\Omega$ , and 0.18 k $\Omega$ . When a nanoparticle chain bridges the crack,  $V_{\text{crack}}$  decreases to  $V_{\text{crack}}'$  because the impedance of the cracked gold interconnect decreases sharply.  $V_{\text{crack}}$  was monitored using an oscilloscope (DSO-X 2024A, Agilent). The value of  $V_{\text{all}}/R_{\text{res}}$  was used as the representative value of current flowing in a nanoparticle chain. Once nanoparticles were trapped and a nanoparticle chain was formed in the crack, the nanoparticle chain retained its form even after the applied voltage was stopped. After the nanoparticle formation, the cracked interconnect was washed with pure water and dried for scanning electron microscope (SEM) observation.

The setup for direct observation of the process of nanoparticle chain formation was as follows. A citrate-buffered aqueous medium of 150-nm-diameter gold nanoparticles was also dropped on the 10- $\mu\text{m}$ -wide crack and covered with a cover glass. Based on the results of the above observation,  $V_{\text{crack}}$  and  $V_{\text{all}}/R_{\text{res}}$  were set to 1.9 V<sub>rms</sub> and 11 mA<sub>rms</sub> to represent the low voltage case, 10.3 V<sub>rms</sub> and 60 mA<sub>rms</sub> to represent the high voltage with high current case, and 8.9 V<sub>rms</sub> and 1.8 mA<sub>rms</sub> to represent the high voltage with low current case. A high-speed optical microscope (VW-9000, Keyence) with a magnification of 3,000 $\times$  was used for the direct observation. The frame rate of microscopy was 4,000 fps (0.25 ms/frame). Metal halide lamps were used as both the top and bottom light sources of the microscope to obtain sufficient light intensity for the direct observation.

### 2.3.3 Results and Discussion

Figure 2.6 depicts a condition plot for nanoparticle chain formation in the case of a 10- $\mu\text{m}$  crack width,

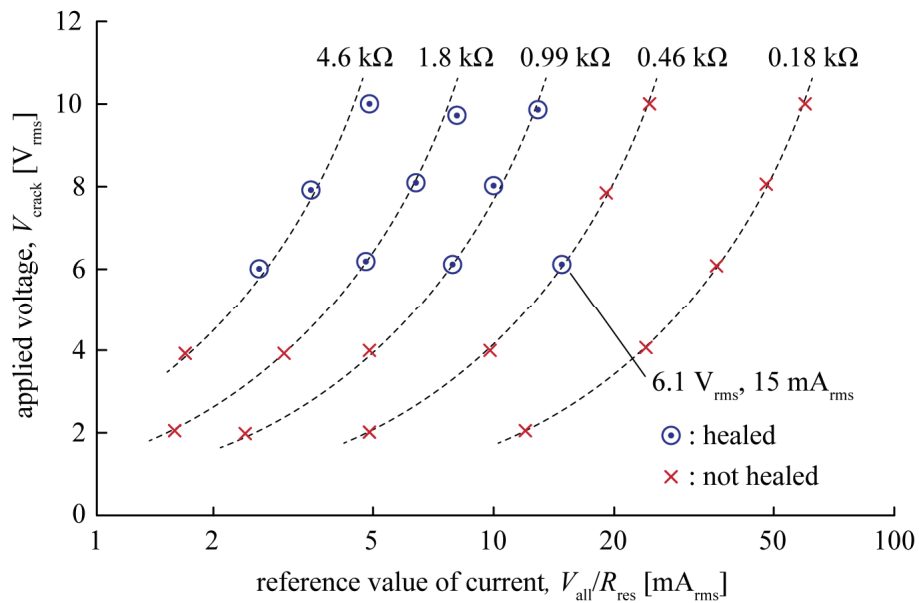


Figure 2.6 Formation condition plot between applied voltage,  $V_{\text{crack}}$ , and representative value of current,  $V_{\text{all}}/R_{\text{res}}$ , for 10- $\mu\text{m}$ -wide crack.

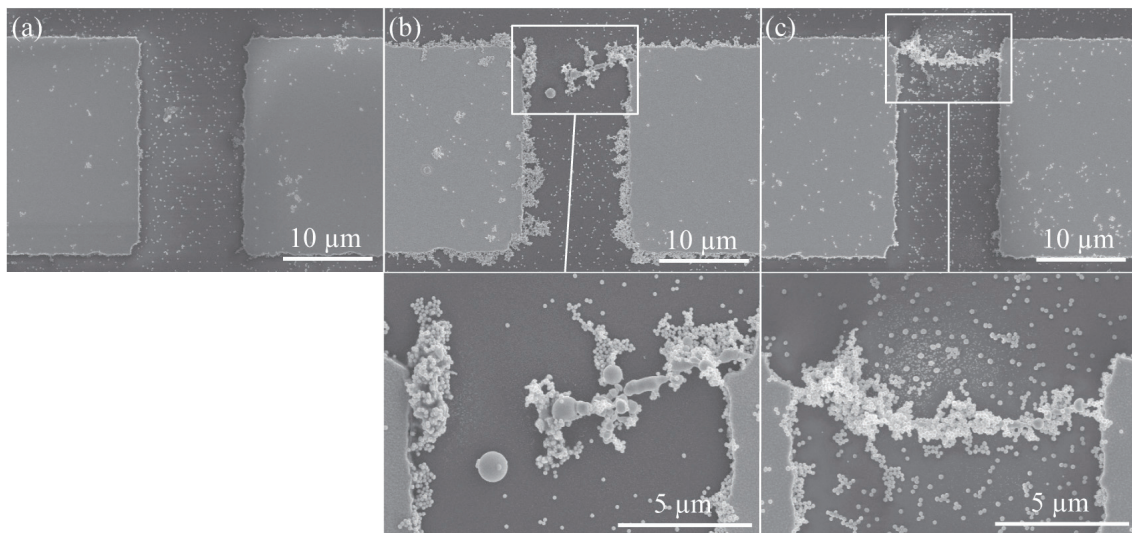


Figure 2.7 (a) SEM image for 2.0 V<sub>rms</sub> with 4.9 mA<sub>rms</sub>, (b) 10.0 V<sub>rms</sub> with 60 mA<sub>rms</sub>, and (c) 8.1 V<sub>rms</sub> with 6.4 mA<sub>rms</sub> in Figure 2.6.

and Figure 2.7 shows the SEM image in each voltage and current condition. When a  $V_{\text{crack}}$  was 4.1 V<sub>rms</sub> or

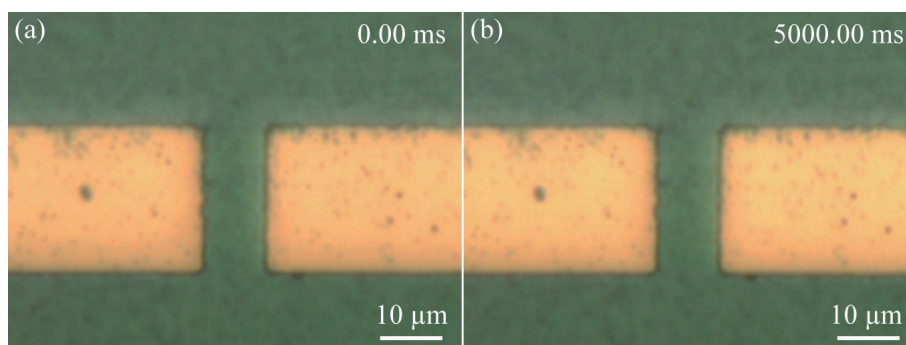


Figure 2.8 Series of optical images showing gold nanoparticle chain formation for low voltage applied to cracked gold interconnect. (a) and (b) Nanoparticle chain not observed clearly.

less, a nanoparticle chain was not observed, as shown in Figure 2.7a. This indicates that the dielectrophoresis force on the nanoparticles was weak owing to the low applied voltage, and the nanoparticles were not trapped to the crack. When a voltage greater than or equal to  $6.1 V_{\text{rms}}$  with a current greater than or equal to  $19 \text{ mA}_{\text{rms}}$  was applied, an imperfect nanoparticle chain was observed in the crack, as shown in Figure 2.7b. A micrometer-sized lump of gold was observed in part of the imperfect nanoparticle chain, which indicates that some of the nanoparticles in the nanoparticle chain had melted by Joule heating. Conversely, a nanoparticle chain was observed in the crack when a voltage greater than or equal to  $6.1 V_{\text{rms}}$  with a current less than or equal to  $15 \text{ mA}_{\text{rms}}$  was applied across a crack of the interconnect, as shown in Figure 2.7c. This indicates that a nanoparticle chain can be formed even in a large crack when a high voltage with low current is applied. A nanoparticle chain was often formed around the edges of the cracked interconnect, as shown in in Figure 2.7. This is because nanoparticles were trapped more at the edges because the gradient of the electric field was especially strong around the edges.

The series of optical images shown in Figures 2.8, 2.9, and 2.10 are the results of the direct observations of nanoparticle chain formation for low voltage, high voltage with high current, and high voltage with low current. When a low voltage was applied to the interconnect, nanoparticles were not trapped in the crack, as depicted in Figures 2.8a and 2.8b. However, when a high voltage with high current was applied, some nanoparticles were trapped and an assembled nanoparticle structure was formed in the crack at the beginning of microscopy, as shown in Figure 2.9a. Approximately 5 s later, the number of trapped nanoparticles increased and the assembled nanoparticle structure was growing as a chain structure, as shown in Figure 2.9b. Subsequently, the nanoparticle chain suddenly started to break just when the

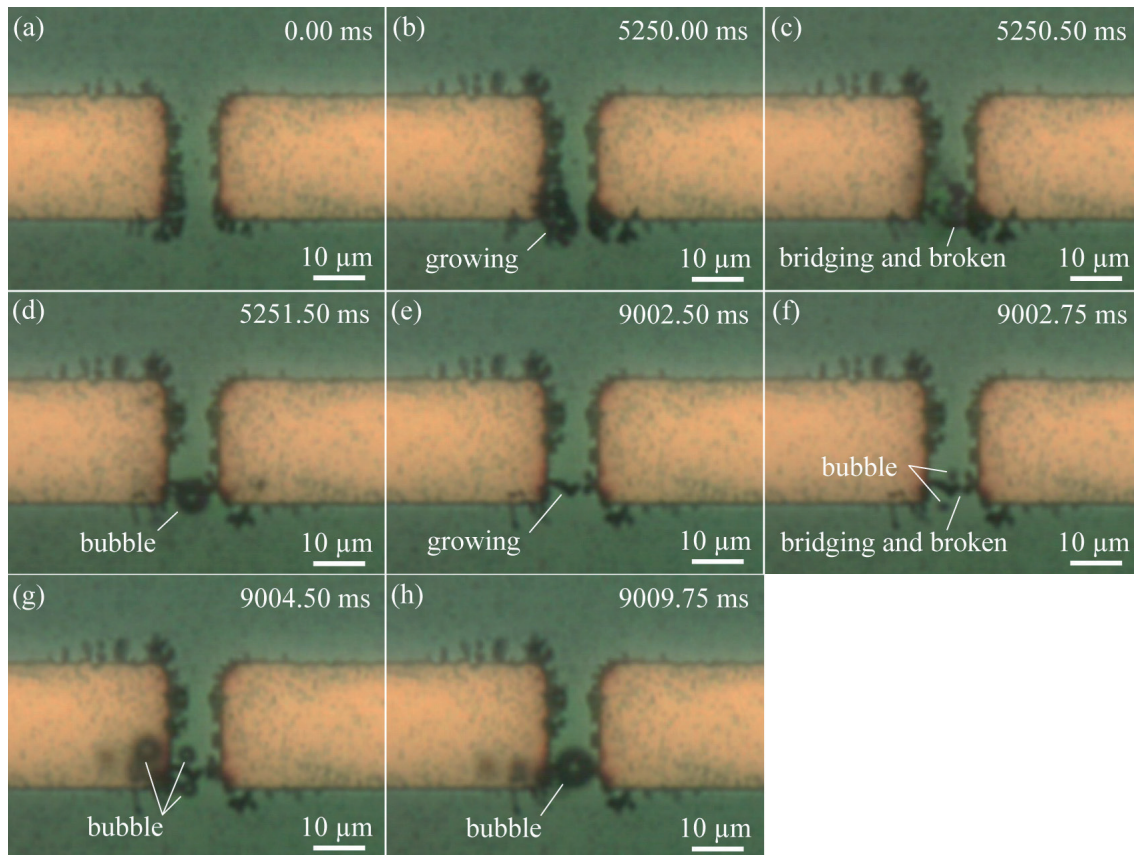


Figure 2.9 Series of optical images showing gold nanoparticle chain formation for high voltage with high current. (a, b) Nanoparticle chains growing. (c, d) One nanoparticle chain is bridging and being broken. (e) Another nanoparticle chain is regrowing. (f, g, and h) Nanoparticle chain being broken again.

nanoparticle chain bridged the crack, as shown in Figure 2.9c, and some microbubbles were observed around the crack (Figure 2.9d). This indicates that part of citrate-buffered aqueous medium around the nanoparticle chain was suddenly heated and evaporated by Joule heating, thus breaking the nanoparticle chain. Approximately 4 s later, another nanoparticle chain was growing again, as depicted in Figure 2.9e, and subsequently began to break again just when the nanoparticle chain bridged the crack (Figure 2.9f). Some microbubbles were observed again, as shown in Figures 2.9g and 2.9h. This breaking process was repeatedly observed while voltage was applied across the crack of the interconnect. When a high voltage with low current was applied, nanoparticles were also trapped, especially at the edges of the cracked interconnect, as shown Figure 2.10a. Subsequently, one of the nanoparticle chains grew rapidly (Figures



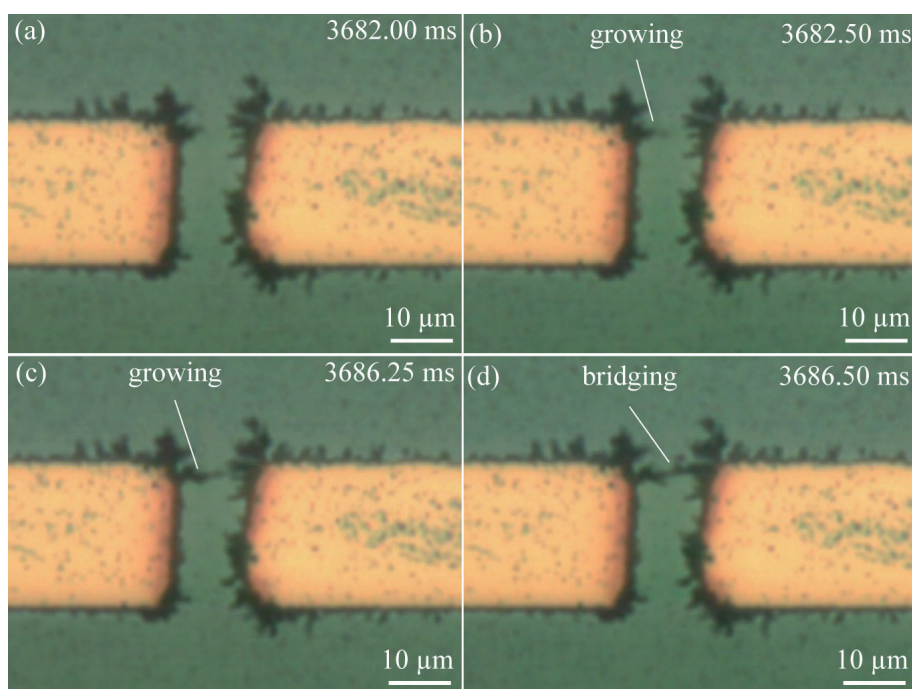


Figure 2.10 Series of optical images showing gold nanoparticle chain formation for high voltage with low current. (a) Nanoparticles trapped in crack. (b, c) Nanoparticle chain growing. (d) Nanoparticle chain bridging crack.

2.10b, 2.10c, and 2.10d), bridging a crack in approximately 4 ms. In this case, microbubbles were not observed around the nanoparticle chain.

## 2.4 Measurement of Maximum Allowable Current and Resistance of Nanoparticle chain

Based on the results of the observation of nanoparticle chain formation, important parameters for the self-healing metal interconnect using the dielectrophoresis of metal nanoparticles, such as the maximum allowable current,  $I_{\max}$ , and the resistance of the nanoparticle chain formed in the crack,  $R_{\text{chain}}$ , were experimentally measured.

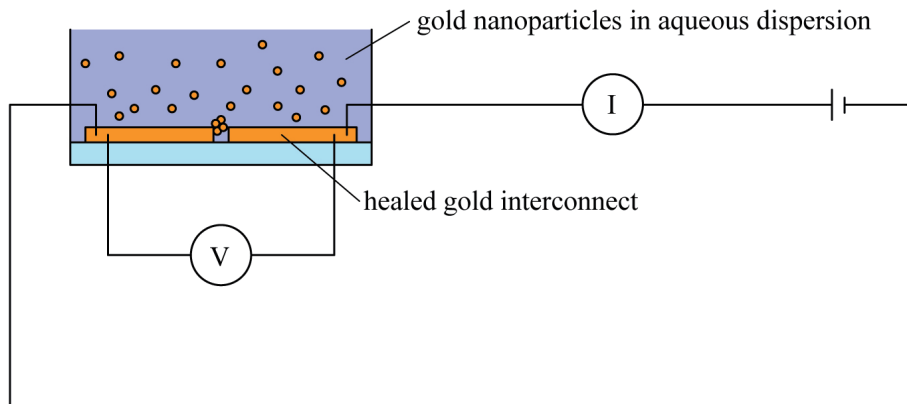


Figure 2.11 Measurement setup for maximum allowable current,  $I_{\max}$ , and resistance of nanoparticle chain,  $R_{\text{chain}}$ .

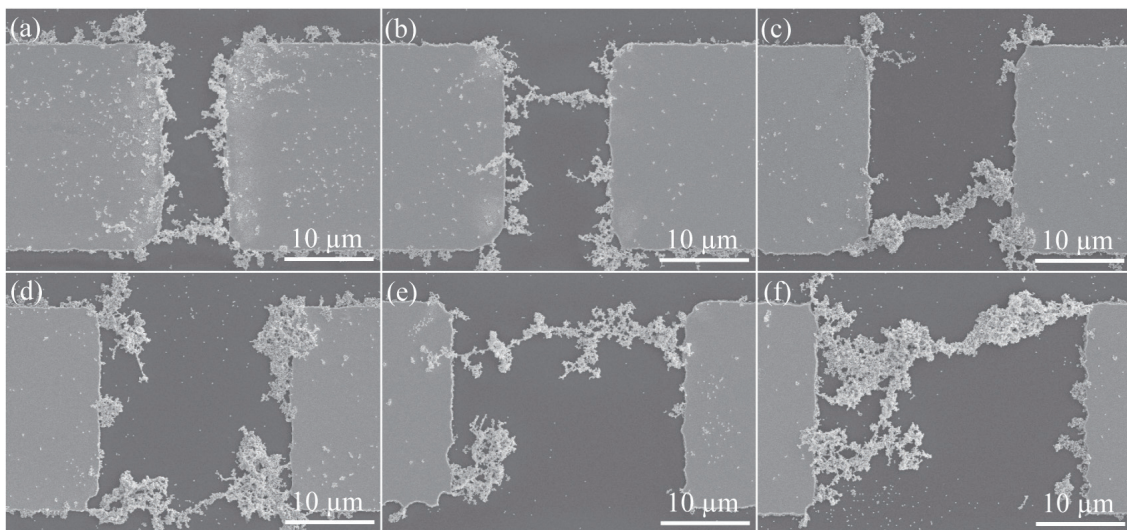


Figure 2.12 SEM images of gold nanoparticle chain in crack of gold interconnect on glass substrate corresponding to crack widths of (a) 5  $\mu\text{m}$ , (b) 10  $\mu\text{m}$ , (c) 15  $\mu\text{m}$ , (d) 20  $\mu\text{m}$ , (e) 25  $\mu\text{m}$ , and (f) 30  $\mu\text{m}$ .

#### 2.4.1 Measurement Setup

A cracked gold interconnect with a 5-to-30- $\mu\text{m}$ -wide crack on a glass substrate was fabricated, and each crack was covered with a citrate-buffered aqueous medium of 150-nm-diameter gold nanoparticles. AC

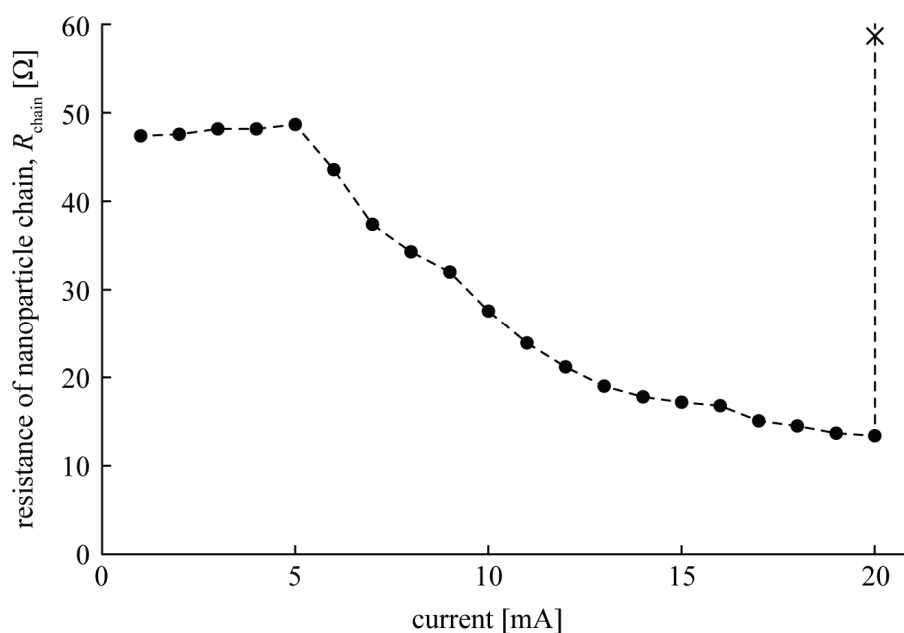


Figure 2.13 Resistance of nanoparticle chain in cracked gold interconnect,  $R_{\text{chain}}$ , changes with increasing current in 10- $\mu\text{m}$ -wide crack.

voltage ( $V_{\text{crack}}$  and  $V_{\text{all}}/R_{\text{res}}$  were 15  $V_{\text{rms}}$  and 4.9  $\text{mA}_{\text{rms}}$ , respectively) was applied to each cracked gold interconnect in the same manner as shown in Figure 2.5. It was confirmed that a nanoparticle chain was formed in each cracked interconnect, as depicted in Figure 2.12. Subsequently, each bridged gold interconnect was connected to a source meter (2614B, Keithley Instruments), and increasing current was applied to each nanoparticle chain while measuring the resistance of the healed gold interconnect. The resistance of the uncracked gold interconnect was 5.8  $\Omega$ ; therefore,  $R_{\text{chain}}$  was given by subtracting 5.8  $\Omega$  from the resistance of the healed gold interconnect. During the measurement, each crack was covered with gold nanoparticle dispersion, and the current was gradually increased in steps of 1.0 mA. During each step, current was applied for several seconds until the value of the resistance became stable because the value of the resistance gradually decreased during each step. The number of trials for each crack width was five.

#### 2.4.2 Results and Discussion

Figure 2.13 illustrates the resistance change of  $R_{\text{chain}}$  in the case of a 10- $\mu\text{m}$ -wide crack.  $R_{\text{chain}}$  increased slightly from 1.0 to 5.0 mA. However,  $R_{\text{chain}}$  decreased as the current increased beyond 5.0 mA, and  $R_{\text{chain}}$

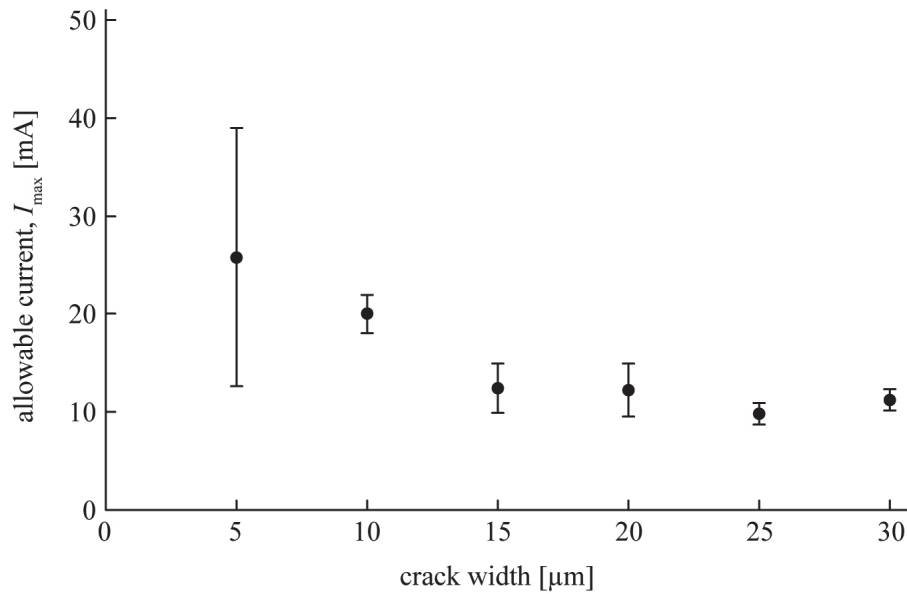


Figure 2.14 Maximum allowable current,  $I_{\max}$ , as determined by crack width.

increased sharply when the current increased from 20.0 to 21.0 mA. This indicates that a nanoparticle chain was broken by excessive current. After the measurement, it was confirmed that a nanoparticle chain was broken by the SEM observation. Hence,  $I_{\max}$  is 20 mA in Figure 2.13. Regarding the decrease in  $R_{\text{chain}}$ , this might occur because of the decrease in the contact resistance of the nanoparticle chain.  $R_{\text{chain}}$  is expressed by the following:

$$R_{\text{chain}} = R_{\text{crc}} + n(R_{\text{crp}} + R_{\text{irp}}) \quad (2.6)$$

where  $R_{\text{crc}}$  is the contact resistance between the nanoparticle chain and the crack surface,  $n$  is the integer of the number of nanoparticles where current flows,  $R_{\text{crp}}$  is the contact resistance between the nanoparticle surfaces, and  $R_{\text{irp}}$  is the internal resistance of the nanoparticles. When current flowing through the nanoparticle chain increases in the range of lower current,  $R_{\text{irp}}$  is increased by a temperature increase in each nanoparticle according to Joule heating. Therefore,  $R_{\text{chain}}$  increases, as shown in Figure 2.13. Conversely, when the current increase is in the range of the higher current, each nanoparticle might gradually start melting as a result of Joule heating. In this case, in Equation (2.6),  $R_{\text{crc}}$  and  $R_{\text{crp}}$  decrease. Therefore,  $R_{\text{chain}}$  decreases as current increases, as shown in Figure 2.13.

Figure 2.14 depicts the measurement results of  $I_{\max}$  determined by the crack width.  $I_{\max}$  decreased

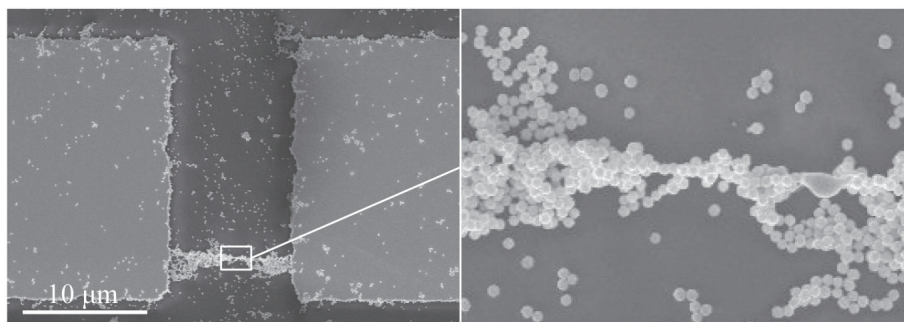


Figure 2.15 SEM images of nanoparticle chain with partially single-nanoparticle bridging structure. Crack width is 10  $\mu\text{m}$ .

as the crack width increased from 5  $\mu\text{m}$  to 15  $\mu\text{m}$ .  $I_{\text{max}}$  was approximately 11 mA from 15  $\mu\text{m}$  to 30  $\mu\text{m}$ , which indicates that  $I_{\text{max}}$  must be 11 mA for a crack width greater than 30  $\mu\text{m}$ . Therefore, when an aqueous dispersion of 150-nm-diameter gold nanoparticles is used, a nanoparticle chain must be formed in a crack several tens of micrometers wide when a high voltage (for example, 15  $V_{\text{rms}}$  or higher) with a current less than 11 mA is applied. The value change of  $I_{\text{max}}$  as determined by the crack width might be because a single-nanoparticle bridging structure is partially formed in the nanoparticle chain structure. When the crack width is greater than 10  $\mu\text{m}$ , it was observed that a single-nanoparticle bridging structure was partially formed in the nanoparticle chain structure, as shown in Figure 2.15. The nanoparticle chain might break owing to Joule heating at the single-nanoparticle bridging structure; therefore, in the range of wider crack width in Figure 2.14,  $I_{\text{max}}$  shows a constant value. This indicates that  $I_{\text{max}}$  might be determined by the diameter of the nanoparticle. When the crack width was smaller than 10  $\mu\text{m}$ , a single-nanoparticle bridging structure was sometimes not observed in the nanoparticle chain structure. In this case,  $I_{\text{max}}$  might show a higher value. Therefore,  $I_{\text{max}}$  in the range of a smaller crack width shows a wide range of values, as shown in Figure 2.14.

Figure 2.16 shows the measurement results of  $R_{\text{chain}}$  determined by the crack width.  $R_{\text{chain}}$  at 1.0 mA and  $I_{\text{max}}$  are depicted in Figure 2.16. In both cases,  $R_{\text{chain}}$  increased almost linearly as the crack width increased. The value of  $R_{\text{chain}}$  at 1 mA and  $I_{\text{max}}$  ranged from 23 to 94  $\Omega$  and 10 to 65  $\Omega$ , respectively, when the crack width ranged from 5 to 30  $\mu\text{m}$ . Compared with the values of  $R_{\text{chain}}$  at 1.0 mA and  $I_{\text{max}}$ , the values of  $R_{\text{chain}}$  at  $I_{\text{max}}$  were lower than those of  $R_{\text{chain}}$  at 1.0 mA. The plots by the least-square method show that the rate of change is similar, and the intercept of  $R_{\text{chain}}$  at  $I_{\text{max}}$  is lower than  $R_{\text{chain}}$  at 1.0 mA. This indicates

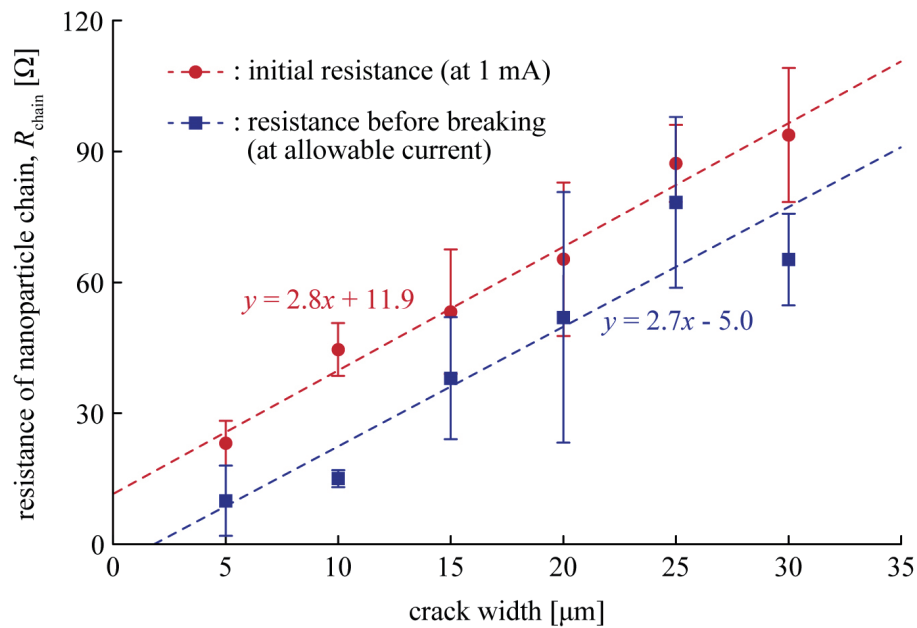


Figure 2.16 Resistance of nanoparticle chain in cracked gold interconnect,  $R_{\text{chain}}$ , as determined by crack width.

that  $R_{\text{crc}}$  is significantly decreased by Joule heating in Equation (2.6). Regarding Equation (2.6),  $R_{\text{crp}}$  and  $R_{\text{irp}}$  must be determined by the number of nanoparticles in the nanoparticle chain formation. This means that  $R_{\text{crp}}$  and  $R_{\text{irp}}$  must be determined by the crack width. Therefore, in Figure 2.16, the rate of change must be determined by  $R_{\text{crp}}$  and  $R_{\text{irp}}$ . In contrast,  $R_{\text{crc}}$  is not determined by the crack width;  $R_{\text{crc}}$  must be intercepted in Figure 2.16. Therefore,  $R_{\text{crc}}$  is significantly decreased by Joule heating.

## 2.5 Measurement of Forming Time

Forming time,  $t_{\text{form}}$ , which is also an important parameter for the self-healing ability using dielectrophoresis, was measured. In the theoretical analysis section, the result indicates that a higher voltage applied to the cracked interconnect causes a stronger dielectrophoresis force on the nanoparticles near the crack. Therefore,  $t_{\text{form}}$  decreases as the applied voltage increases. Additionally,  $t_{\text{form}}$  must be determined by the crack width. Therefore, measurements of  $t_{\text{form}}$  with different applied voltages and crack widths were conducted.

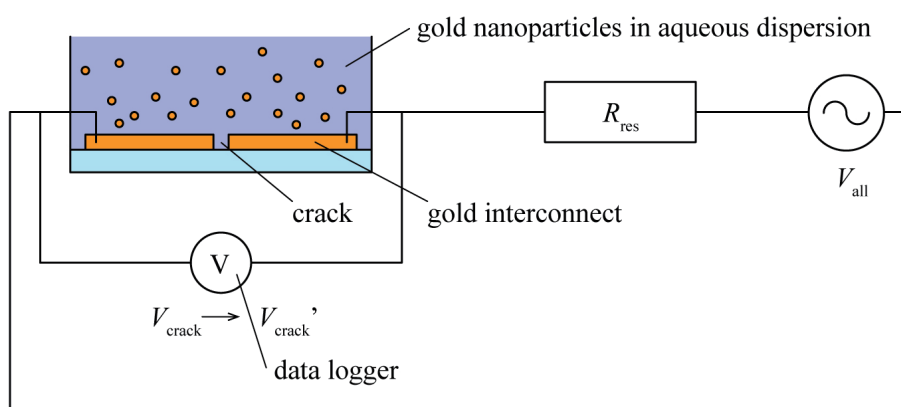


Figure 2.17 Measurement setup for forming time,  $t_{\text{form}}$ .

### 2.5.1 Measurement Setup

Figure 2.17 depicts the measurement setup for  $t_{\text{form}}$ . The setup was basically the same as that for the observation of nanoparticle chain formation. The cracked gold interconnect (crack width formed at 5 to 25  $\mu\text{m}$ ) was covered with a citrate-buffered aqueous medium of 150-nm-diameter gold nanoparticles. A resistor (10  $\text{k}\Omega$ ) was connected to the cracked interconnect in series, and an AC voltage of 100 kHz was applied across both the cracked interconnect and resistor by a waveform generator and an amplifier for approximately 3 min. The voltage applied to the cracked interconnect,  $V_{\text{crack}}$ , was 10  $\text{V}_{\text{rms}}$  or 12  $\text{V}_{\text{rms}}$ . When a nanoparticle chain bridges the crack,  $V_{\text{crack}}$  changes to  $V_{\text{crack}}'$  because of the decrease in the impedance of the cracked interconnect. The change in  $V_{\text{crack}}$  was monitored using a data logger (GL7000, Graphtec) with a high-speed voltage unit (GL7-HSV, Graphtec). The time between the start of applying the voltage and the sharp decrease in  $V_{\text{crack}}$  is defined as  $t_{\text{form}}$ . The number of trials was six.

### 2.5.2 Results and Discussion

Figure 2.18 shows the measurement result of  $t_{\text{form}}$  as determined by the crack width. In both cases of 10  $\text{V}_{\text{rms}}$  and 12  $\text{V}_{\text{rms}}$ ,  $t_{\text{form}}$  increased as the crack width increased. The values of  $t_{\text{form}}$  for 10  $\text{V}_{\text{rms}}$  and 12  $\text{V}_{\text{rms}}$  ranged from 15 to 47 s and 7 to 21 s, respectively, when the crack width was 5 to 20  $\mu\text{m}$ . When the crack width was 25  $\mu\text{m}$ , the cracked interconnect was healed only three times in 3 min in the case of 10  $\text{V}_{\text{rms}}$ .

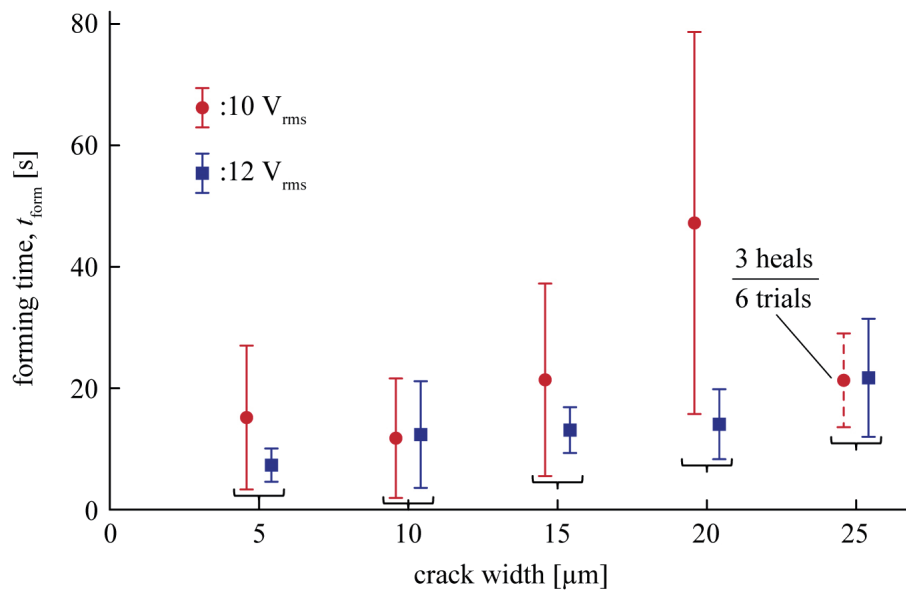


Figure 2.18 Forming time,  $t_{\text{form}}$ , as determined by crack width.

This indicates that  $t_{\text{form}}$  decreased when a higher voltage was applied to the cracked interconnect. This must occur because higher voltages applied to the cracked interconnect cause a stronger dielectrophoresis force on the nanoparticles near the crack.

## 2.6 Summary

The conditions for nanoparticle chain formation in a crack that is several tens of micrometers wide were studied by both theoretical analysis and experiments. In the theoretical analysis section, the formation process of a nanoparticle chain was divided into trapping and bridging processes, and each process was analyzed. For the trapping process, the forces acting on a nanoparticle during the trapping process were analyzed. The nanoparticles were trapped and adhered to the cracked interconnect with a large crack when a certain voltage or higher was applied to the interconnect. The voltage is  $V_{\text{trap}}$ , in which the total force acting on the nanoparticles becomes attracted to the crack surface. The physical phenomena during the bridging process were analyzed for the bridging process, and the Joule heating caused in the nanoparticles of the nanoparticle chain by the current breaks the nanoparticle chain when the nanoparticle chain bridges a large crack. Therefore, a nanoparticle chain can be formed in a crack several tens of micrometers wide



only when a voltage higher than  $V_{\text{trap}}$  with a current lower than  $I_{\text{max}}$  is applied. In the experiment section, observations and measurements were conducted to verify the analysis result obtained in the theoretical analysis section. First, certain voltages with changing currents were applied to a 10- $\mu\text{m}$ -wide crack to confirm that a nanoparticle chain is formed in a large crack when a high voltage with low current is applied. In this research, an aqueous dispersion of 150-nm-diameter gold nanoparticles was used. As a result, nanoparticle chain formation was observed in a crack only when 6.1  $V_{\text{rms}}$  or higher with 15  $\text{mA}_{\text{rms}}$  or lower was applied. Additionally, the process of nanoparticle chain formation was directly observed with high-magnification and high-speed microscopy to understand the behavior of nanoparticle chain formation. As a result, when a low voltage was applied, the nanoparticles were not trapped in the crack. Conversely, when a high voltage with high current was applied, the repeated growth and breakage of a nanoparticle chain in the crack was observed. Further, microbubbles were observed around the nanoparticle chain when it bridged the crack. When a high voltage with low current was applied, the rapid growth of a nanoparticle chain to bridge the crack was observed in approximately 4 ms. In this case, microbubbles were not observed around the nanoparticle chain. Next,  $I_{\text{max}}$  and  $R_{\text{chain}}$  were measured with increasing current applied to the nanoparticle chain. The value of  $I_{\text{max}}$  decreased as the crack width increased, and  $I_{\text{max}}$  was approximately 11 mA for crack widths in the range of 15 to 30  $\mu\text{m}$  in the case of an aqueous dispersion of 150-nm-diameter gold nanoparticles. This result indicates that a nanoparticle chain must be formed in a crack several tens of micrometers wide when a high voltage with current lower than 11 mA is applied. The value of  $R_{\text{chain}}$  increased almost linearly as the crack width increased, and the value at 1 mA and  $I_{\text{max}}$  ranged from 23 to 94  $\Omega$  and 10 to 65  $\Omega$ , respectively, when the crack width was from 5 to 30  $\mu\text{m}$ . The resistance of the metal interconnect healed by the dielectrophoresis of metal nanoparticles must be lower when a high voltage with the maximum allowable current is applied. Finally,  $t_{\text{form}}$  was measured with different voltages applied to the interconnect. As a result, the values of  $t_{\text{form}}$  for 10  $V_{\text{rms}}$  and 12  $V_{\text{rms}}$  ranged from 15 to 47 s and 7 to 21 s, respectively, when the crack width was 5 to 20  $\mu\text{m}$ . Therefore,  $t_{\text{form}}$  must be shorter when a higher voltage is applied to the cracked interconnect.

# Chapter 3 Crack Configuration of Metal Interconnect

## 3.1 Introduction

---

In this chapter, to understand the mechanical design principles of a self-healing metal interconnect, factors determining the crack configuration of a metal interconnect are studied. Regarding the self-healing metal interconnect using the dielectrophoresis of metal nanoparticles, an applied voltage needed for self-healing is determined by the number of cracks and crack width; therefore, the two parameters are important. As mentioned above, various metal interconnects for flexible devices have been proposed, and the crack configurations of the metal interconnects observed in previous studies differ considerably. Some studies reported many microcracks (such as randomly distributed tribrached microcracks), whereas other studies reported a few large cracks that propagated and crossed the metal interconnect perpendicular to the deformation direction. the applied voltage needed for self-healing in the latter case is much lower than in the former case. However, the factors determining the crack configurations are still not clear. This might be because the focus of many previous studies was to prevent breaking the conductive interconnect and achieving high stretchability while maintaining high conductivity.

Theoretical analysis and experiments were conducted to understand the factors determining the crack configurations of a stretched metal interconnect. In the theoretical analysis section, the stretching deformation of a metal interconnect embedded in an elastomer is analyzed. In the experiments section, to verify the results obtained in the theoretical analysis section, straight-shaped metal interconnects are fabricated, and cracks caused on the interconnect by stretching deformation are observed. In this research, cracks were analyzed with respect to the crack width and the number of cracks. Next, to measure the breaking elongation and crack width of a metal interconnect that is broken with a large single crack, wave-shaped metal interconnects are fabricated, and cracks caused by stretching deformation are observed.

## 3.2 Theoretical Analysis

---

The stretching deformation of a metal interconnect embedded in an elastomer is analyzed to understand the factors determining crack configurations.

### 3.2.1 Theoretical Calculation

Figure 3.1a shows a schematic illustration of a cracked metal interconnect embedded in an elastomer. In Figure 3.1a, it is assumed that the thickness of the metal interconnect is several tens of nanometers to several tens of micrometers, and the thickness of the elastomer is several tens of micrometers to several millimeters. A small crack is caused in the interconnect, and both the interconnect and the elastomer are deformed by a constant balanced force. In Figure 3.1a, the strain in the cracked region is denoted as  $\varepsilon_A$  and that in the non-cracked region as  $\varepsilon_B$ ; it is assumed that all of the strains are uniform over each region, and that  $\varepsilon_A$  is larger than  $\varepsilon_B$ , as shown in Figures 3.1b, c. These figures illustrate the simplified stress-strain curves of a metal interconnect and an elastomer in Figure 3.1a. For flexible devices, copper or gold is often used in conductive interconnect layers, and polyurethane (PU) or polydimethylsiloxane (PDMS) is used in elastomer layers. Therefore, the stress-strain curves are simplified based on the material. The balanced force around the boundary between the cracked and non-cracked regions in Figure 3.1a is expressed as

$$\varepsilon_A E_{\text{elast}} A_{\text{elast}} = \sigma_{\text{break}} A_{\text{inter}} + \varepsilon_B E_{\text{elast}} A_{\text{elast}} \quad (3.1)$$

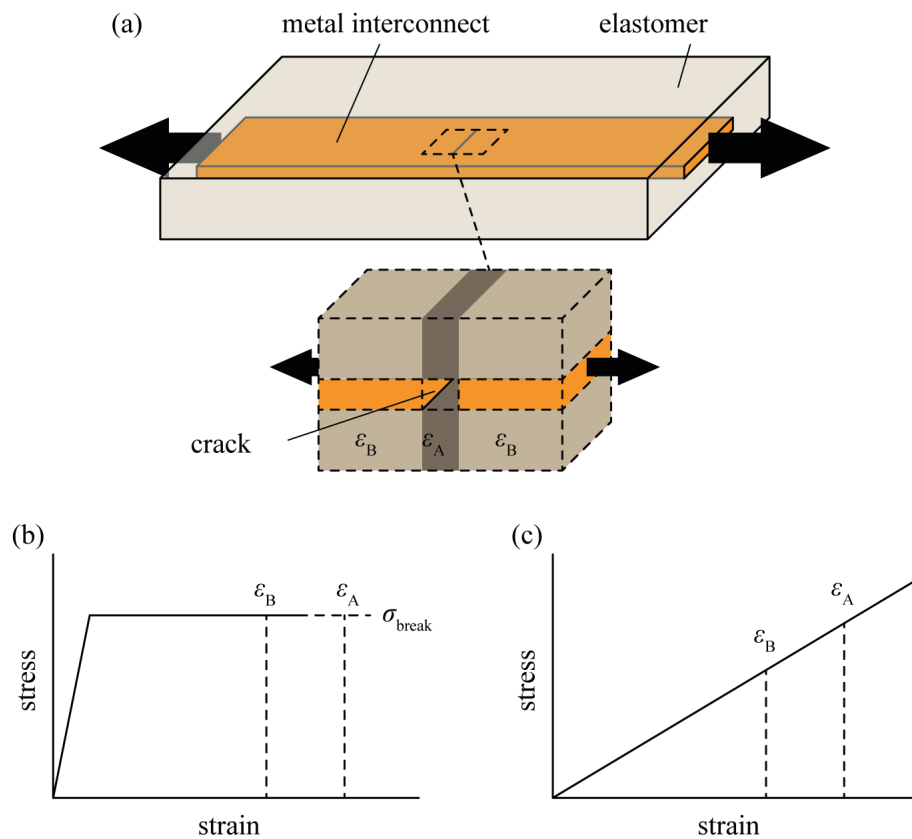


Figure 3.1 Theoretical calculation for factors determining crack configurations of stretched metal interconnect. (a) Schematic illustration of cracked metal interconnect embedded in elastomer. (b) Simplified stress-strain curve of metal interconnect layer. (c) Simplified stress strain-curve of elastomer.

where  $E_{\text{elast}}$ ,  $A_{\text{elast}}$ ,  $\sigma_{\text{break}}$ , and  $A_{\text{inter}}$  are the Young's modulus of the elastomer, cross-sectional area of the elastomer, breaking stress of the metal interconnect, and cross-sectional area of the metal interconnect, respectively. Focusing on  $\varepsilon_A$  and  $\varepsilon_B$ , Equation (3.1) is expressed by the following:

$$\varepsilon_A - \varepsilon_B = \frac{\sigma_{\text{break}} A_{\text{inter}}}{E_{\text{elast}} A_{\text{elast}}} \quad (3.2)$$

The left side of Equation (3.2) is the difference between  $\varepsilon_A$  and  $\varepsilon_B$ , and the right side is the elongation stiffness ratio of the metal interconnect and elastomer. Therefore, Equation (3.2) indicates that the difference between  $\varepsilon_A$  and  $\varepsilon_B$  is determined by the elongation stiffness ratio of the metal interconnect and elastomer. When the elongation stiffness ratio is considerably small (when the elongation stiffness of

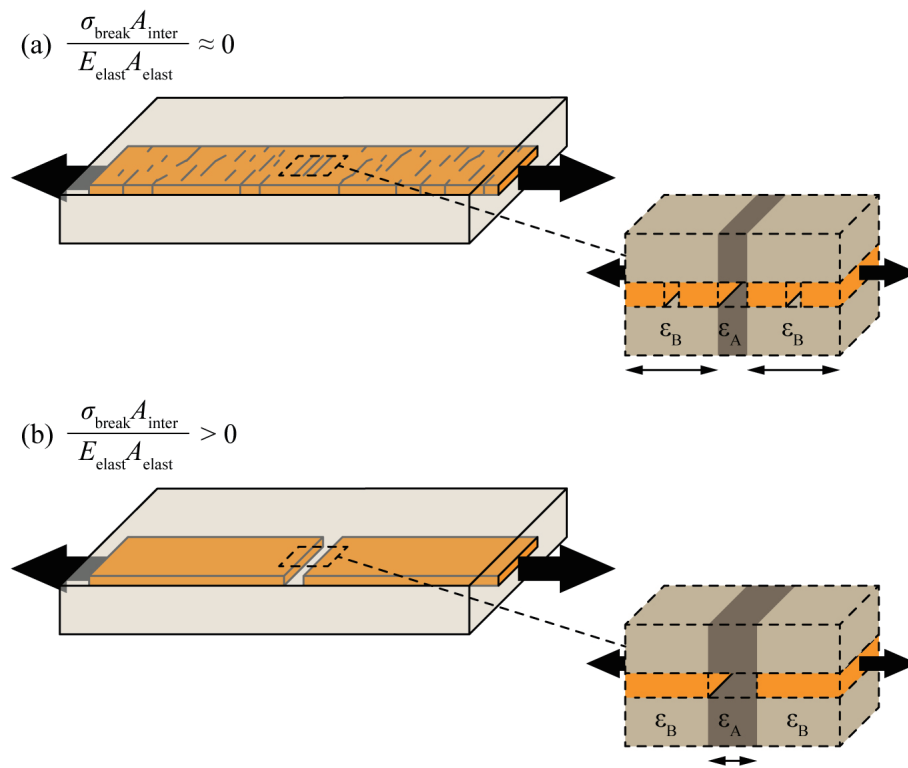


Figure 3.2 Schematic illustrations of crack configurations of stretched metal interconnect. (a) Multiple-crack growth type and (b) single-crack growth type.

elastomer is much larger than the elongation stiffness of metal interconnect), Equation (3.2) is

$$\varepsilon_A - \varepsilon_B = \frac{\sigma_{\text{break}} A_{\text{inter}}}{E_{\text{elast}} A_{\text{elast}}} \approx 0 \quad (3.3)$$

In this case,  $\varepsilon_A$  and  $\varepsilon_B$  show nearly the same value; therefore, other cracks are caused in the non-cracked region as the metal interconnect is stretched further, as shown in Figure 3.2a. In this research, this crack configuration is referred to as a multiple-crack growth type. When the ratio of the elongation is greater than zero (when the elongation stiffness of metal interconnect is much larger than the elongation stiffness of elastomer), a crack already caused in the metal interconnect increasingly propagates as the metal interconnect is stretched further, as shown in Figure 3.2b. This crack configuration is referred to as a single-crack growth type.

Table 3.1 Relationship between calculated values of elongation stiffness ratio and crack configurations, in previous studies and this research.

reference	structure	$\frac{\sigma_{\text{break}} A_{\text{inter}}}{E_{\text{elast}} A_{\text{elast}}}$	crack configuration
[84] (straight-shaped)	$t_{\text{inter}} = 0.05 \mu\text{m}$ (gold) $t_{\text{elast}} = 1 \text{ mm}$ (PDMS)	0.01	multiple
[85] (straight-shaped)	$t_{\text{inter}} = 0.05\text{--}0.1 \mu\text{m}$ (gold) $t_{\text{elast}} = 1 \text{ mm}$ (PDMS)	0.01–0.02	
[86] (straight-shaped)	$t_{\text{inter}} = 0.075 \mu\text{m}$ (gold) $t_{\text{elast}} = 0.3 \text{ mm}$ (PDMS)	0.06	
[87] (straight-shaped)	$t_{\text{inter}} = 0.035 \mu\text{m}$ (gold) $t_{\text{elast}} = 0.12 \text{ mm}$ (PDMS)	0.07	
[88] (straight-shaped)	$t_{\text{inter}} = 0.04 \mu\text{m}$ (gold) $t_{\text{elast}} = 0.076 \text{ mm}$ (PDMS)	0.12	
[53] (straight-shaped /wave-shaped)	$t_{\text{inter}} = 2.5\text{--}5 \mu\text{m}$ (gold) $t_{\text{elast}} = 0.4 \text{ mm}$ (PDMS)	1.44–2.88	single
[89] (wave-shaped)	$t_{\text{inter}} = 18 \mu\text{m}$ (copper) $t_{\text{elast}} = 1 \text{ mm}$ (PDMS)	2.76	
[90] (wave-shaped)	$t_{\text{inter}} = 17 \mu\text{m}$ (copper) $t_{\text{elast}} = 0.1 \text{ mm}$ (PDMS)	26.15	
This research	$t_{\text{inter}} = 0.04\text{--}1.17 \mu\text{m}$ (copper) $t_{\text{elast}} = 0.1 \text{ mm}$ (PU)	0.03–0.78	multiple/ single

### 3.2.2 Relationship between Elongation Stiffness Ratio and Crack Configuration in Previous Studies

To examine the relationship between the elongation stiffness ratio of metal interconnect and elastomer and the crack configurations, the value of the ratio was calculated with reference to previous studies. In the calculation, it is assumed that the widths of the metal interconnect and elastomer are considerably greater than the thicknesses of the metal interconnect and elastomer; therefore, Equation (3.2) is expressed as follows:

$$\varepsilon_A - \varepsilon_B = \frac{\sigma_{\text{break}} t_{\text{inter}}}{E_{\text{elast}} t_{\text{elast}}} \quad (3.4)$$

where  $t_{\text{inter}}$  and  $t_{\text{elast}}$  are the thicknesses of the metal interconnect and elastomer, respectively. Table 3.1 lists the calculated values of the elongation stiffness ratio using Equation (3.4). The values that are used in Table 3.1 are as follows:  $E_{\text{elast}}$  of PDMS was 1.3 MPa [91],  $\sigma_{\text{break}}$  of gold thin film was 0.3 GPa [92], and  $\sigma_{\text{break}}$  of copper thin film was 0.2 GPa [93]. Mechanical properties of bulk metals and metal thin films often show different values; these cited values are used in Table 3.1. Table 3.1 indicates that a multiple-crack growth type is often observed when the value of elongation stiffness is lower than approximately 0.1. A single-crack growth type is often observed when the value of elongation stiffness is higher than approximate unity.

## 3.3 Observation of Crack Configuration Transition

To verify the results of the theoretical analysis, metal interconnects with different elongation stiffness ratio were fabricated, and the cracks caused in the metal interconnect by the stretching deformation were observed. In this research, the elongation stiffness ratio was varied by changing the thickness of the metal interconnect. The shape of the metal interconnect was a straight-shaped conductive interconnect, and the metal interconnect thickness was in the range of 0.04–1.17  $\mu\text{m}$ . The metal interconnects were fabricated through a transfer method, where a deposited thin metal film was transferred on an elastomer. In previous studies, to form a metal interconnect in elastomer, a thin metal layer was often directly deposited on an elastomer layer by thermal or electron-beam deposition. An elastomer such as PU or PDMS, however, changes its mechanical property around the boundary between the thin metal layer and elastomer layer owing to thermal damage through deposition process. In this case, the mechanical property is unclear, and

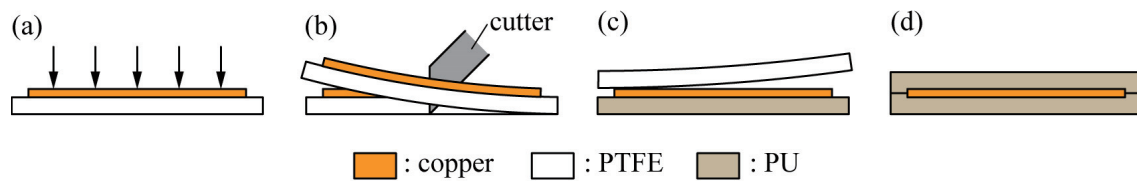


Figure 3.3 Fabrication of straight-shaped copper interconnect embedded in PU. (a) Thermal deposition of copper layer on PTFE sheet. (b) Cutting of PTFE sheet. (c) Transfer of copper interconnect onto PU tape. (d) Lamination of another PU tape.

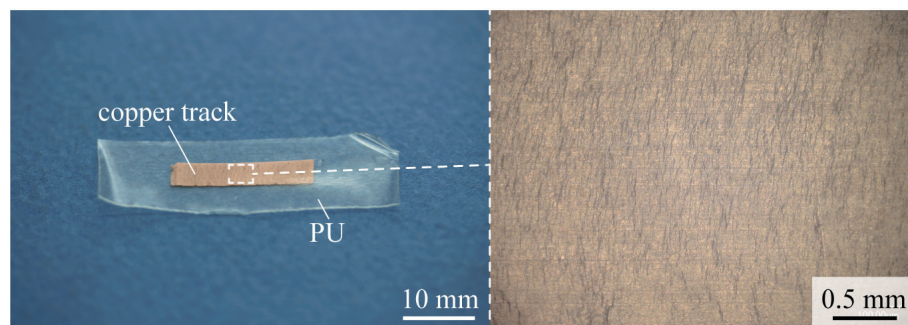


Figure 3.4 Optical images of fabricated copper interconnect embedded in PU.

it is difficult to understand the factors that determine the crack configurations. In both the thermal deposition and transfer methods, some microcracks might be pre-formed in the metal layer; however, the transfer methods are more effective because of a lack of thermal damage. Moreover, if there are pre-formed microcracks, they have slight effect on the crack configuration. For the multiple-crack growth type, new microcracks are caused in addition to the pre-formed microcracks. For the single-crack growth type, some of the pre-formed microcracks propagate and become large cracks. Therefore, in this research, a transfer method in which the metal interconnect layer is transferred onto the elastomer was used.

### 3.3.1 Fabrication

The fabrication process of a metal interconnect embedded in an elastomer is illustrated in Figure 3.3. Initially, a polytetrafluoroethylene (PTFE) sheet was cut into  $20 \times 30$  mm sheets, and a copper layer was deposited on these PTFE sheets by a thermal evaporation system (SVC-700TMSG/7PS80, Sanyu Electron), as shown in Figure 3.3a. The thickness of the metal interconnect,  $t_{\text{inter}}$ , was 0.04, 0.10, 0.18,



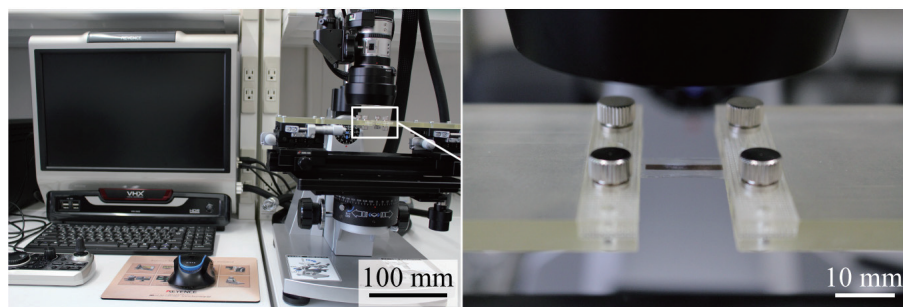


Figure 3.5 Optical Images of experimental setup.

0.53, and 1.17  $\mu\text{m}$ . The copper layer and the PTFE sheet were cut in the shape of a metal interconnect with a width of 3 mm, as shown in Figure 3.3b, and they were pasted onto a 0.05-mm-thick PU tape (Tegaderm 9534HP, 3M). The PTFE sheet was then peeled from the PU tape, and the copper layer was transferred from the PTFE sheet to the PU tape, as shown in Figure 3.3c. Finally, another PU tape was pasted on the copper interconnect layer (Figure 3.3d), and the PU layer was cut into a shape with a width of 10 mm, as shown in Figure 3.4e. For the fabricated samples, when the value of  $\sigma_{\text{break}}$  of copper thin film is 0.2 GPa [93] and  $E_{\text{elast}}$  of PU is 3 MPa, the calculated elongation stiffness ratio of each sample is 0.03, 0.07, 0.12, 0.35, and 0.78 at  $t_{\text{inter}} = 0.04, 0.10, 0.18, 0.53,$  and 1.17  $\mu\text{m}$ , respectively. Equation (3.4) is used in this calculation of elongation stiffness ratio.

### 3.3.2 Observation Setup

Figure 3.5 shows the setup for crack observation. A fabricated sample was mounted onto movable stages. The sample was stretched gradually by moving the stages, and the crack formation was observed with an optical microscope (VHX-2000, Keyence) when the elongation rate was 10%, 20%, 30%, 40%, and 50%, respectively. The elongation rate was calculated by dividing the initial distance between the stages by displacement of the movable stage.

### 3.3.3 Results and Discussions

A series of optical images of a cracked copper interconnect is depicted in Figures 3.6, 3.7, and 3.8.

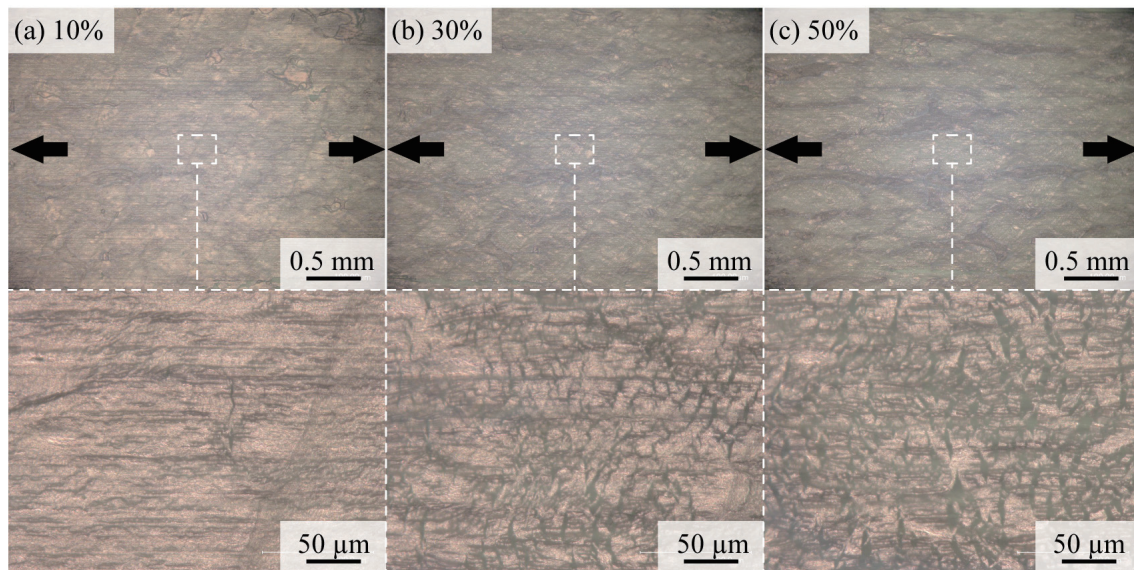


Figure 3.6 Series of optical images of cracked copper interconnect in PU with interconnect thicknesses of  $0.04 \mu\text{m}$  (the calculated elongation stiffness ratio was 0.03).

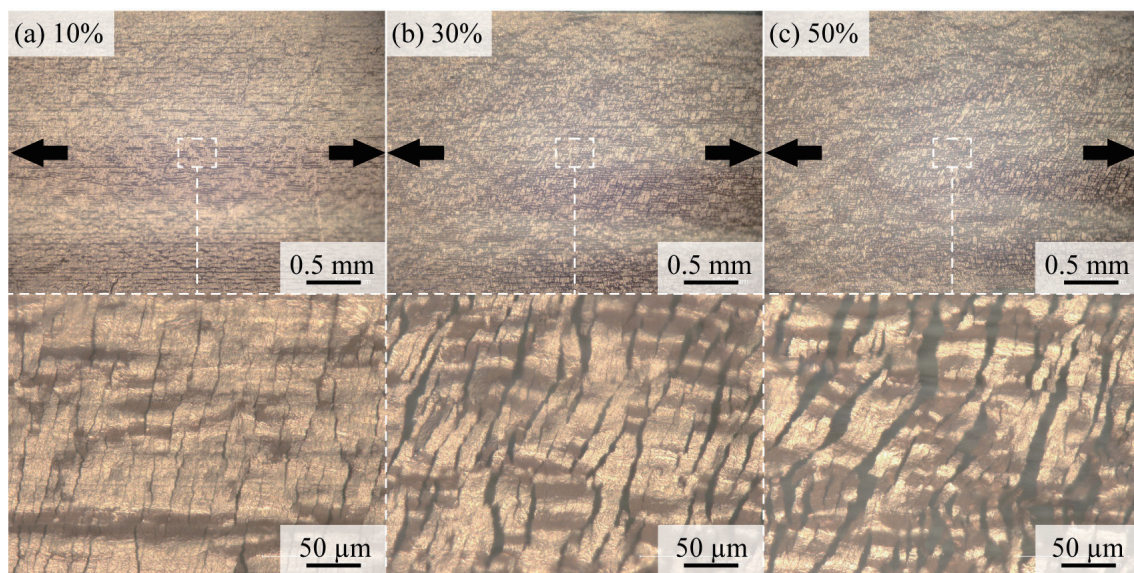


Figure 3.7 Series of optical images of a cracked copper interconnect in PU with interconnect thicknesses of  $0.10 \mu\text{m}$  (the calculated elongation stiffness ratio was 0.07).

Regarding a stretched interconnect with  $t_{\text{inter}} = 0.04 \mu\text{m}$  (the calculated elongation stiffness ratio was 0.03),

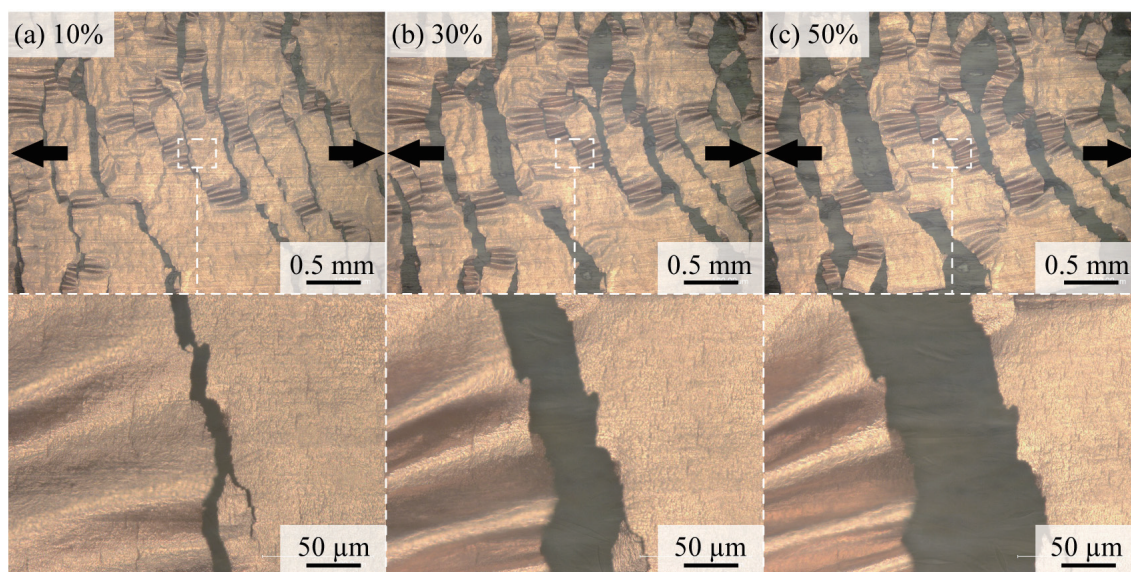


Figure 3.8 Series of optical images of cracked copper interconnect in PU with interconnect thicknesses of  $0.53 \mu\text{m}$  (the calculated elongation stiffness ratio was 0.35).

several smaller cracks were caused in the copper interconnect, as shown in Figures 3.6a–c. When the elongation rate was 10%, few cracks were caused in the copper interconnect, as shown in Figure 3.6a. As the elongation rate increased, new other cracks were caused, and the number of cracks increased, as shown in Figures 3.6b, c. This indicates that a crack configuration with  $t_{\text{inter}} = 0.04 \mu\text{m}$  shows a multiple-crack type. This result corresponds to the results of Table 3.1. In this case, the copper interconnect might be not completely broken and might be electrically conductive even if it was stretched up to several tens of percent. For a stretched interconnect with  $t_{\text{inter}} = 0.53 \mu\text{m}$  (0.35 was the calculated elongation stiffness ratio), several larger cracks were observed in the copper interconnect, as shown in Figures 3.8a–c. The cracks propagated along the interconnect's width direction, which was nearly perpendicular to the stretching direction. The crack width increased with an increase in the elongation rate, whereas the number of cracks was nearly constant. Regarding  $t_{\text{inter}} = 1.17 \mu\text{m}$  (0.78 was the calculated elongation stiffness ratio), a similar trend was observed. This indicates that the crack configuration for  $t_{\text{inter}} = 0.53$  and  $1.17 \mu\text{m}$  shows single-crack growth type, and this result also corresponds to the results of Table 3.1. In this case, the copper interconnect might be completely broken and lose its conductivity even when the elongation rate was under several percent because of the larger crack propagation. Regarding a cracked

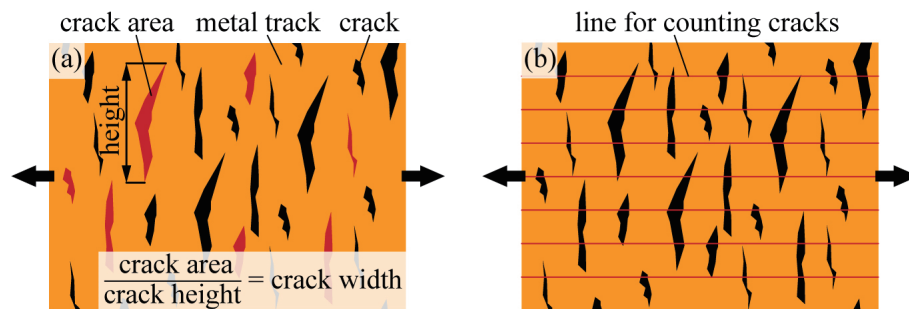


Figure 3.9 Schematic illustrations of (a) measurement of crack width and (b) number of cracks.

interconnect with  $t_{\text{inter}} = 0.10$  and  $0.18 \mu\text{m}$ , an intermediate type of crack configuration was observed, as shown in Figures 3.7a, b. Many microcracks occurred, and each crack propagated as the elongation rate increased.

In order to better understand crack configuration transition, a numerical analysis of the crack width and number of cracks was conducted. The crack width and number of cracks were measured from an optical image of a cracked copper interconnect, and the transitions of the crack width and number of cracks were analyzed. Figure 3.9 illustrates measurement of crack width and the number of cracks. The crack width was measured as follows: seven cracks were randomly selected on the optical image of a cracked copper interconnect, and the values of each crack area were measured. The crack width was calculated by dividing each area by the height of each crack; therefore, the calculated crack width means the average value of the crack width along the stretching direction. The number of cracks was calculated as follows: seven lines were drawn on an optical image of a cracked copper interconnect at regular intervals, as shown in Figure 3.9b, and the number of cracks across the line were counted. The direction of the line was along the stretching direction, and the line was drawn end-to-end on the optical image. The counted number was divided by the reference distance, which was  $100 \mu\text{m}$  for an elongation of 0%. Therefore, the calculated number of cracks is the average value of the reference distance. Figures 3.10a, b depict the results of numerical analysis of the crack width. As shown in Figure 3.10a, the crack widths regarding  $t_{\text{inter}} = 0.04$ ,  $0.10$ , and  $0.18 \mu\text{m}$  ranged from several micrometers to several tens of micrometers. The crack widths regarding  $t_{\text{inter}} = 0.53$  and  $1.17 \mu\text{m}$  ranged from several tens to hundreds of micrometers. Figure 3.10b depicts the normalized crack width by the value of the crack width at a 10% elongation rate. Regarding  $t_{\text{inter}} = 0.04 \mu\text{m}$ , the normalized crack width ranged from 1 to 2. However, for  $t_{\text{inter}} = 0.10$ ,  $0.18$ ,  $0.53$ , and

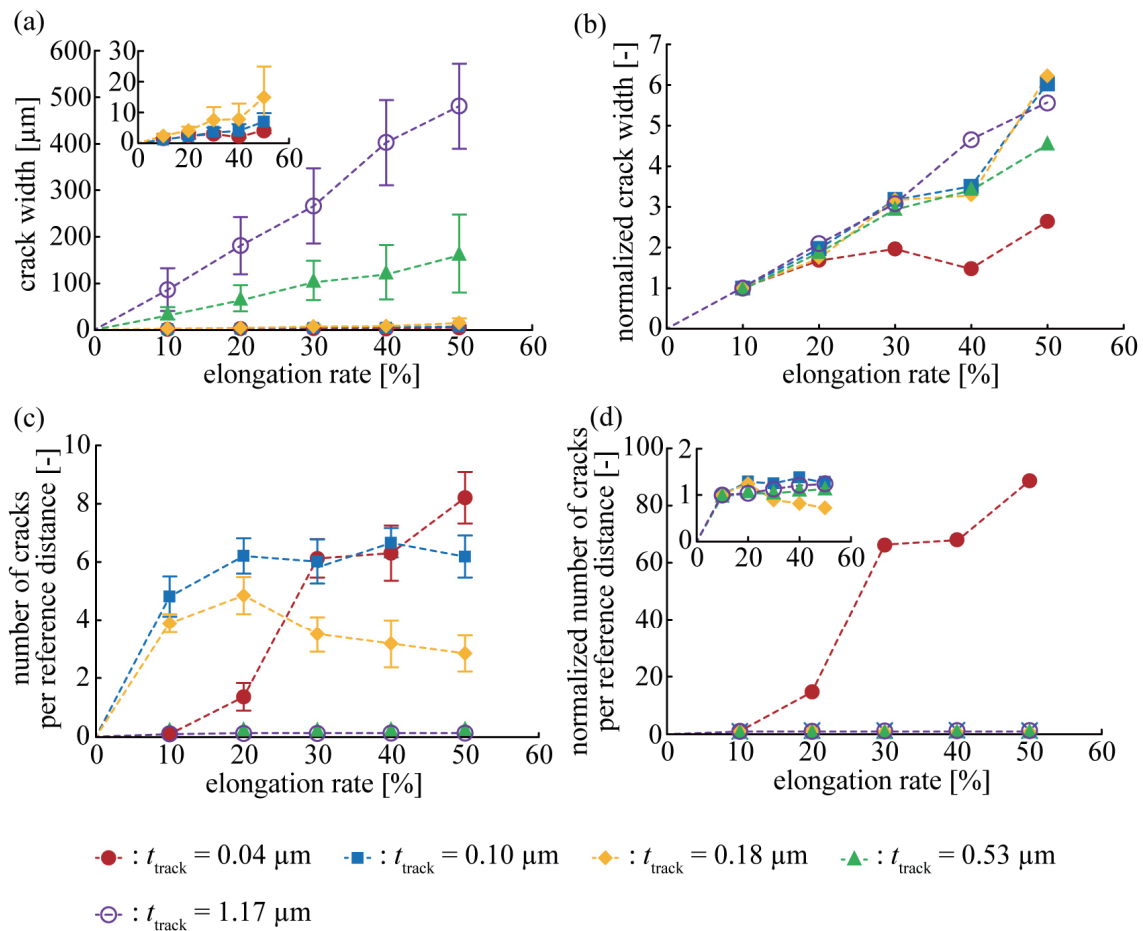


Figure 3.10 Relationship between (a) crack width and elongation rate, (b) normalized crack width and elongation rate, (c) number of cracks and elongation rate, and (d) normalized number of cracks and elongation rate. Reference distance was 100  $\mu\text{m}$  for elongation of 0%.

1.17  $\mu\text{m}$ , the normalized crack width increased almost linearly as the elongation rate increased. This indicates that the crack width is nearly constant or increases marginally as the elongation rate increases, when the crack configuration is the multiple-crack growth type. Conversely, when the crack configuration is the single-crack growth type, the crack width increases almost linearly. Figures 3.10c, d depict the results of numerical analysis of the number of cracks. The number of cracks per reference distance was more than one for  $t_{\text{inter}} = 0.04, 0.10,$  and  $0.18 \mu\text{m}$ . However, when  $t_{\text{inter}} = 0.53$  and  $1.17 \mu\text{m}$ , the number of cracks was approximately zero. Figure 3.10d depicts the normalized number of cracks by the value of the number of

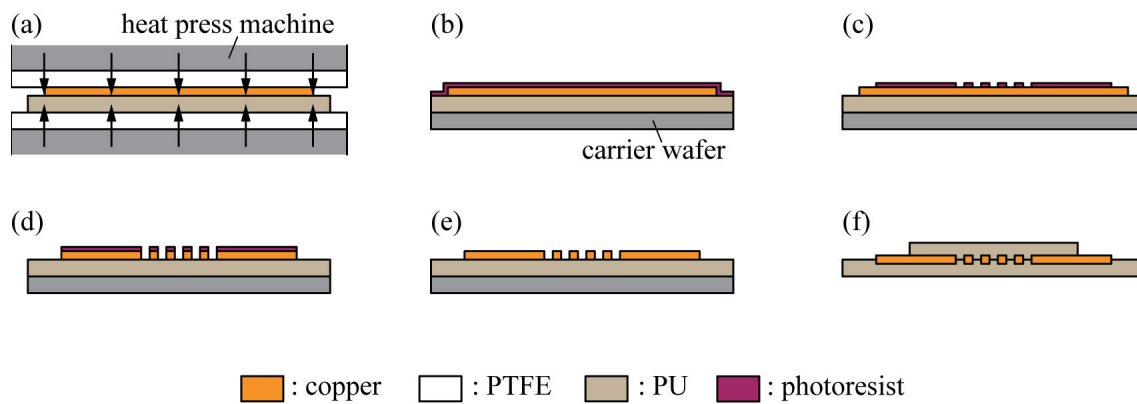


Figure 3.11 Fabrication of wave-shaped copper interconnect embedded in PU. (a) Lamination of copper foil on PU sheet. (b) Spin-coating of photoresist on copper foil. (c) Development and patterning of photoresist. (d) Wet-etching of copper foil. (e) Removal of photoresist. (f) Lamination of PU tape on structured copper.

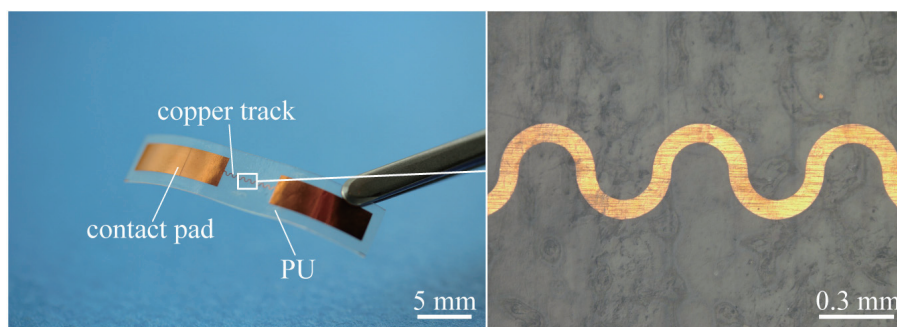


Figure 3.12 Optical images of wave-shaped copper interconnect in PU.

cracks at a 10% elongation rate. When  $t_{\text{inter}} = 0.04 \mu\text{m}$ , the normalized number of cracks increased from approximately 1–90 as the elongation rate increased. However, for  $t_{\text{inter}} = 0.10, 0.18, 0.53,$  and  $1.17 \mu\text{m}$ , the normalized number was nearly constant at unity. That indicates that when the crack configuration is the multiple crack-growth type, the number of cracks increases suddenly as the elongation rate increases. Conversely, when the crack configuration is the single-crack growth type, the number of cracks is nearly constant.

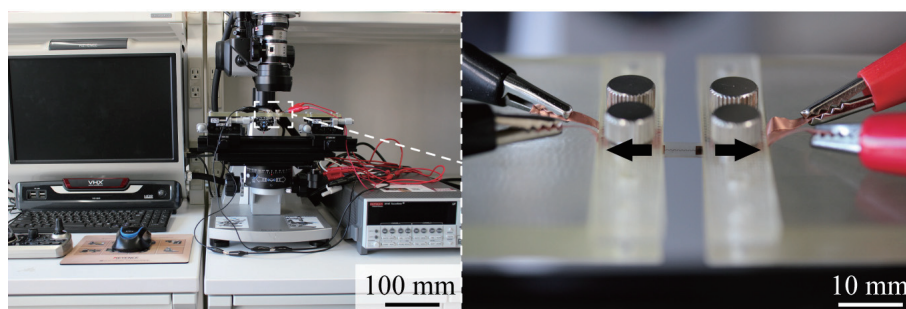


Figure 3.13 Optical images of experimental setup.

### 3.4 Measurement of Crack Width and Breaking Elongation

To measure the breaking elongation and crack width of a metal interconnect with a single crack growth, wave-shaped metal interconnects with a single crack growth were fabricated and the cracks were observed. The required voltage for a self-healing ability using the dielectrophoresis of metal nanoparticles depends on the crack width; therefore, the crack width is an important parameter for self-healing. Furthermore, the breaking elongation is also an important parameter for flexible devices. This research focused on the thickness of the metal interconnect and the thickness of the elastomer; therefore, a metal interconnect with different thicknesses of metal interconnect and elastomer was used in the measurement. In the measurement, copper and PU were used for the metal interconnect and elastomer, respectively.

#### 3.4.1 Fabrication

Figure 3.11 illustrates the fabrication process for a wave-shaped copper interconnect. Initially, rolled copper foils (Nilaco) of various thicknesses (2, 4, 6, 8, and 10  $\mu\text{m}$ ) were thermally laminated onto a PU sheet (Platilon 4201, Covestro AG), as shown in Figure 3.11a. The thickness of the PU sheet was 0.05, 0.1, 0.15, and 0.2 mm. In the lamination process, the copper foil was surface-modified by a plasma cleaner (PDC-32G, Harrick Plasma). The copper foil and PU sheet were heated at 100  $^{\circ}\text{C}$  for 3 min without pressure and were then pressed at approximately 0.4 MPa at 170  $^{\circ}\text{C}$  for 3 min. Subsequently, the copper foil was patterned to the wave-shape through a photolithography process. Photoresist was spin-coated onto the copper foil as shown in Figure 3.11b and patterned into a wave-shaped interconnect and contact pads

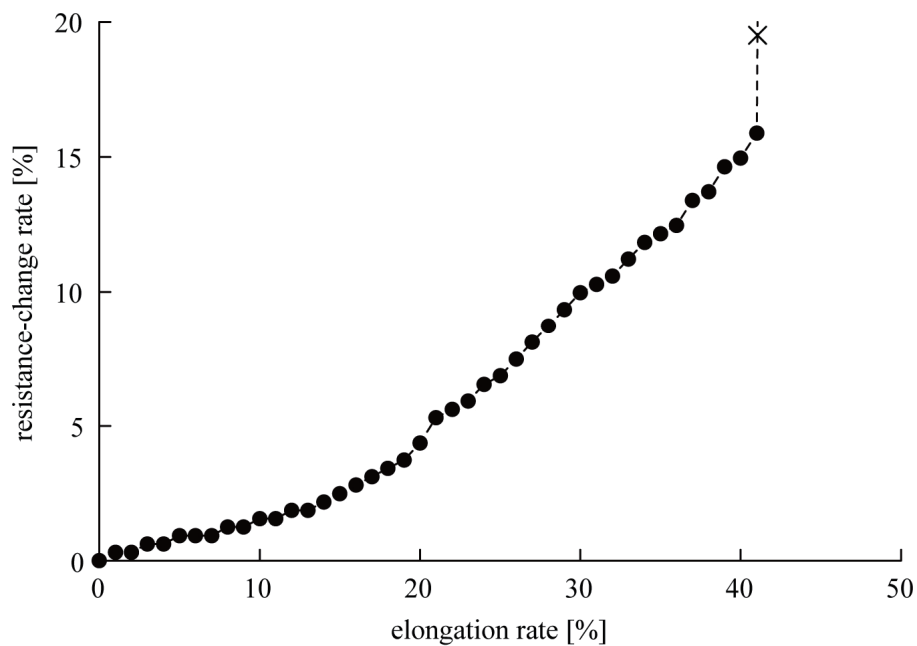


Figure 3.14 Relationship between resistance-change rate and elongation rate for wave-shaped copper interconnect (6  $\mu\text{m}$  in copper thickness and 50  $\mu\text{m}$  in PU substrate thickness).

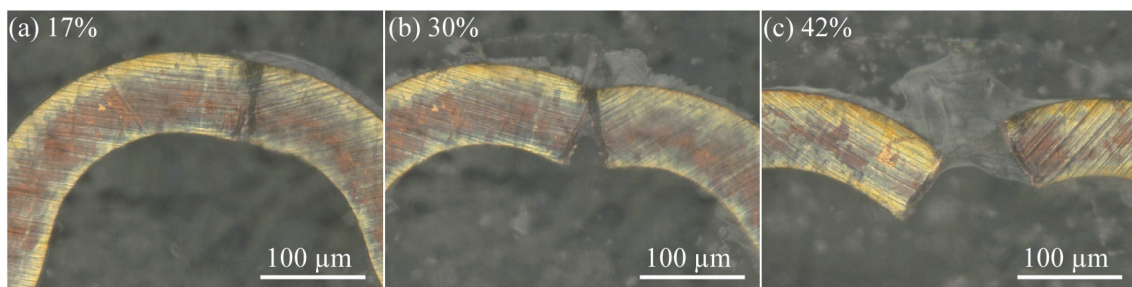


Figure 3.15 Enlarged optical images of broken point of wave-shaped copper interconnect (6  $\mu\text{m}$  in copper thickness and 50  $\mu\text{m}$  in PU substrate thickness).

(Figure 3.11c). Further, the copper layer was wet-etched as shown in Figure 3.11d, and the photoresist was removed (Figure 3.11e). After the photolithography process, a PU tape was laminated only on the wave-shaped copper interconnect, as shown in Figure 3.11f. Finally, the individual samples were separated. Figure 3.12 depicts the fabricated wave-shaped copper interconnect, which is embedded in a PU. The dimensions of each sample were 25 mm by 5 mm. The width of the copper interconnect was 0.1 mm, and



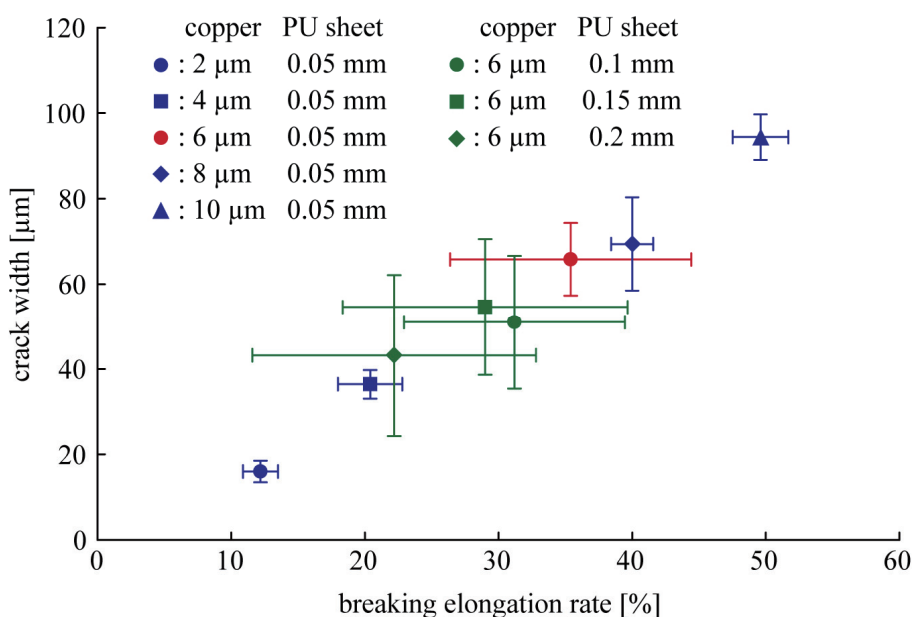


Figure 3.16 Relationship between breaking elongation rate and crack width of wave-shaped copper interconnect.

it was arranged between two large contact pads that were 5 mm apart. The radius of the copper interconnect was 0.15 mm. The calculated elongation stiffness ratio of each sample was 0.89-4.45, when the values of  $\sigma_{\text{break}}$  of copper thin film was 0.2 GPa [93] and the  $E_{\text{elast}}$  values of the PU tape and PU sheet were 3 and 6 MPa, respectively. In this calculation of elongation stiffness ratio, Equation (3.4) was used.

### 3.4.2 Measurement Setup

Figure 3.13 shows the experimental setup. A fabricated sample were mounted onto movable stages. The sample was clamped at the contact pads and electronically connected to a source meter (2614B, Keithley Instruments). The resistance of the wave-shaped interconnect was measured by four probe methods for detecting crack propagation. The sample was stretched gradually by moving the stages. The crack formation was observed with an optical microscope (VHX-2000, Keyence).

### 3.4.3 Results and Discussion

Figure 3.14 depicts the resistance-change rate in terms of the elongation rate, for a wave-shaped copper

interconnect with single-crack growth type. The copper thickness and PU substrate thickness were 6  $\mu\text{m}$  and 50  $\mu\text{m}$ , respectively. The resistance-change rate gradually increased as the elongation rate increased, and the resistance sharply increased at 42% of the elongation rate. That indicates that the copper interconnect was completely broken. Optical images as shown in Figure 3.15 depict crack propagation of the copper interconnect. When stretching deformation was gradually applied to the copper interconnect, some crack initiations were observed around the apex of the wave shape as shown in Figure 3.15a. Each crack gradually propagated as the elongation rate increased along the direction of the copper interconnect width as shown in Figure 3.15b. This indicates that the resistance rate was increased by crack propagation in Figure 3.14. The copper interconnects were completely broken, when the crack propagated completely as shown in Figure 3.15c. The crack configuration was the single-crack growth type in both cases.

Figure 3.16 shows the relationship between the breaking elongation and the crack width for each sample of the wave-shaped copper interconnect. The breaking elongation was several tens of percent, and the crack width was several tens of micrometers. For the sample with different thicknesses of copper interconnect, the breaking elongation increased significantly as the thickness of the copper interconnect increased. For the sample with different thicknesses of elastomer, the breaking elongation decreased as the thickness of the elastomer increased. For the relationship between the breaking elongation and the crack width, the crack width almost linearly increased as the breaking elongation increased. This indicated that a larger elongation caused a higher strain energy in the copper interconnects, and wider cracks were caused when the higher energy was released by the breaking of the copper interconnects.

### 3.5 Summary

---

Factors determining the crack configurations of a stretched metal interconnect embedded in an elastomer were studied by both theoretical analysis and experiments. In the theoretical analysis section, theoretical calculation results indicated that the crack configurations were determined by the elongation stiffness ratio of the metal interconnect and the elastomer and are classified into two types: a multiple-crack and single-crack growth types. With reference to previous studies, it was indicated that a multiple-crack growth type is often observed when the elongation stiffness ratio is lower than approximately 0.1, and that a single-crack growth type is often observed when the elongation stiffness ratio is higher than approximately unity. In the experiments section, first, to verify the calculation results of the theoretical analysis, straight-shaped copper interconnects with  $t_{\text{inter}} = 0.04\text{--}1.17 \mu\text{m}$  (the elongation stiffness ratio is 0.03–0.78) were fabricated,

and cracks caused by stretching deformation were observed. As a result, the multiple-crack growth type was observed when  $t_{\text{inter}} = 0.04 \mu\text{m}$ , and the crack configuration gradually changed to a single crack as  $t_{\text{inter}}$  increased. This corresponds to the result of the theoretical analysis. Second, wave-shaped metal interconnects of the single-crack growth type were fabricated, and the breaking elongation and width of the crack were measured. This research focused on the thickness of the metal interconnect and the thickness of the elastomer; therefore, a wave-shaped copper interconnect with different thicknesses of metal interconnect and elastomer was fabricated and stretched. As a result, the breaking elongation was several tens of percent, and the crack width was several tens of micrometers. For the sample with different thicknesses of copper interconnect, the breaking elongation increased significantly as the thickness of the copper interconnect increased. For the sample with different thicknesses of elastomer, the breaking elongation decreased as the thickness of the elastomer increased. Additionally, the crack width almost linearly increased as the breaking elongation increased.

# Chapter 4 Flexible Device using Self-Healing Metal Interconnect

## 4.1 Introduction

---

Based on the results of Chapter 2 and Chapter 3, flexible devices using self-healing metal interconnect were developed. By controlling the crack configurations of the device's metal interconnects to a single-crack growth type and forming a nanoparticle chain in a large crack (several tens of micrometers) of one of the metal interconnects, the self-healing metal interconnect was applied to flexible devices using the dielectrophoresis of metal nanoparticles. In this chapter, first, to verify the self-healing of a metal interconnect broken by stretching deformation and to evaluate the healing property under cyclic stretching deformation, wave-shaped metal interconnects with a self-healing ability were fabricated, and the impedance changes under the stretching deformation were measured. To evaluate the healing property, the following parameters were studied: breaking elongation, impedance of a metal interconnect after self-healing, and healing time. Second, a flexible device, which was composed of self-healing metal interconnects and surface-mounted light emitting diode (LED) chips was developed, and the applicability of self-healing metal interconnects to flexible electric devices was demonstrated.

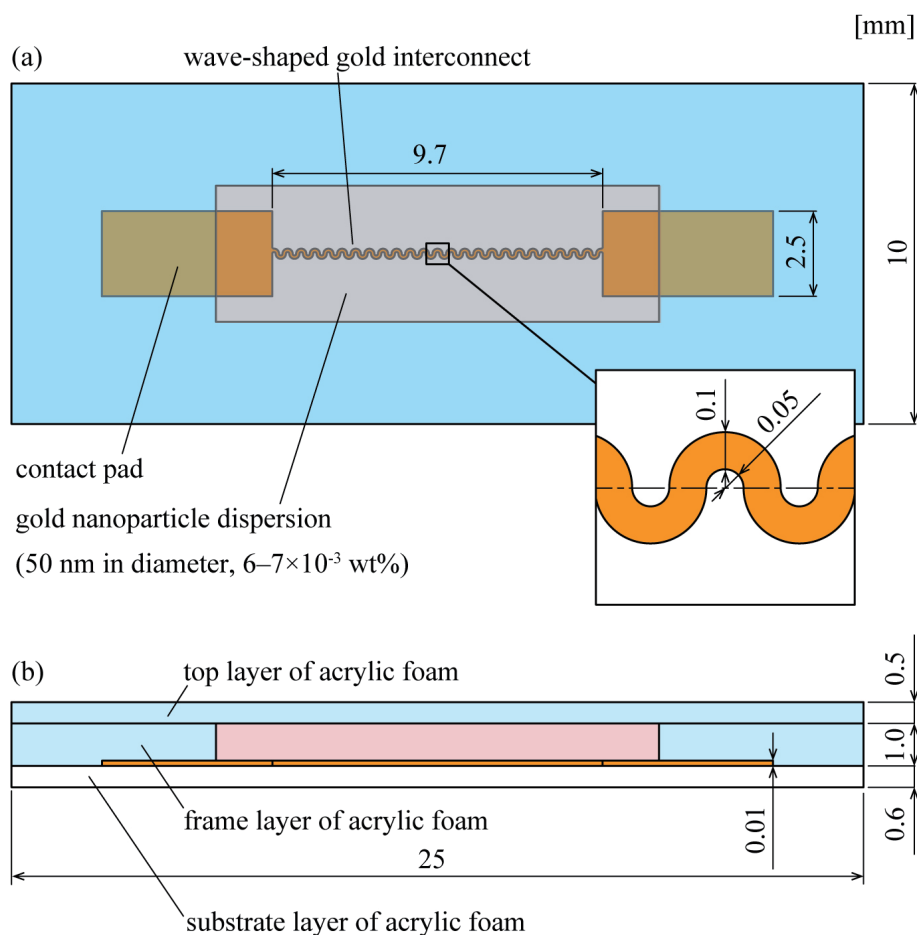


Figure 4.1 Dimensions of self-healing gold interconnect for evaluation of self-healing property. (a) Top view and (b) Cross-sectional view.

## 4.2 Healing Property Evaluation under Cyclic Stretching Deformation

To verify the self-healing of a metal interconnect broken by stretching deformation and to evaluate the healing property under cyclic stretching deformation, self-healing metal interconnects were fabricated, and their impedance changes under the stretching deformation were measured. In this research, gold, acrylic form (AF), and gold nanoparticle dispersion were used as a metal interconnect, an elastomer, and

metal nanoparticle dispersion, respectively, because of their availability and chemical stability.

#### 4.2.1 Design

Figure 4.1 depicts the dimensions of a self-healing gold interconnect fabricated to evaluate the self-healing property. A wave-shaped gold interconnect on a substrate layer of AF was covered with gold nanoparticles in a citrate-buffered aqueous medium (50 nm in diameter), and the gold nanoparticle dispersion was encapsulated with a frame layer and a top layer of AF. The width and radius of the wave shape and the thickness of the gold interconnect were 0.1 mm, 0.1 mm, and 0.01 mm, respectively. Contact pads were fabricated at both ends of the gold interconnect to obtain electrical contact to a measurement system. The distance between the contact pads was 9.7 mm, and the width of the contact pads was 2.5 mm. Regarding each layer of AF, the thickness of the substrate, frame, and top layers was 0.6 mm, 1.0 mm, and 0.5 mm, respectively. The breaking stress of gold was 0.2 GPa, and the Young's modulus of AF was 1.8 MPa; therefore, the elongation stiffness ratio of the gold interconnect and the substrate layer was 1.9. In this case, the crack configuration of the gold interconnect was of a single-crack growth type; hence, a single large crack (several tens to hundreds of micrometers in crack width) was formed in the gold interconnect by stretching deformation. Regarding gold nanoparticle dispersions, the diameter was 50 nm, and the mass ratio of the gold was  $6\text{--}7 \times 10^{-3}$  wt%. To form a nanoparticle chain in the crack of the broken gold interconnect, approximately 20 V<sub>rms</sub> of voltage was applied, and the current flowing just when nanoparticles bridged a crack was controlled to 3–4 mA<sub>rms</sub>.

#### 4.2.2 Fabrication

Self-healing gold interconnects were fabricated as illustrated in Figure 4.2. First, 10- $\mu\text{m}$ -thick rolled gold foil (AU-173175, Nilaco) was ruminated to an adhesive sheet (Figure 4.2a), and the gold foil was patterned to a wave shape with contact pads by laser cutting (Figure 4.2b). Second, the unnecessary gold foil was peeled off with tweezers, as shown in Figure 4.2c, and the patterned gold foil was transferred to an 0.6-mm-thick acrylic form adhesive tape (Y-4930, 3M) as a substrate layer. Then, electrical wirings for electrical contact to a measurement system were laminated on the contact pads. A 1.0-mm-thick acrylic form tape (Y-4910, 3M) patterned to the shape of a frame layer was laminated as shown in Figure 4.2e. Gold nanoparticles in a citrate-buffered aqueous medium with a diameter of 50 nm (Au colloid solution-SC 50 nm, Tanaka Kikinzoku Kogyo) were dropped into the frame layer. Finally, a 0.1-mm-thick acrylic

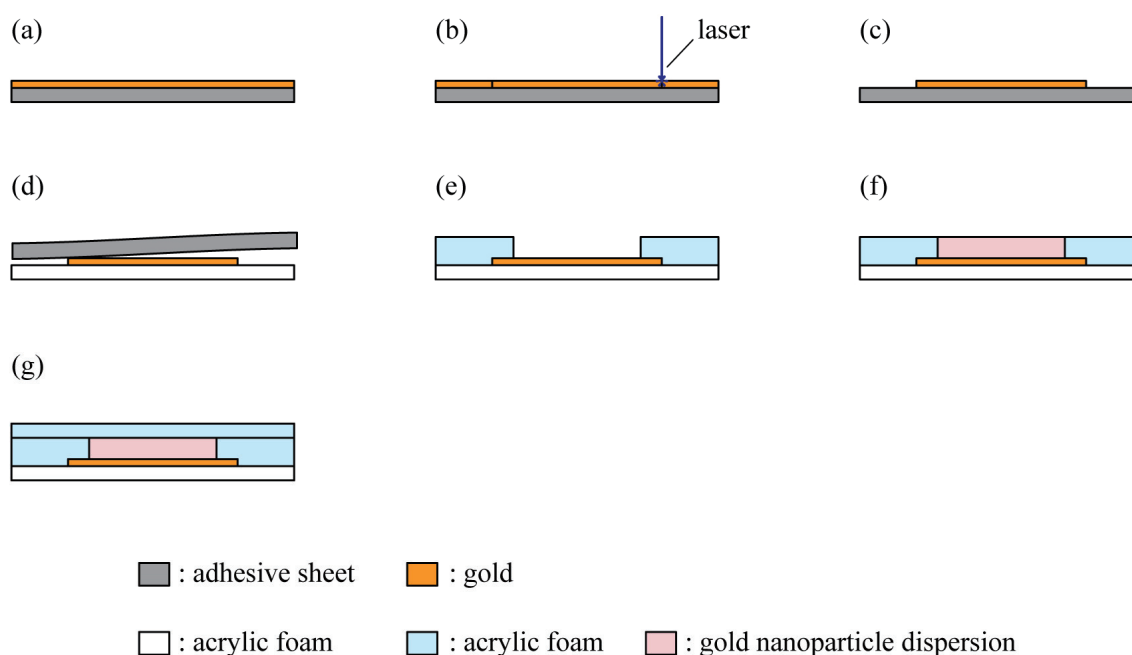


Figure 4.2 Schematic of fabrication process of self-healing gold interconnect. (a) Laminating rolled gold foil onto adhesive sheet. (b) Patterning gold foil to wave shape and contact pads by laser cutting. (c) Peeling off unnecessary gold foil. (d) Transferring patterned gold onto AF adhesive tape as substrate layer. (e) Laminating frame layer. (f) Dropping gold nanoparticle dispersion into flame layer. (g) Laminating top layer.

form tape was laminated as a cover layer on the flame layer. Figure 4.3 shows optical images of a fabricated gold interconnect. Only the wave-shaped gold interconnect was covered with the gold nanoparticle dispersion as designed.

### 4.2.3 Measurement Setup

Figure 4.4 shows the measurement setup used to evaluate the healing property. A fabricated self-healing gold interconnect was mounted on electrical movable stages (SGSP20-85, Sigma Koki), and stretching deformation was gradually induced in the self-healing gold interconnect while measuring its impedance change. The stages were connected to a stage controller (SOHT-204MS, Sigma Koki) to adjust and obtain the value of stage displacement,  $d$ . A resistor (4.6 k $\Omega$  in resistance) was connected to the self-healing gold interconnect in series to control the current flowing after nanoparticles bridged the broken point of the

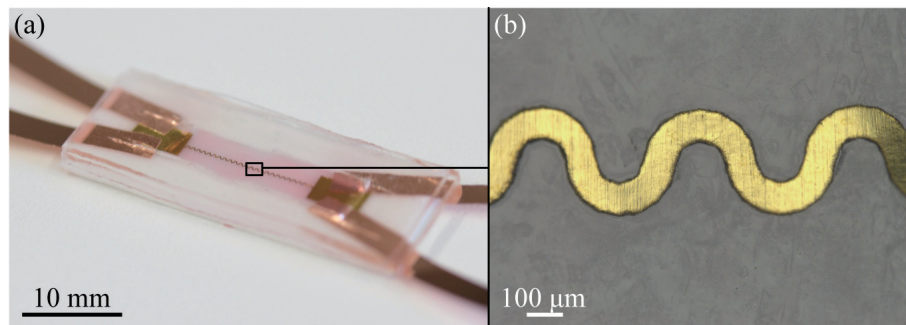


Figure 4.3 (a) Optical image of self-healing gold interconnect, and (b) enlarged view of gold interconnect on AF layer.

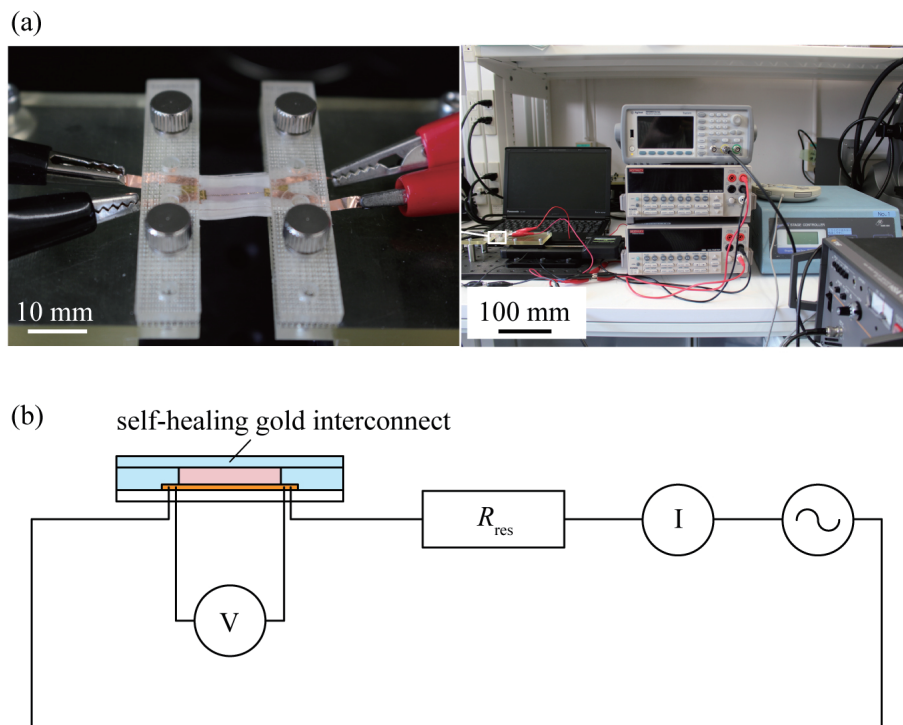


Figure 4.4 Optical images and schematic of measurement setup. (a) Optical images of measurement setup. (b) Schematic of measurement setup.

interconnect. An AC voltage (28 or 32  $V_{\text{rms}}$  in amplitude and 100 kHz in frequency) was applied to the self-healing gold interconnect and the resistor; therefore, 2.3 or 2.6  $mV_{\text{rms}}$  was applied to the self-healing



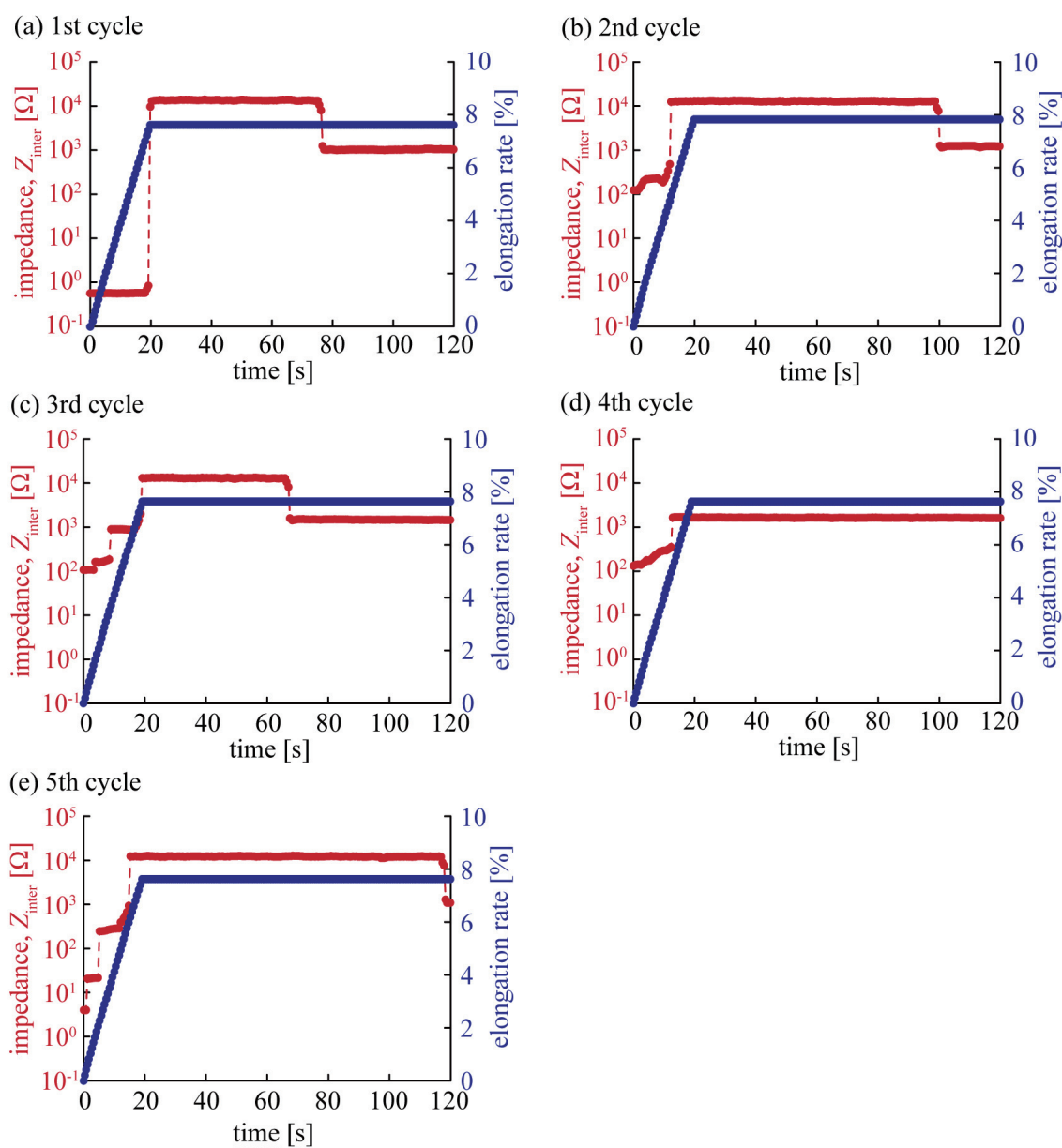


Figure 4.5 Time variation of impedance of self-healing gold interconnect,  $Z_{inter}$ , and elongation of self-healing gold interconnect during (a) first cycle, (b) second cycle, (c) third cycle, (d) fourth cycle, and (e) fifth cycle.

gold interconnect when the interconnect was not broken, and 19 or 22  $V_{rms}$  was applied to the self-healing gold interconnect when the interconnect was broken. To measure changes in the impedance of the self-

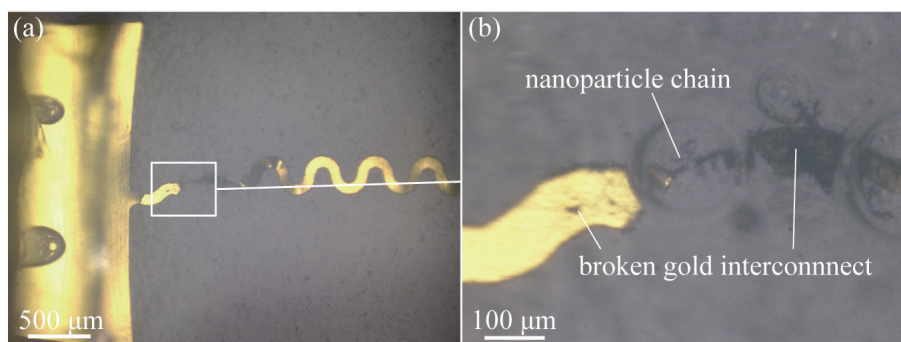


Figure 4.6 Optical images of broken and healed point of wave-shape gold interconnect covered with gold nanoparticle dispersion. (a) Optical image of healed point. (b) Enlarged view of healed point.

healing gold interconnect,  $Z_{\text{inter}}$ , the values of the voltage applied to the gold interconnect,  $V_{\text{inter}}$ , and current,  $I$ , were measured with digital multimeters (2000, Keithley Instruments).  $Z_{\text{inter}}$  was calculated as  $V_{\text{inter}}/I$ . The stage controller and the digital multimeters were connected to a laptop PC with GPIB cables, and they were controlled with measurement software to obtain the values of  $d$ ,  $V_{\text{inter}}$ , and  $I$  at regular intervals of approximately 0.5 ms. The value of  $d$  was also controlled by the software, and the change rate of  $d$  was 40  $\mu\text{m/s}$ . The elongation of the wave-shaped interconnect was calculated by dividing  $d$  with the distance between each contact pad. When the metal interconnect was broken and  $Z_{\text{inter}}$  increased sharply, the movement of the stage was stopped. After the measurement, the stage was moved to its initial position, and the same measurement was repeated five times.

#### 4.2.4 Results and Discussion

The series of graphs depicted in Figure 4.5 shows the time variation of  $Z_{\text{inter}}$  and the elongation rate of a self-healing gold interconnect when 32  $V_{\text{rms}}$  of voltage was applied to the interconnect and resistor. In the first cycle as shown in Figure 4.5a,  $Z_{\text{inter}}$  increased sharply from 0.58  $\Omega$  to 13  $\text{k}\Omega$  when the elongation rate was 7.6%. This indicates that the self-healing gold interconnect was broken and lost its conductivity. On the other hand,  $Z_{\text{inter}}$  decreased sharply from 13  $\text{k}\Omega$  to 1.1  $\text{k}\Omega$  at 77 s. This was because a broken point of the self-healing gold interconnect was electrically connected to gold nanoparticle chains formed by an applied voltage, as shown in Figure 4.6. Hence, this verifies that a metal interconnect broken by stretching deformation can be healed with its self-healing ability using the dielectrophoresis of metal nanoparticles.

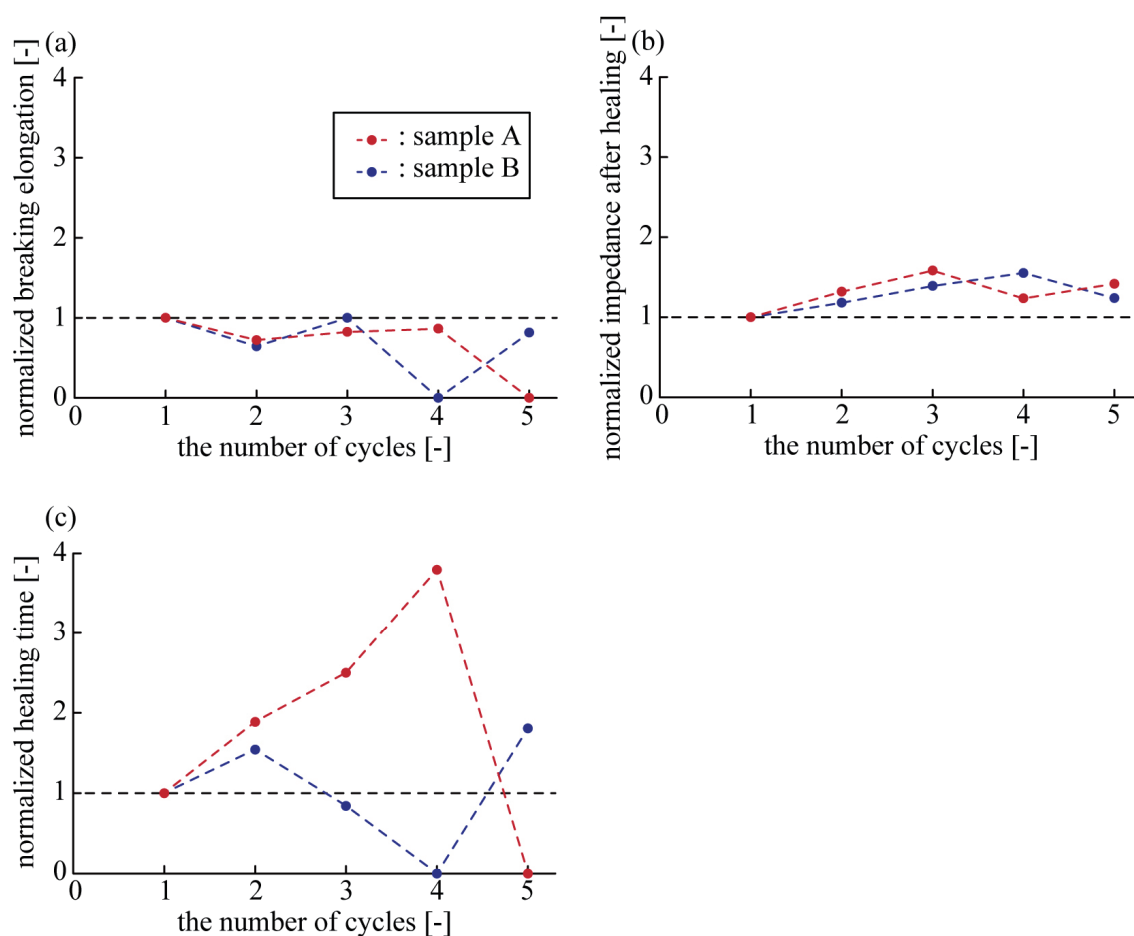


Figure 4.7 Change in breaking elongation, impedance after healing, and healing time in terms of number of stretching cycles for sample A and sample B. Each value was normalized with the value of the first cycle. (a) Normalized breaking elongation. (b) Normalized impedance after self-healing. (c) Normalized healing time.

In Figure 4.6, some microbubbles are observed around the broken point of the self-healing gold interconnect. This indicates that the medium around the nanoparticle chains evaporated by Joule heating, which was caused by current. Regarding the second cycle as shown in Figure 4.5b, compared with  $Z_{\text{inter}}$  at the end of first cycle as shown in Figure 4.5a,  $Z_{\text{inter}}$  decreased from 1.1 k $\Omega$  to 0.12 k $\Omega$  around the beginning of the measurement. This indicates that the broken point of the self-healing gold interconnect was physically contacted. The self-healing gold interconnect was broken and  $Z_{\text{inter}}$  increased sharply again when the elongation rate was 4.9%; this value was lower than that during breaking elongation of the first

cycle. Approximately 88 s later,  $Z_{\text{inter}}$  decreased sharply again from 13 k $\Omega$  to 1.2 k $\Omega$ . This indicates that the self-healing gold interconnect was healed again. Following this, it was confirmed that the broken point was healed in the same way as the first cycle. This indicates that the healed point of the self-healing gold interconnect was mechanically weak; therefore, the breaking-and-healing process was repeated at the first broken point. Regarding the fourth cycle,  $Z_{\text{inter}}$  increased from 0.35 k $\Omega$  to 1.7 k $\Omega$  when the elongation rate was 5.2%. Meanwhile,  $Z_{\text{inter}}$  was 1.7 k $\Omega$  after self-healing; hence, the gold interconnect was not broken in the fourth cycle. This is because the nanoparticle chain formed in the broken point kept bridging and was electrically connected.

Figure 4.7 shows changes in the breaking elongation, impedance after healing, and healing time in terms of the number of stretching cycles. The voltage applied to the interconnect and resistor was 28 and 32 V<sub>rms</sub> for samples A and B, respectively. Each measured value was normalized with the value of the first cycle. Regarding the breaking elongation, each value was lower than that of the first cycle in both cases of samples A and B. This indicates that the healed part was mechanically weak; therefore, the healed part was easily broken compared with the first cycle. Regarding the impedance after healing, each value was higher than those in the first cycle in both cases of samples A and B. This could be because the length of the nanoparticle chain increased as the number of stretching cycles increased. Regarding the healing time, each value takes both higher and lower values than those in the first cycle randomly in both cases of sample A and sample B. In the case of a lower value, it is considered that the broken nanoparticle chain remained at the broken point and the other nanoparticles were attracted and trapped on the remaining nanoparticle chain; therefore, the healing time decreased. On the other hand, in the case of a higher value, the growing nanoparticle chain could have been broken by Joule heating. The broken nanoparticle chain kept growing and finally bridged; therefore, it took more time.

### 4.3 Demonstration of Flexible Device using Self-Healing Metal Interconnect

---

To demonstrate the applicability of a self-healing metal interconnect using dielectrophoresis of metal nanoparticles to flexible devices, a flexible device using a self-healing metal interconnect was developed. In this research, the flexible device was composed of self-healing metal interconnects and surface-mounted LED chips. As for the self-healing metal interconnects, gold, AF, and gold nanoparticle dispersion were used as metal, elastomer, and metal nanoparticle dispersion similar to those used in the healing property

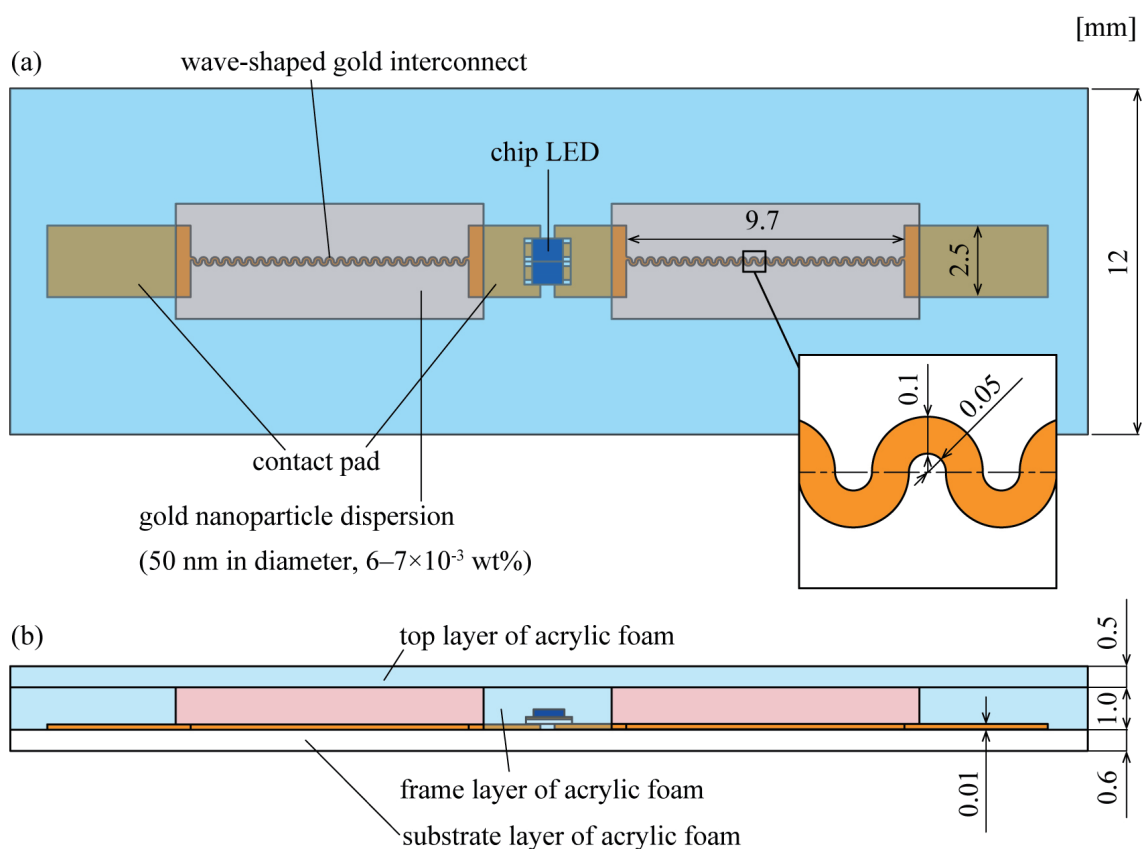


Figure 4.8 Dimensions of flexible device, which is composed of self-healing gold interconnects and surface-mounted LED chips. (a) Top view and (b) Cross-sectional view of flexible device.

evaluation.

#### 4.3.1 Design

Figure 4.8 illustrates the dimensions of the flexible device, which is composed of self-healing gold interconnects and surface-mounted LED chips. As with the healing property evaluation, wave-shaped gold interconnects were covered with gold nanoparticles in the device. The gold nanoparticle dispersion was encapsulated with the substrate, frame, and top layers of AF. As for the self-healing gold interconnect, the design parameters were the same as that used in the healing property evaluation (width and radius of 0.1 mm and thickness of 0.01 mm). Contact pads were also fabricated at both ends of the gold interconnect to obtain electrical contact to the surface-mounted LED chips and the measurement system. The distance

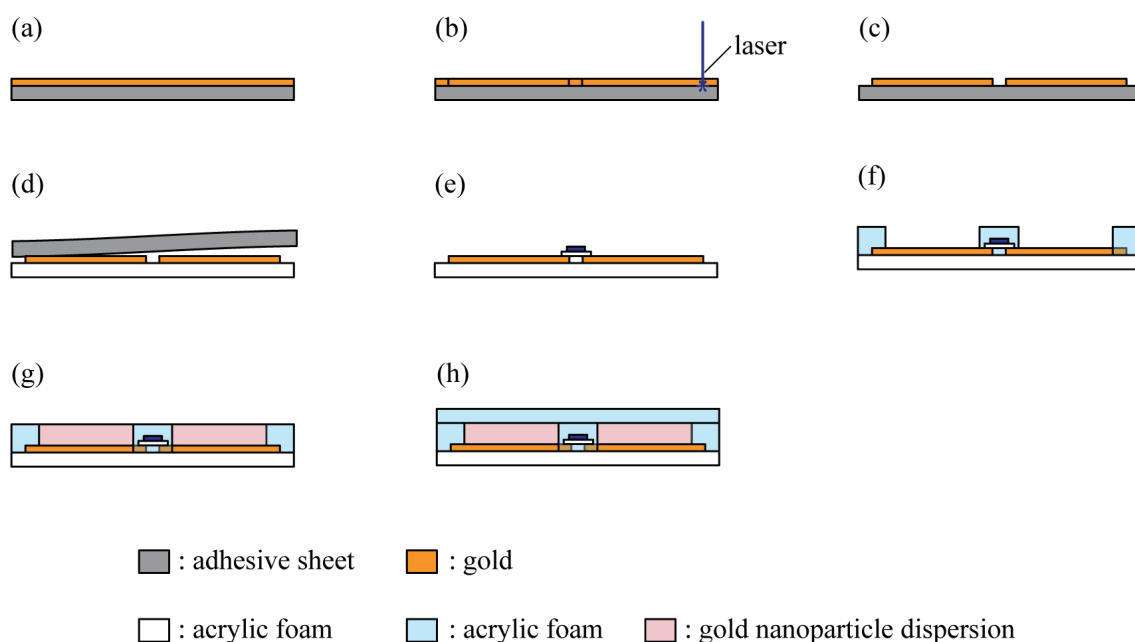


Figure 4.9 Schematic of fabrication process of flexible device, which is composed of self-healing gold interconnects and surface-mounted LED chips. (a) Laminating rolled gold foil onto adhesive sheet. (b) Patterning gold foil to wave shape and contact pads by laser cutting. (c) Peeling off unnecessary gold foil. (d) Transferring patterned gold onto acrylic form adhesive tape as substrate layer. (e) Soldering surface-mounted LED chips with solder paste. (f) Laminating frame layer. (g) Dropping gold nanoparticle aqueous into frame layer. (h) Laminating top layer.

between the contact pads was 9.7 mm and the width of the contact pads was 2.5 mm. Two LED chips were mounted with opposite polarities; hence, the LED chips emitted light even when AC voltage was applied. The thickness of each layer of AF was also the same as that of the self-healing gold interconnect used in the healing property evaluation (0.6 mm of the substrate layer, 1.0 mm of the frame layer, and 0.5 mm of the top layer). In this design, the elongation stiffness ratio of the gold interconnect and the substrate layer of AF was 1.9; therefore, the crack configuration was of a single crack growth type. A single large crack was formed in one of the gold interconnects by stretching deformation. As for the gold nanoparticle dispersions, the diameter and mass ratio of the gold were also the same as those of the gold interconnect used in the healing property evaluation (50 nm in diameter and  $6\text{--}7 \times 10^{-3}$  wt%). Regarding the voltage and current applied to the device, to consume electric power for both light emission and self-healing without switching electric power sources, a resistor of 4.6 k $\Omega$  was connected to the device, and voltage

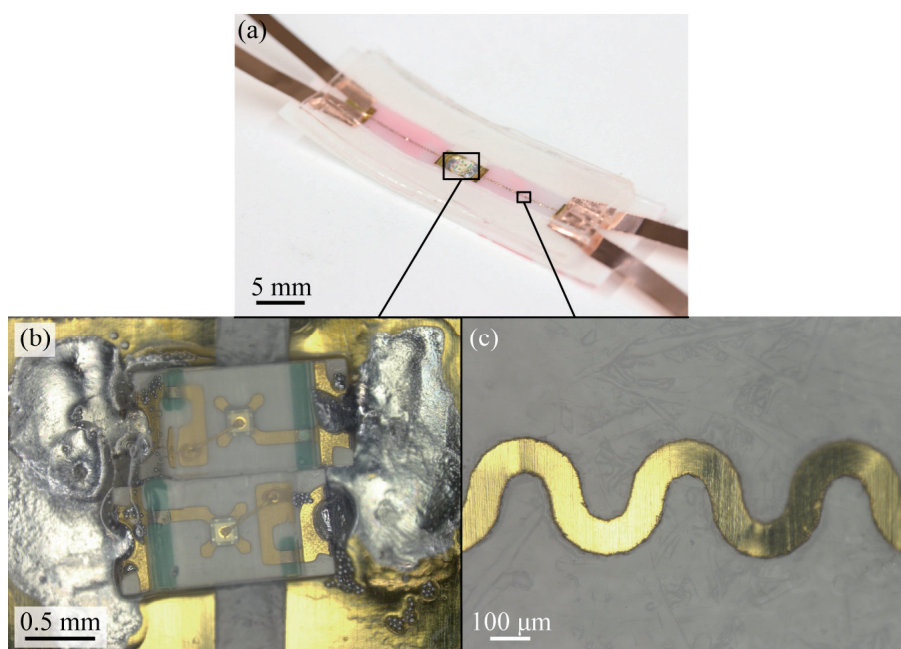


Figure 4.10 Optical images of fabricated flexible device, which is composed of self-healing gold interconnects and surface-mounted LED chips. (a) Optical image of flexible device. (b) Enlarged view of LED chips soldered on contact pads. (c) Enlarged view of wave-shaped gold interconnect on AF substrate.

(28  $V_{\text{rms}}$  and 100 kHz) was applied to the device and the resistor. In this circuit, 2.7  $V_{\text{rms}}$  and 4  $\text{mA}_{\text{rms}}$  were applied to the device when interconnects in the device were not broken, and 25  $V_{\text{rms}}$  and 2  $\text{mA}_{\text{rms}}$  were applied to the device when one of the interconnects was broken because of the increase in impedance in the interconnect; hence, the interconnect in the device can be healed without switching electric power sources. On the other hand, the electric power is also consumed by the resistor.

### 4.3.2 Fabrication

The designed devices were fabricated as illustrated in Figure 4.9. The fabrication process was essentially the same as that of the self-healing gold interconnect used in the healing property evaluation. First, 10- $\mu\text{m}$ -thick rolled gold foil (AU-173175, Nilaco) was laminated to an adhesive sheet (Figure 4.9a), and the gold foil was patterned to wave-shaped interconnects and contact pads by laser cutting (Figure 4.9b). Second, the unnecessary gold foil was peeled off by tweezers, as shown in Figure 4.9c, and the patterned gold foil was transferred to a 0.6-mm-thick acrylic form adhesive tape (Y-4930, 3M) as a substrate layer

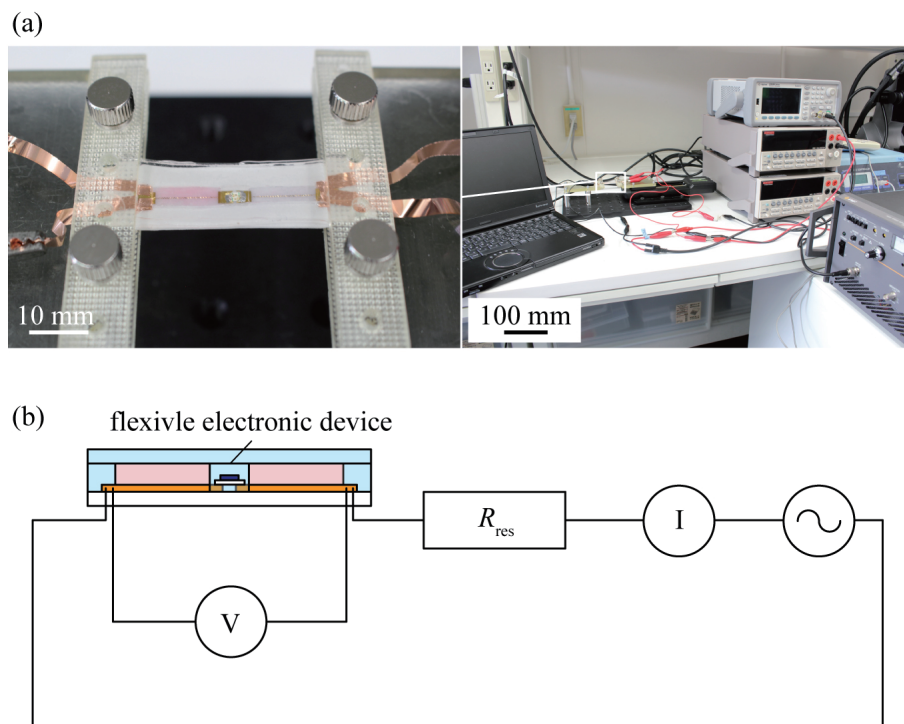


Figure 4.11 Optical images and schematic of measurement setup. (a) Optical image of measurement setup. (b) Schematic of measurement setup.

(Figure 4.9d). Then, surface-mounted LED chips (SMLE12BC7TT86, Rohm) were soldered by applying solder paste on the contact pads (Figure 4.9e). In addition, electrical wirings for electrical contact to a measurement system were laminated on the contact pads. A 1.0-mm-thick acrylic form tape (Y-4910J, 3M) patterned to a flame layer shape was laminated as shown in Figure 4.9f. Then, gold nanoparticles in a citrate-buffered aqueous medium (Au colloid solution-SC 50 nm, Tanaka Kikinzoku Kogyo) were dropped into the flame layer (Figure 4.9g). Finally, a 0.5-mm-thick acrylic form tape (Y-4905J, 3M) was laminated on the flame layer as a cover layer, as shown in Figure 4.9h. Figure 4.10 illustrates optical images of the fabricated flexible device, which was composed of wave-shaped gold interconnects with a self-healing ability and surface-mounted LED chips. In the device, only the wave-shaped gold interconnect was covered with the gold nanoparticle dispersion as designed.



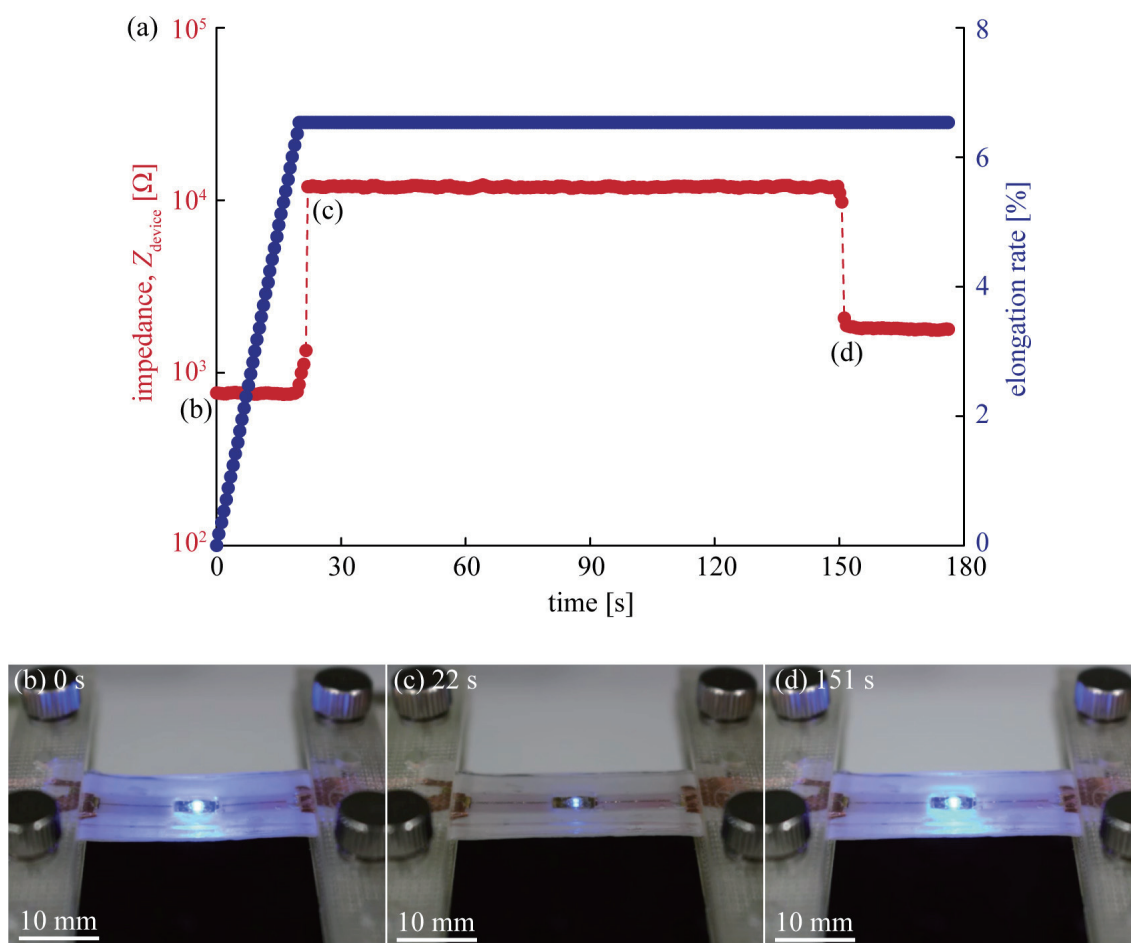


Figure 4.12 (a) Time variation of impedance of device,  $Z_{\text{device}}$  and elongation of stretchable device with self-healing ability. (b), (c), (d) Optical images of device at 0 s (beginning of measurement), 22 s (breaking of gold interconnect), and 151 s (healing of broken point of interconnect), respectively.

### 4.3.3 Measurement Setup

Figure 4.11 shows the measurement setup used to demonstrate the effectiveness of a flexible device with a self-healing gold interconnect. The measurement setup was essentially the same as that used in the healing property evaluation. A fabricated device was mounted on electrical movable stages (SGSP20-85, Sigma Koki), and stretching deformation was gradually induced in the device with applied voltage. The stages were connected to a stage controller (SOHT-204MS, Sigma Koki) to adjust and obtain the value of

the displacement,  $d$ , of the stage. A resistor (4.6 k $\Omega$  in resistance) was connected to the device in series to control the flow of current after nanoparticles bridged the broken part. An AC voltage of 28 V<sub>rms</sub> and 100 kHz was applied to the device and the resistor. The voltage applied to the flexible device,  $V_{\text{device}}$ , and the current,  $I$ , were measured with digital multimeters (2000, Keithley Instruments). The stage controller and the digital multimeters were connected to a laptop PC with GPIB cables, and a measurement software was used to obtain the values of  $d$ ,  $V_{\text{device}}$ , and  $I$  at regular intervals of approximately 0.5 ms. The value of  $d$  was also controlled by the software, and the change rate of  $d$  was 100  $\mu\text{m/s}$ . The elongation of the device was calculated by dividing  $d$  with the initial distance between the stages. The impedance of the device,  $Z_{\text{device}}$ , was calculated by  $V_{\text{device}}/I$ . When one of the gold interconnects in the device was broken and  $Z_{\text{device}}$  increased sharply, the stage stopped moving.

#### 4.3.4 Results and Discussion

Figure 4.12 shows the time variation of  $Z_{\text{device}}$  and the elongation rate of a flexible device. At the beginning of the measurement, the LED chips were emitting light, as shown in Figure 4.5a, and  $Z_{\text{device}}$  was almost stable at 0.76 k $\Omega$ . When the elongation rate increased to 6.5%,  $Z_{\text{device}}$  increased sharply from 0.76 k $\Omega$  to 12 k $\Omega$ , and the LED chips were turned off. This indicates that one of the self-healing gold interconnects in the device was broken. At 151 s,  $Z_{\text{device}}$  decreased sharply from 13 k $\Omega$  to 1.8 k $\Omega$ , and the LED chips started emitting light again. This indicates that the broken gold interconnect was electrically healed with gold nanoparticle chains formed at the broken point. Hence, this demonstrates the applicability of the self-healing metal interconnects using the dielectrophoresis of metal nanoparticles to flexible devices.

## 4.4 Summary

---

To demonstrate the applicability of self-healing metal interconnects using the dielectrophoresis of metal nanoparticles to flexible devices, a flexible device composed of self-healing metal interconnects and surface-mounted LED chips was developed. First, to verify the self-healing of a metal interconnect broken by stretching deformation and to evaluate the healing property under cyclic stretching deformation, a self-healing metal interconnect was fabricated, and the changes in the impedance of the interconnect under stretching deformation were measured. In this study, gold, AF, and gold nanoparticle dispersion were used as the metal interconnect, elastomer, and metal nanoparticle dispersion, respectively. As for the design of the self-healing gold interconnect, the elongation stiffness ratio of the gold interconnect and the substrate

layer of AF was 1.9; hence, the crack configuration was of the single-crack growth type. Regarding the applied voltage and current, a voltage of 19 to 22 V<sub>rms</sub> was applied to the interconnect when it was broken, and the current just when nanoparticles bridged the crack was 3 to 4 mA<sub>rms</sub> in order to stably form a nanoparticle chain in the crack. A fabricated self-healing gold interconnect was mounted on electrical movable stages, and cyclic stretching deformation was applied to the interconnect while measuring the impedance of the interconnect,  $Z_{\text{inter}}$ . As a result, in the first cycle of stretching deformation,  $Z_{\text{inter}}$  increased sharply from 0.58  $\Omega$  to 13 k $\Omega$  by breaking when the elongation rate was 7.6%. Fifty-seven seconds from the time of breaking,  $Z_{\text{inter}}$  decreased sharply from 13 k $\Omega$  to 1.1 k $\Omega$  by a self-healing. This verifies that a gold interconnect broken by stretching deformation can be healed with its self-healing ability using the dielectrophoresis of gold nanoparticles. Regarding the evaluation of the healing property under cyclic stretching deformation, the results obtained by the evaluation were as follows. The breaking elongation in the second to fifth cycles was lower than the breaking elongation in the first cycle, and the impedance after healing in the second to fifth cycles was higher than the impedance in the first cycle. As for the healing time, each value in the second to fifth cycle was randomly higher or lower than values in the first cycle. Second, to demonstrate the applicability of the self-healing metal interconnect to flexible devices, a flexible device composed of self-healing gold interconnects and surface-mounted LED chips was developed. As for the design of the device, the elongation stiffness ratio of the gold interconnect and the substrate layer of AF was 1.9 to form a single crack in one of the interconnects of the device. Regarding voltage and current, to consume electric power for both light emission and self-healing without switching electric power sources, a designed electric circuit was connected to the device. This circuit applied 2.7 V<sub>rms</sub> and 4 mA<sub>rms</sub> (when interconnects in the device were not broken) or 25 V<sub>rms</sub> and 2 mA<sub>rms</sub> (when one of the interconnects was broken) to the device. A fabricated device was mounted on movable stages, and stretching deformation was gradually induced in the device with applied voltage. As a result, the LEDs emitted light until the elongation rate increased to 6.5%. Then, the LEDs were turned off owing to the breaking of the interconnect. After 130 s from the time of breaking, the LEDs emitted light again by self-healing of the broken interconnect. This demonstrates the applicability of the self-healing metal interconnect using the dielectrophoresis of metal nanoparticles to flexible devices.

# Chapter 5 Conclusion

## 5.1 Overall Summary

---

The electrical and mechanical design principles of the self-healing metal interconnect using the dielectrophoresis of metal nanoparticles were identified, and flexible devices using the self-healing metal interconnect were developed based on the design principles. In this research, a complementary approach was considered: (i) Understanding the conditions required to form a nanoparticle chain so as to form a nanoparticle chain in a larger crack (which is to understand the electrical design principle, Chapter 2). (ii) Understanding the factor determining the crack configurations of a metal interconnect to control the number of cracks and crack width. Then, by combining the formation of a nanoparticle chain in the larger crack and controlling the crack configurations to a single larger crack, the self-healing metal interconnect was applied to flexible devices (Chapter 4).

In Chapter 2, in order to understand the electrical design principle of the self-healing metal interconnect, conditions for nanoparticle chain formation in a large crack of broken metal interconnect that is several tens of micrometers wide was studied; both theoretical analysis and experiments were conducted. In this research, it was considered that the formation process of the nanoparticle chain consists of trapping

and bridging processes, and each process was theoretically analyzed. Regarding the trapping process, the forces acting on a nanoparticle were analyzed; it was considered that the nanoparticles get trapped and adhere on the large crack when a certain voltage or more is applied to the broken interconnect. With regard to the bridging process, the physical phenomenon during the process was analyzed, and it was observed that Joule heating that occurs in the nanoparticle chain owing to the current breaks the nanoparticle chain when the nanoparticle chain bridges the large crack. Hence, it was assumed that a nanoparticle chain can be formed in a crack several tens of micrometers wide only when a voltage higher than a certain value and with current lower than a certain value is applied. In the experiment section, observations and measurements were conducted to verify the result obtained in the theoretical analysis section. First, certain voltages with changing current were applied to a 10- $\mu\text{m}$ -wide crack to confirm that a nanoparticle chain is formed in a large crack when a high voltage with low current is applied. As a result, in the case of the 150-nm-diameter gold nanoparticles in a citrate-buffered aqueous medium, a nanoparticle chain formation was observed in a crack only when 6.1  $V_{\text{rms}}$  or more with 15  $\text{mA}_{\text{rms}}$  or less was applied. The process of nanoparticle chain formation was directly observed with high-magnification and high-speed microscopy for the clarification of the behavior of nanoparticle chain formation. As a result, when a low voltage was applied, the nanoparticles were not trapped in the crack. On the other hand, when a high voltage with high current was applied, the repeated growth and breakage of a nanoparticle chain in the crack was observed. When a high voltage with low current was applied, the rapid growth of a nanoparticle chain to bridge the crack was observed in approximately 4 ms. Next, the maximum allowable current,  $I_{\text{max}}$ , and the resistance of nanoparticle chain,  $R_{\text{chain}}$ , was measured with increasing current applied to the nanoparticle chain. The value of  $I_{\text{max}}$  decreased as the crack width increased, and in the case of an citrate-buffered aqueous dispersion of 150-nm-diameter gold nanoparticles, it was approximately 11 mA for crack width in the range of 15  $\mu\text{m}$  to 30  $\mu\text{m}$ . Regarding  $R_{\text{chain}}$ , the value increased almost linearly as the crack width increased, and the value at 1 mA and  $I_{\text{max}}$  ranged from 23 to 94  $\Omega$  and 10 to 65  $\Omega$ , respectively, when the crack width ranged from 5 to 30  $\mu\text{m}$ . Finally, forming time,  $t_{\text{form}}$ , was measured with the deferent voltage applied to the interconnect. As a result, the values of  $t_{\text{form}}$  for 10  $V_{\text{rms}}$  and 12  $V_{\text{rms}}$  ranged from 15 to 47 s and 7 to 21 s when the crack width ranged from 5 to 20  $\mu\text{m}$ . Hence, in this chapter, it was concluded that a nanoparticle chain can be formed in a large crack, such as one that is several tens of micrometers wide, when a high voltage with low current is applied.

. In Chapter 3, in order to understand mechanical design principle of self-healing metal interconnect, factors determining crack configurations of a stretched metal interconnect were studied by

both theoretical analysis and experiments. In the theoretical analysis section, theoretical calculations were conducted. The calculation results indicated that crack configurations are determined by the elongation stiffness ratio of a metal interconnect and an elastomer, and they are classified into multiple-crack growth and single-crack growth type. It was established that a multiple-crack growth type is often observed when the elongation stiffness ratio is lower than approximately 0.1, while a single-crack growth type is often observed when the elongation stiffness ratio is higher than approximately unity, with reference to previous studies. In the experiment section, first, to verify the results of theoretical calculation, straight-shaped interconnects with  $t_{\text{inter}} = 0.04\text{--}1.17\ \mu\text{m}$  (0.03–0.78 is the elongation stiffness ratio) were fabricated, and then cracks caused by stretching deformation were observed. As a result, the multiple-crack growth type was observed, when  $t_{\text{inter}} = 0.04\ \mu\text{m}$ , and the crack configuration gradually changed to a single crack, as  $t_{\text{inter}}$  increased. Hence, this corresponds to the result of the theoretical analysis. Second, wave-shaped metal interconnects with single-crack growth type were fabricated, and the breaking elongation and the width of the cased crack were measured. In this research, the thickness of metal interconnect and thickness of elastomer were especially focused on; hence, the wave-shaped metal interconnect with different thicknesses of the metal interconnect and the elastomer were used for the measurement. As a result, the breaking elongation was several tens of percentages, and the crack width was several tens of micrometers. For the sample that used the copper interconnect with different thicknesses, the breaking elongation increased significantly as the thickness of the copper interconnect increased. For the sample with a different thickness of the elastomer, the breaking elongation decreased as the thickness of the elastomer increased. In addition, the crack width almost linearly increased as the breaking elongation increased. Therefore, in this chapter, it is concluded that the crack configuration can be controlled to the single-crack growth type by designing the elongation stiffness ratio of the metal interconnect. Furthermore, the crack width decreases as the breaking elongation increased.

In Chapter 4, based on the result of Chapters 2 and 3, the flexible device using self-healing metal interconnect was developed. To verify the self-healing of a metal interconnect broken by stretching deformation and to evaluate the healing property under cyclic stretching deformation, a self-healing metal interconnect was fabricated, and impedance changes of the interconnect under stretching deformation were measured. Regarding the mechanical design of the self-healing gold interconnect, to control the crack configuration to the single crack growth type, the elongation stiffness ratio of the gold interconnect and the substrate layer of acrylic foam (AF) was 1.9, based on Chapter 3. Regarding the applied voltage and current (electrical design), to stably form a nanoparticle chain in the crack, a voltage ranging from 19 to

22  $V_{\text{rms}}$  was applied to the interconnect when it was broken, and the current flowing just when nanoparticles bridged the crack was 3 to 4  $\text{mA}_{\text{rms}}$ , based on Chapter 2. A fabricated self-healing gold interconnect was mounted on electrical movable stages, and cyclic stretching deformation was applied to the interconnect while measuring the impedance of the interconnect,  $Z_{\text{inter}}$ . As a result, after 57 s from the breaking of the stretched interconnect,  $Z_{\text{inter}}$  sharply decreased from 13  $\text{k}\Omega$  to 1.1  $\text{k}\Omega$ . This verifies that a broken gold interconnect by stretching deformation was healed with the self-healing ability. For evaluating the healing property under cyclic stretching deformation, the results obtained by the evaluation were as follows: The breaking elongation in the second to fifth cycles was lower than the breaking elongation in the first cycle, and the impedance after healing in the second to fifth cycles was higher than the impedance in the first cycle. As for the healing time, each value in the second to fifth cycle had randomly higher and lower values than the first cycle. Second, to demonstrate the applicability of the self-healing metal interconnect to flexible devices, a flexible device composed of self-healing gold interconnects and surface-mounted light emitting diode (LED) chips was developed. For the electrical and mechanical design of the self-healing metal interconnect, the voltage and the current applied to the interconnect were almost same as that used for the evaluation of the self-healing property (1.9 of the elongation stiffness ratio, and 2.7  $V_{\text{rms}}$  with 4  $\text{mA}_{\text{rms}}$  (when interconnects in the device were not broken) or 25  $V_{\text{rms}}$  with 2  $\text{mA}_{\text{rms}}$  (when one of the interconnects was broken)). Further, the device was designed to consume electric power for both light emitting and self-healing without switching an electric power source. A fabricated device was mounted on movable stages, and stretching deformation was gradually applied to the device with applied voltage. As a result, the LEDs emitted light until the elongation rate increased to 6.5%. Then, the LEDs turned off by breaking of the interconnect. After 130 s from the breaking, the LEDs emitted light again by self-healing of the broken interconnect. Hence, the applicability of the self-healing metal interconnect using the dielectrophoresis of metal nanoparticles to flexible devices was demonstrated.

## 5.2 Future Prospect

---

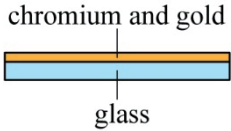

In this research, the main target for the application of the self-healing metal interconnect using dielectrophoresis of metal nanoparticle is flexible devices. However, it is considered that the self-healing ability is useful for not only flexible device but also for electrical wirings, which are difficult to repair; for example, electric circuits in satellites and submarines, and electrical cables embedded in the ground. In this case, the long-term stability of the sealing for metal nanoparticles dispersion is one of the important

factors. Currently, elastomers and an aqueous solution are used for the sealing structure and metal nanoparticle dispersion in the device, respectively. In general, the elastomers have high water vapor permeability and the aqueous solution is easy to evaporate; hence, it remains difficult to seal the metal nanoparticles in the device in a stable manner. The potential solutions to the above-mentioned problem are as follows; coating the surface of the elastomer with a thin film, which have low vapor permeability, such as parylene, and using non-volatile materials, such as silicone oils and ionic liquid, for the medium of the metal nanoparticle dispersion. These solutions enable the application of the self-healing ability using the dielectrophoresis of metal nanoparticles, to various devices.



## Appendix A Fabrication Process


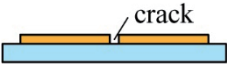
### Cracked Gold Interconnect on Glass Substrate (Chapter 2)

cross sectional view	process	condition	
 <p>chromium and gold glass</p>	deposition of chromium layer and gold layer	chromium layer	electron-beam evaporation system (EBX-6D) rate 1 0.1 nm/sec (0.003 $\mu\text{m}$ ) rate 2 0.1 nm/sec (0.007 $\mu\text{m}$ ) rate 3 0.1 nm/sec (0.01 $\mu\text{m}$ )
		gold layer	electron-beam evaporation system (EBX-6D) rate 1 0.1 nm/sec (0.01 $\mu\text{m}$ ) rate 2 0.3 nm/sec (0.49 $\mu\text{m}$ ) rate 3 0.1 nm/sec (0.5 $\mu\text{m}$ )
 <p>photoresist</p>	patterning photoresist	spin coating	photoresist (OFPR800 20cp) 500 rpm 5 sec 3000 rpm 30 sec
		bake	hot plate (RSH-1DN) 100°C 1 min
		exposure	mask aligner (MJB 3) 9 mJ/cm <sup>2</sup> 13 sec

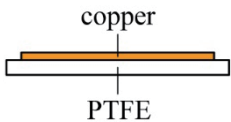

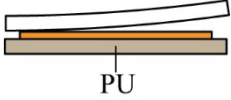

---

*Appendix A Fabrication Process*

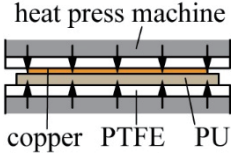

---

		development	developer (TMAH 2.83%) soak 1 min deionized water 1st rinse 1 min 2nd rinse 1 min spin dry 1 min
	patterning chromium layer and gold layer	gold etching	etchant (AURUM-302) soak 5 min deionized water 1st rinse 1 min 2nd rinse 1 min spin dry 1 min
		chromium etching	etchant (mixed acid chromium etchant) soak 10 sec deionized water 1st rinse 1 min 2nd rinse 1 min spin dry 1 min
	removing photoresist	exposure	mask aligner (MJB 3) 9 mJ/cm <sup>2</sup> 1 min
		development	developer (TMAH 2.83%) soak 1 min Deionized water 1st rinse 1 min 2nd rinse 1 min spin dry 1 min

**Straight-Shaped Copper Interconnect Embedded in PU (Chapter 3)**

cross sectional view	process	condition
 <p>copper PTFE</p>	deposition of copper layer	thermal evaporation system (SVC-700TMSG/7PS80) rate 0.2 nm/sec (0.04 $\mu\text{m}$ , 0.10 $\mu\text{m}$ , 0.18 $\mu\text{m}$ , 0.53 $\mu\text{m}$ , and 1.17 $\mu\text{m}$ )
 <p>cutter</p>	cutting	
 <p>PU</p>	transferring copper layer to PU tape	PU tape (Tegaderm 9534HP)
	laminating PU tape	PU tape (Tegaderm 9534HP)

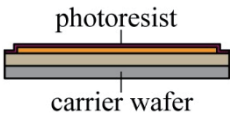


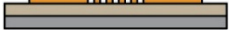
**Wave-Shaped Copper Interconnect Embedded in PU (Chapter 3)**

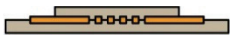
cross sectional view	process	condition
 <p>heat press machine copper PTFE PU</p>	laminating copper foil on PU sheet	<p>hot plate (DP-1S) 100°C 3 min</p> <p>rolled copper foil (CU-113091 (2 <math>\mu\text{m}</math>), CU-113121 (4 <math>\mu\text{m}</math>), CU-113141 (6 <math>\mu\text{m}</math>), CU-113151 (8 <math>\mu\text{m}</math>), CU-113173 (10 <math>\mu\text{m}</math>))</p> <p>PU sheet (Platilon 4201 (0.05 mm))</p>

---

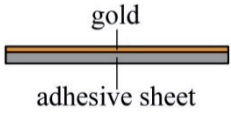
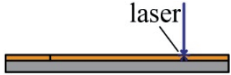

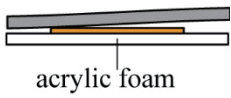
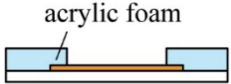
*Appendix A Fabrication Process*


---

		pressing	heat press machine (IMC-180C) 170 °C 0.4 MPa 3 min
 <p>photoresist carrier wafer</p>		spin coating	photoresist (OFPR800 20cp) 500 rpm 5 sec 3000 rpm 30 sec
		bake	hot plate (RSH-1DN) 100°C 1 min
	patterning photoresist	exposure	mask aligner (MJB 3) 9 mJ/cm <sup>2</sup> 13 sec
		development	developer (TMAH 2.83%) soak 1 min deionized water 1st rinse 1 min 2nd rinse 1 min spin dry 1 min
	patterning copper layer	etchant (H-1000A) soak 10 sec deionized water 1st rinse 1 min 2nd rinse 1 min spin dry 1 min	
	removing photoresist	exposure	mask aligner (MJB 3) 9 mJ/cm <sup>2</sup> 13 sec

		development	developer (TMAH 2.83%) soak 1 min Deionized water 1st rinse 1 min 2nd rinse 1 min spin dry 1 min
	laminating PU tape	PU tape (Tegaderm 9534HP)	



#### Self-Healing Gold Interconnect (Chapter 4)

cross sectional view	process	condition
	laminating gold foil on adhesive sheet	gold foil (AU-173174 (10 μm)) adhesive sheet (CR09308)
	laser cutting gold foil	laser-cutting machine (OLMUV-355-5A-K) speed 50 mm/sec power 20% frequency 30 kHz the number of cutting 1 duty cycle 65%
	removing unnecessary area of gold foil	
	transferring gold layer to substrate layer of AF	AF adhesive tape (Y-4930 (0.6 mm))
	laminating flame layer of AF	AF adhesive tape (Y-4910J (1 mm))


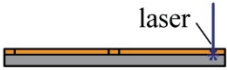

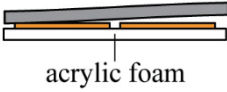
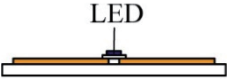

---

*Appendix A Fabrication Process*


---

 <p>gold nanoparticle dispersion</p>	dropping gold nanoparticle dispersion	gold nanoparticles in citrate-buffered aqueous dispersion (Au colloid solution-SC 50 nm)
	laminating top layer of AF	AF adhesive tape (Y-4905J (0.5 mm))



**Flexible device with Self-Healing Ability (Chapter 4)**

cross sectional view	process	condition
 <p>gold adhesive sheet</p>	laminating gold foil on adhesive sheet	gold foil (AU-173174 (10 μm)) adhesive sheet (CR09308)
 <p>laser</p>	laser cutting gold foil	laser-cutting machine (OLMUV-355-5A-K) speed 50 mm/sec power 20% frequency 30 kHz the number of cutting 1 duty cycle 65%
	removing unnecessary area of gold foil	
 <p>acrylic foam</p>	transferring gold layer to substrate layer of AF	AF adhesive tape (Y-4930 (0.6 mm))
 <p>LED</p>	soldering surface-mounted LED chips	surface mount LED chip (SMLE12BC7TT86) solder paste (SMX-H05) 250°C with soldering iron
 <p>acrylic foam</p>	laminating flame layer of AF	AF adhesive tape (Y-4910J (1 mm))

---

*Appendix A Fabrication Process*

---

<p>gold nanoparticle dispersion</p> 	<p>dropping gold nanoparticle dispersion</p>	<p>gold nanoparticles in citrate-buffered aqueous dispersion (Au colloid solution-SC 50 nm)</p>
	<p>laminating top layer of AF</p>	<p>AF adhesive tape (Y-4905J (0.5 mm))</p>

## Appendix B Materials and Equipment

### Chemical Products

	<b>product number</b>	<b>manufacture</b>
photoresist	OFPR800-20cp	Tokyo Ohka Kogyo
developer	TMAH 2.83%	Tama Chemicals
gold etchant	AURUM-302 AURUM-304	Kanto Chemical
chromium etchant	mixed acid chromium etchant	Kanto Chemical
copper etchant	H-1000A	Sunhayato
gold nanoparticle dispersion	Au colloid solution-SC 50 nm Au colloid solution-SC 150 nm	Tanaka Kikinzoku Kogyo



**Metal Materials**

	<b>product number</b>	<b>manufacture</b>
rolled copper foil	CU-113091 (2 $\mu\text{m}$ ) CU-113121 (4 $\mu\text{m}$ ) CU-113141 (6 $\mu\text{m}$ ) CU-113151 (8 $\mu\text{m}$ ) CU-113173 (10 $\mu\text{m}$ )	Nilaco
rolled gold foil	AU-173174 (10 $\mu\text{m}$ )	Nilaco

**Elastomers**

	<b>product number</b>	<b>manufacture</b>
PU film	Platilon 4201 (0.1 mm) Platilon 4201 (0.05 mm)	Covestro AG
PU adhesive tape	Tegaderm 9534HP	3M
AF adhesive tape	Y-4930 (0.6 mm) Y-4905J (0.5 mm) Y-4910J (1 mm)	3M
PDMS	silpot 184 sylgard 184	Dow Chemical

**Other materials**

	<b>product number</b>	<b>manufacture</b>
glass substrate	CS00438 (20 mm × 20 mm) CS00434 (40 mm × 50 mm)	Matsunami Glass Industry
surface mount LED chip	SMLE12BC7TT86	Rohm
adhesive sheet	CR09308	Graphtech
solder paste	SMX-H05	Sunhayato

**Micro Machining Machines**

	<b>product number</b>	<b>manufacture</b>
electron-beam evaporation system	EBX-6D	Ulvac
spin coater	1H-D7	Mikasa
hot plate	DP-1S RSH-1DN	Iuchi As One
mask aligner	MJB 3	Karl Suss
thermal evaporation system	SVC-700TMSG/7PS80	Sanyu Electron
plasma cleaner	PDC-32G	Harrick Plasma
laser-cutting machine	OLMUV-355-5A-K	OPI

---

*Appendix B Materials and Equipment*


---

mixing and degassing machine	ARE-310	Thinky
heat press machine	IMC-180C	Imoto Machinery

**Measuring Instruments**

	<b>product number</b>	<b>manufacture</b>
digital multi meters	2000	Keitley Instruments
oscilloscope	DSO-X 2024A	Agilent
source meter	2614B	Keitley Instruments
waveform generator	33500B	Agilent
amplifier	HAS 4101	NF
FE-SEM	S-4800	Hitachi High-Technologies
microscope	VHX-2000	Keyence
high-speed microscope	VW-9000	Keyence
data logger	GL7000	Graphtec
high speed voltage unit for data logger	GL7-HSV	Graphtec

**Other Equipment**

	<b>product number</b>	<b>manufacture</b>
manual movable stage	TSD-602S	Sigma-Koki
electric movable stage	SGSP20-85	Sigma-Koki
stage controller	SOHT-204MS	Sigma-Koki

## Appendix C Embodiment Informatics

The Graduate program for Embodiment Informatics, Waseda University, provided the author with considerable support for this research. Graduate program for Embodiment Informatics is a part of the Ministry of Education, Culture, Sports, Science and Technology's work to make significance reforms to the graduate school education in Japan. This section describes the author's understanding about the Embodiment Informatics and how this research contributes the Embodiment Informatics, in order to express the author's application to the graduate program for Embodiment Informatics.

Figure C.1 illustrates the research field of the Embodiment Informatics. The Embodiment Informatics considers the interaction between the real world (not only humans but also all of living things in the world) and information technology for the benefit of the real world. The interaction described here was to obtain data from the object in the real world and to take action on these objects based on the processed data. The author considers the interaction where the objects did not feel the existence of the technology to be the best interaction. That is, the technology perfectly integrated to the life of living things in the real world as the "imperceptible technology." In particular, with regards to obtaining data, physical

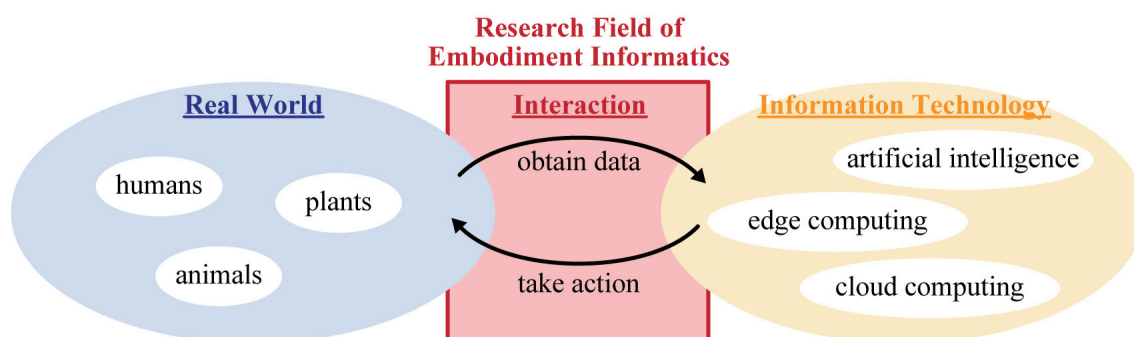


Figure C.1 Schematic illustration of the research field of Embodiment Informatics

contact between the object and sensing devices is useful to get rich data associated with the object, such as bio-information sensing using smart watch; however, data-sensing using such sensing devices without feeling of existence of the device is still difficult. The author considers that flexible devices are suitable for data-sensing as “imperceptible devices.” Hence, the author believes that this research will contribute to the Embodiment Informatics.

## References

### Flexible Devices

- [1] H. Ohmae, Y. Tomita, M. Kasahara, J. Schram, E. Smits, J. van der Brand, F. Bossuyt, J. Vanfleteren, and J. D. Baets, “Stretchable  $45 \times 80$  RGB LED display using meander wiring technology,” *SID Symposium Digest of Technical Papers*, vol. 46, issue 1, pp. 102–105, 2015.
- [2] M. Choi, B. Jang, W. Lee, S. Lee, T. W. Kim, H.-J. Lee, J.-H. Kim, and J.-H. Ahn, “Stretchable active matrix inorganic light-emitting diode display enabled by overlay-aligned roll-transfer printing,” *Advanced Functional Materials*, vol. 27, issue 11, 1606005 (10 pages), 2017.
- [3] T. Yokota, P. Zalar, M. Kaltenbrunner, H. Jinno, N. Matsuhisa, H. Kitanosako, Y. Tachibana, W. Yukita, M. Koizumi, and T. Someya, “Ultraflexible organic photonic skin,” *Science Advances*, vol. 2, no. 4, e1501856 (8 pages), 2016.
- [4] T. Sekitani, H. Nakajima, H. Maeda, T. Fukushima, T. Aida, K. Hata, and T. Someya, “Stretchable active-matrix organic light-emitting diode display using printable elastic conductors,” *Nature Materials*, vol. 8, pp. 494–499, 2009.
- [5] X. Hu, P. Krull, B. D. Graff, K. Dowling, J. A. Rogers, and W. J. Arora, “Stretchable inorganic - semiconductor electronic systems,” *Advanced Materials*, vol. 23, issue 26, pp. 2933–2936, 2011.
- [6] D. J. Lipomi, M. Vosgueritchian, B. C-K. Tee, S. L. Hellstrom, J. A. Lee, C. H. Fox, and Z. Bao, “Skin-like pressure and strain sensors based on transparent elastic films of carbon nanotubes,” *Nature Nanotechnology*, vol. 6, pp. 788–792, 2011.
- [7] J. Kim, M. Lee, H. J. Shim, R. Ghaffari, H. R. Cho, D. Son, Y. H. Jung, M. Soh, C. Choi, S. Jung, K. Chu, D. Jeon, S.-T. Lee, J. H. Kim, S. H. Choi, T. Hyeon, and D.-H. Kim, “Stretchable silicon nanoribbon electronics for skin prosthesis,” *Nature Communications*, vol. 5, 5754 (11 pages), 2014.

---

*References*

---

- [8] T. Someya, T. Sekitani, S. Iba, Y. Kato, H. Kawaguchi, and T. Sakurai, "A large-area, flexible pressure sensor matrix with organic field-effect transistors for artificial skin applications," *Proceedings of the National Academy of Sciences of the United States of America*, vol. 101, no. 27, pp. 9966–9970, 2004.
- [9] T. Yokota, Y. Inoue, Y. Terakawa, J. Reeder, M. Kaltenbrunner, T. Ware, K. Yang, K. Mabuchi, T. Murakawa, M. Sekino, W. Voit, T. Sekitani, and T. Someya, "Ultraflexible, large-area, physiological temperature sensors for multipoint measurements," *Proceedings of the National Academy of Science of the United States of America*, vol. 112, no. 47, pp. 14533–14538, 2015.
- [10] W.-P. Shih, L.-C. Tsao, C.-W. Lee, M.-Y. Cheng, C. Chang, Y.-J. Yang, and K.-C. Fan, "Flexible temperature sensor array based on a graphite-polydimethylsiloxane composite," *Sensors*, vol. 10, issue 4, pp. 3597–3610, 2010.
- [11] D. Liu and T. L. Kelly, "Perovskite solar cells with a planar heterojunction structure prepared using room-temperature solution processing techniques," *Nature Photonics*, vol. 8, pp. 133–138, 2014.
- [12] H. Jinno, K. Fukuda, X. Xu, S. Park, Y. Suzuki, M. Koizumi, T. Yokota, I. Osaka, K. Takimiya, and T. Someya, "Stretchable and waterproof elastomer-coated organic photovoltaics for washable electronic textile applications," *Nature Energy*, vol. 2, pp. 780–785, 2017.
- [13] J. You, Z. Hong, Y. (M.) Yang, Q. Chen, M. Cai, T.-B. Song, C.-C. Chen, S. Lu, Y. Liu, H. Zhou, and Y. Yang, "Low-temperature solution-processed perovskite solar cells with high efficiency and flexibility," *ACS Nano*, vol. 8, no. 2, pp. 1674–1680, 2014.
- [14] M. Kaltenbrunner, M. S. White, E. D. Głowacki, T. Sekitani, T. Someya, N. S. Sariciftci, and S. Bauer, "Ultrathin and lightweight organic solar cells with high flexibility," *Nature Communications*, vol. 3, 770 (7 pages), 2012.
- [15] P. Docampo, J. M. Ball, M. Darwich, G. E. Eperon, and H. J. Snaith, "Efficient organometal trihalide perovskite planar-heterojunction solar cells on flexible polymer substrates," *Nature Communications*, vol. 4, 2761 (6 pages), 2013.
- [16] Z. Fan, H. Razavi, J. Do, A. Moriwaki, O. Ergen, Y.-L. Chueh, P. W. Leu, J. C. Ho, T. Takahashi, L. A. Reichertz, S. Neale, K. Yu, M. Wu, J. W. Ager, and A. Javey, "Three-dimensional nanopillar-array photovoltaics on low-cost and flexible substrates," *Nature Materials*, vol. 8, 648–653, 2009.
- [17] B. Liu, J. Zhang, X. Wang, G. Chen, D. Chen, C. Zhou, and G. Shen, "Hierarchical three-dimensional ZnCo<sub>2</sub>O<sub>4</sub> nanowire arrays/carbon cloth anodes for a novel class of high-performance flexible lithium-ion batteries," *Nano Letters*, vol. 12, pp. 3005–3011, 2012.



- 
- [18] J. W. Lee, R. Xu, S. Lee, K.-I. Jang, Y. Yang, A. Banks, K. J. Yu, J. Kim, S. Xu, S. Ma, S. W. Jang, P. Won, Y. Li, B. H. Kim, J. Y. Choe, S. Huh, Y. H. Kwon, Y. Huang, U. Paik, and J. A. Rogers, "Soft, thin skin-mounted power management systems and their use in wireless thermography," *Proceedings of the National Academy of Sciences of the United States of America*, vol. 113, issue. 22, pp. 6131–6136, 2016.
- [19] M. F. El-Kady and R. B. Kaner, "Scalable fabrication of high-power graphene micro-supercapacitors for flexible and on-chip energy storage," *Nature Communications*, vol. 4, 1475 (9 pages), 2013.
- [20] S. Xu, Yihui Z., Jiung Cho, J. Lee, X. Huang, L. Jia, J. A. Fan, Y. Su, J. Su, H. Zhang, H. Cheng, B. Lu, C. Yu, C. Chuang, T. Kim, T. Song, K. Shigeta, S. Kang, C. Dagdeviren, I. Petrov, P. V. Braun, Y. Huang, U. Paik, and J. A. Rogers, "Stretchable batteries with self-similar serpentine interconnects and integrated wireless recharging systems," *Nature Communications*, vol. 4, 1543 (8 pages), 2013.
- [21] V. L. Pushparaj, M. M. Shaijumon, A. Kumar, S. Murugesan, L. Ci, R. Vajtai, R. J. Linhardt, O. Nalamasu, and P. M. Ajayan, "Flexible energy storage devices based on nanocomposite paper," *Proceedings of the National Academy of Sciences of the United States of America*, vol. 104, no. 34, 13574–13577, 2007.
- [22] Z. Weng, Y. Su, D. - W. Wang, F. Li, J. Du, and H. - M. Cheng, "Graphene–cellulose paper flexible supercapacitors," *Advanced Energy Materials*, vol. 1, issue 5, pp. 917–922, 2011.
- [23] A. Chortos, J. Liu, and Z. Bao, "Pursuing prosthetic electric skin," *Nature Materials*, vol. 15, pp. 937–950, 2016.
- [24] C. Pang, C. Lee, and K.-Y. Suh, "Recent Advances in Flexible Sensors for Wearable and Implantable Devices," *Journal of Applied Polymer Science*, vol. 130, issue 3, pp. 1429–1441, 2013.
- [25] D.-H. Kim, J. Xiao, J. Song, Y. Hung, and J. A. Rogers, "Stretchable curvilinear electronics based on inorganic materials," *Advanced Materials*, vol. 22, issue 19, pp. 2108–2124, 2010.
- [26] K. J. Yu, Z. Yan, M. Han, and J. A. Rogers, "Inorganic semiconducting materials for flexible and stretchable electronics," *Flexible electronics*, vol. 1, 4 (14 pages), 2017.
- [27] M. D. Dickey, "Stretchable and soft electronics using liquid metals," *Advanced Materials*, vol. 29, issue 27, 1606425 (19 pages), 2017.
- [28] M. L. Hammock, A. Chortos, B. C.-K. Tee, J. B.-H. Tok, and Z. Bao, "25th anniversary article: the evolution of electronic skin (E-Skin): a brief history, design considerations, and recent progress," *Advanced Materials*, vol. 25, issue 42, pp. 5997–6038, 2013.

---

*References*

---

- [29] M. Segev-Bar and H. Haick, "Flexible Sensors Based on Nanoparticles," *ACS Nano*, vol. 7, no. 10, pp. 8366–8378, 2013.
- [30] S. Park, M. Vosguerichian, and Z. Bao, "A review of fabrication and applications of carbon nanotube film-based flexible electronics," *Nanoscale*, issue 5, pp. 1727–1752, 2013.
- [31] S. R. Forrest, "The path to ubiquitous and low-cost organic electronic appliances on plastic," *Nature*, vol. 428, pp. 911–918, 2004.
- [32] T. Chang, Y. Zhang, W.-Y. Lai, and W. Hung, "Stretchable Thin - Film Electrodes for Flexible Electronics with High Deformability and Stretchability," *Advanced Materials*, vol. 27, issue 22, pp. 3349–3376, 2015.
- [33] W. Liu, M.-S. Song, B. Kong, and Y. Cui, "Flexible and Stretchable Energy Storage: Recent Advances and Future Perspectives," *Advanced Materials*, vol. 29, issue 1, 1603436 (34 pages), 2016.
- [34] Y. Sun and J. A. Rogers, "Inorganic Semiconductors for Flexible Electronics," *Advanced Materials*, vol. 19, issue 15, pp. 1897–1916, 2007.
- [35] Y. Zang, F. Zhang, C. Di, and D. Zhu, "Advances of flexible pressure sensors toward artificial intelligence and health care applications," *Material Horizons*, issue 2, pp. 140–156, 2015.
- [36] A. Koh, D. Kang, Y. Xue, S. Lee, R. M. Pielak, J. Kim, T. Hwang, S. Min, A. Banks, P. Bastien, M. C. Manco, L. Wang, K. R. Ammann, K.-I. Jang, P. Won, S. Han, R. Ghaffari, U. Paik, M. J. Slepian, G. Balooch, Y. Huang, and J. A. Rogers, "A soft, wearable microfluidic device for the capture, storage, and colorimetric sensing of sweat," *Science Translational Medicine*, vol. 8, issue 336, 366ra165 (13 pages), 2016.
- [37] A. Miyamoto, S. Lee, N. F. Cooray, S. Lee, M. Mori, N. Matsuhisa, H. Jin, L. Yoda, T. Yokota, A. Itoh, M. Sekino, H. Kawasaki, T. Ebihara, M. Amagai, and T. Someya, "Inflammation-free, gas-permeable, lightweight, stretchable on-skin electronics with nanomeshes," *Nature Nanotechnology*, vol. 12, 907–913, 2017.
- [38] D.-H. Kim, Nanshu Lu, R. Ma, Y.-S. Kim, R.-H. Kim, S. Wang, J. Wu, S. M. Won, H. Tao, A. Islam, K. J. Yu, T. Kim, R. Chowdhury, M. Ying, L. Xu, M. Li, H.-J. Chung, H. Keum, M. McCormick, P. L., Y.-W. Zhang, F. G. Omenetto, Y. Huang, T. Coleman, and J. A. Rogers, "Epidermal Electronics," *Science*, vol. 333, issue 6044, pp. 838–843, 2011.
- [39] J. A. Fan, W.-H. Yeo, Y. Su, Y. Hattori, W. Lee, S.-Y. Jung, Y. Zhang, Z. Liu, H. Cheng, L. Falgout, M. Bajema, T. Coleman, D. Gregoire, R. J. Larsen, Y. Huang, and J. A. Rogers, "Fractal design concepts for stretchable electronics," *Nature Communications*, vol. 5, 3266 (8 pages), 2014.

- 
- [40] J. Kim, G. A. Salvatore, H. Araki, A. M. Chiarelli, Z. Xie, A. Banks, X. Sheng, Y. Liu, J. W. Lee, K.-I. Jang, S. Y. Heo, K. Cho, H. Luo, B. Zimmerman, J. Kim, L. Yan, X. Feng, S. Xu, M. Fabiani, G. Gratton, Y. Huang, U. Paik, and J. A. Rogers, “Battery-free, stretchable optoelectronic systems for wireless optical characterization of the skin,” *Science Advances*, vol. 2, no. 8, e1600418 (10 pages), 2016.
- [41] L. Gao, Y. Zhang, V. Malyarchuk, L. Jia, K.-I. Jang, R. C. Webb, H. Fu, Y. Shi, G. Zhou, L. Shi, D. Shah, X. Huang, B. Xu, C. Yu, Y. Huang, and J. A. Rogers, “Epidermal photonic devices for quantitative imaging of temperature and thermal transport characteristics of the skin,” *Nature Communications*, vol. 5, 4938 (10 pages), 2014.
- [42] S. Yao and Y. Zhu, “Wearable multifunctional sensors using printed stretchable conductors made of silver nanowires,” *Nanoscale*, vol. 6, issue 4, pp. 2345–2352, 2014.
- [43] Y. Chen, B. Lu, Y. Chen, and X. Feng, “Breathable and stretchable temperature sensors inspired by skin,” *Scientific Reports*, vol. 5, 11505 (11 pages), 2015.
- [44] Z. Li and Z. L. Wang, “Air/liquid-pressure and heartbeat-driven flexible fiber nanogenerators as a micro/nano-power source or diagnostic sensor,” *Advanced Materials*, vol. 23, issue 1, pp. 84–89, 2011.

#### **Ultra-Thin Devices with Out-of-Plane Wrinkle Structure**

- [45] K. Fukuda, Y. Takeda, Y. Yoshimura, R. Shiwaku, L. T. Tran, T. Sekine, M. Mizukami, D. Kumaki, and S. Tokito, “Fully-printed high-performance organic thin-film transistors and circuitry on one-micron-thick polymer films,” *Nature Communications*, vol. 5, 4147 (8 pages), 2014.
- [46] M. Drack, I. Graz, T. Sekitani, T. Someya, M. Kaltenbrunner, and S. Bauer, “An imperceptible plastic electronic wrap,” *Advanced Materials*, vol. 27, issue 1, pp 34–40, 2014.
- [47] M. Kaltenbrunner, T. Sekitani, J. Reeder, T. Yokota, K. Kuribara, T. Tokuhara, M. Drack, R. Schwodiauer, I. Graz, S. B-Gogonea, S. Bauer, and T. Someya, “An ultra-lightweight design for imperceptible plastic electronics,” *Nature*, vol. 499, pp. 458–463, 2013.
- [48] M. S. White, M. Kaltenbrunner, E. D. Głowacki, K. Gutnichenko, G. Kettlgruber, I. Graz, S. Aazou, C. Ulbricht, D. A. M. Egbe, M. C. Miron, Z. Major, M. C. Scharber, T. Sekitani, T. Someya, S. Bauer, and N. S. Sariciftci, “Ultrathin, highly flexible, and stretch-compatible PLEDs”, *Nature Photonics*, vol. 7, pp. 811–816, 2013.

**Elastic Conductors as Conductive Interconnects**

- [49] N. Matsuhisa, D. Inoue, P. Zalar, H. Jin, Y. Matsuba, A. Itoh, T. Yokota, D. Hashizume, and T. Someya, "Printable elastic conductors by in situ formation of silver nanoparticles from silver flakes," *Nature Materials*, vol. 16, pp. 824–840, 2017.
- [50] N. Matsuhisa, M. Kaltenbrunner, T. Yokota, H. Jinno, K. Kuribara, T. Sekitani, and T. Someya, "Printable elastic conductors with a high conductivity for electronic textile applications," *Nature Communications*, vol. 21, 7416 (11 pages), 2015.
- [51] T. Sekitani, Y. Noguchi, K. Hata, T. Fukushima, T. Aida, and T. Someya, "A rubberlike stretchable active matrix using elastic conductors," *Science*, vol. 321, issue 5895, pp. 1468–1472, 2008.

**Wave-Shaped Metal Interconnects**

- [52] D-H. Kim, Z. Liu, Y-S. Kim, J. Wu, J. Song, H-S. Kim, Y. Huang, K. Hwang, Y. Zhang, and J. A. Rogers, "Optimized structural designs for stretchable silicon integrated circuits," *Small*, vol. 5, issue 24, pp. 2841–2847, 2009.
- [53] D. S. Gray, J. Tien, and C. S. Chen, "High-conductivity elastomeric electronics," *Advanced Materials*, vol. 16, no. 5, pp. 393–397, 2004.
- [54] F. Bossuyt, T. Vervust, and J. Vanfleteren, "Stretchable Electronics Technology for Large Area Applications: Fabrication and Mechanical Characterization," *IEEE Transactions on Components, Packaging and Manufacturing Technology*, vol. 3, issue 2, pp. 229–235, 2013.
- [55] J. Jones, S. P. Lacour, and S. Wagner, "Stretchable wavy metal interconnect," *Journal of Vacuum Science and Technology A*, vol. 22, no. 4, pp. 1723–1725, 2004.
- [56] S. Xu, Y. Zhang, L. Jia, K. E. Mathewson, K-I. Jang, J. Kim, H. Fu, X. Huang, P. Chava, R. Wang, S. Bhole, L. Wang, Y. J. Na, Y. Guan, M. Flavin, Z. Han, Y. Huang, and J. A. Rogers, "Soft Microfluidic Assemblies of Sensors, Circuits, and Radios for the Skin," *Science*, vol. 344, Issue 6179, pp. 70–74, 2014.

**Conductive Interconnects with Self-Healing Ability**

- [57] S. J. Benight, C. Wang, J. B.H. Tok, and Z. Bao, "Stretchable and self-healing polymers and devices for electronic skin," *Progress in Polymer Science*, vol. 38, issue 12, pp. 1961–1977, 2013.

- 
- [58] B. C-K. Tee, C. Wang, R. Allen, and Z. Bao, “An electrically and mechanically self-healing composite with pressure- and flexion-sensitive properties for electronic skin applications,” *Nature Nanotechnology*, vol. 7, pp. 825–832, 2012.
- [59] B. J. Blaiszik, S. L. B. Kramer, M. E. Grady, D. A. McIlroy, J. S. Moore, N. R. Sottos, and S. R. White, “Autonomic restoration of electrical conductivity,” *Advanced Materials*, vol. 24, issue 3, pp. 398–401, 2012.
- [60] T. Koshi and E. Iwase, “Self-healing metal wire using an electric field trapping of gold nanoparticles for flexible devices,” *Proceedings of the 28th IEEE International Conference on Micro Electro Mechanical Systems (MEMS2015)*, pp. 81–84, 2015.
- [61] T. Koshi and E. Iwase, “Self-healing metal wire using electric field trapping of metal nanoparticles,” *Japanese Journal of Applied Physics*, vol. 54, no. 6S1, 06FP03 (6 pages), 2015.
- [62] T. Koshi and E. Iwase, “Particle Size Dependence on Self-Healing Metal Wire using an Electric Field Trapping of Metal Nanoparticles,” *Transactions of the Japan Society of Mechanical Engineers (in Japanese)*, vol. 82, no. 834, 15-00470 (10 pages), 2016.

### **Dielectrophoresis of Nanoparticles**

- [63] D. Cheon, S. Kumar, and G-H. Kim, “Assembly of gold nanoparticles of different diameters between nanogap electrodes,” *Applied Physics Letters*, vol. 96, issue 1, 013101(3 pages), 2010.
- [64] H. Ding, J. Shao, Y. Ding, W. Liu, X. Li, H. Tian, and Y. Zhou, “Effect of island shape on dielectrophoretic assembly of metal nanoparticle chains in a conductive-island-based microelectrode system,” *Applied Surface Science*, vol. 330, pp. 178–184, 2015.
- [65] L. Bernard, M. Calame, S. J. van der Molen, J. Liao, and C. Schönenberger, “Controlled formation of metallic nanowires via Au nanoparticle as trapping,” *Nanotechnology*, vol. 18, no. 23, 235202 (6 pages), 2007.
- [66] S. L. Leung, M. L. Li, and W. J. Li, “Formation of gold nano-particle chains by DEP – a parametric experimental analysis,” *Proceedings of the 3rd IEEE International Conference on Nano/Micro Engineered and Molecular Systems*, pp. 1033–1038, 2008.
- [67] W. Liu, C. Wang, H. Ding, J. Shao, and Y. Ding, “AC electric field induced dielectrophoretic assembly behavior of gold nanoparticles in a wide frequency range,” *Applied Surface Science*, vol. 370, pp. 184–192, 2016.

---

*References*

---

- [68] X. Xiong, A. Busnaina, S. Selvarasah, and S. Somu, "Directed assembly of gold nanoparticle nanowires and networks for nanodevices," *Applied Physics Letters*, vol. 91, issue 6, 063101(3 pages), 2007.
- [69] A. Bezryadin and C. Dekker, "Electric trapping of single conducting nanoparticles between nanoelectrodes," *Applied Physics Letters*, vol. 71, issue 9, pp. 1273–1275, 1997.
- [70] I. Amlani, A. M. Rawlett, L. A. Nagahara, and R. K. Tsui, "An approach to transport measurement of electronic molecules," *Applied Physics Letters*, vol. 80, issue 15, pp. 2761-2763, 2002.
- [71] J-S. Na, J. Ayres, K. L. Chandra, C. Chu, C. B. Gorman, and G. N. Parsons, "Conduction mechanisms and stability of single molecule nanoparticle/molecule/nanoparticle junctions," *Nanotechnology*, vol. 18, no. 3, 035203(8 pages), 2007.
- [72] R. Krahne, T. Dadosh, Y. Gordin, A. Yacoby, H. Shtrikman, D. Mahalu, J. Sperling, and I. Bar-Joseph, "Nanoparticles and nanogaps: controlled positioning and fabrication," *Physica E: Low-dimensional Systems and Nanostructures*, vol. 17, pp. 498–502, 2003.
- [73] S. Kumar, Y-K. Seo, and G-H. Kim "Manipulation and trapping of semiconducting ZnO nanoparticles into nanogap electrodes by dielectrophoresis technique," *Applied Physics Letters*, vol. 94, issue 15, 153104 (3 pages), 2009.
- [74] J. Lee, S. Mubeen, C. M. Hangarter, A. Mulchandani, W. Chen, and N. V. Myung, "Selective and rapid room temperature detection of H<sub>2</sub>S using gold nanoparticle chain arrays," *Electroanalysis*, vol. 23, no. 11, pp. 2623–2628, 2011.
- [75] K. Hoshino, K. Yamada, K. Matsumoto, and I. Shimoyama, "Creating a nano-sized light source by electrostatic trapping of nanoparticles in a nanogap," *Journal of Micromechanics and Microengineering*, vol. 16, no. 7, pp. 1285–1289, 2006.
- [76] Y. Hwang, H. Sohn, A. Phan, O. M. Yaghi, and R. N. Candler "Dielectrophoresis-assembled zeolitic imidazolate framework nanoparticle-coupled resonators for highly sensitive and selective gas detection," *Nano Letters*, vol. 13, no. 11, pp 5271–5276, 2013.
- [77] K. D. Hermanson, S. O. Lumsdon, J. P. Williams, E. W. Kaler, and O. D. Velev "Dielectrophoretic assembly of electrically functional microwires from nanoparticle suspensions," *Science*, vol. 294, issue 5544, pp. 1082–1086, 2001.
- [78] K. H. Bhatt and O. D. Velev, "Control and modeling of the dielectrophoretic assembly of on-chip nanoparticle wires," *Langmuir*, vol. 22, no. 2, pp. 467–476, 2004.

- 
- [79] R. Kretschmer, and W. Fritzsche, "Pearl chain formation of nanoparticles in microelectrode gaps by dielectrophoresis," *Langmuir*, vol. 20, no. 26, pp. 11797–11801, 2004.
- [80] J. N. Israelachvili, "Intermolecular and surface forces 3rd ed.," *Elsevier*, pp. 107–340, 2011.
- [81] T. B. Jones, "Electromechanics of Particles," *Cambridge University Press*, pp. 5–82, 1995.
- [82] R. J. Barsotti, Jr., M. D. Vahey, R. Wartena, Y.-M. Chiang, J. Voldman, and F. Stellacci, "Assembly of metal nanoparticles into nanogaps," *Small*, vol. 3, no. 3, pp. 488–499, 2007.
- [83] B. C. Gierhart, D. G. Howitt, S. J. Chen, R. L. Smith, and S. D. Collins, "Frequency dependence of gold nanoparticle superassembly by dielectrophoresis," *Langmuir*, vol. 23, no. 24, pp. 12450–12456, 2007.

#### **Crack Configurations of Metal Interconnect**

- [84] I. M. Graz, D. P. J. Cotton, and S. P. Lacour, "Extended cyclic uniaxial loading of stretchable gold thin-films on elastomeric substrates," *Applied Physics Letter*, vol. 94, issue 7, 071902 (3 pages), 2009.
- [85] O. Akogwu, D. Kwabi, S. Midturi, M. Eleruja, B. Babatope, and W. O. Soboyejo, "Large strain deformation and cracking of nano-scale gold films on PDMS substrate," *Material Science and Engineering: B*, vol. 170, issues 1-3, pp. 32–40, 2010.
- [86] O. Graudejus, Z. Jia, T. Li, and S. Wagner, "Size-dependent rupture strain of elastically stretchable metal," *Scripta Materialia*, vol. 66, issue 11, pp. 919–922, 2012.
- [87] I. R. Minev, P. Musienko, A. Hirsch, Q. Barraud, N. Wenger, E. M. Moraud, J. Gandar, M. Capogrosso, T. Milekovic, L. Asboth, R. F. Torres, N. Vachicouras, Q. Liu, N. Pavlova, S. Duis, A. Larmagnac, J. Vörös, S. Micera, Z. Suo, G. Courtine, and S. P. Lacour, "Electronic dura mater for long-term multimodal neural interfaces," *Science*, vol. 347, pp. 159–163, 2015.
- [88] T. Adrega and S. P. Lacour, "Stretchable gold conductors embedded in PDMS and patterned by photolithography: Fabrication and electromechanical characterization," *Journal of Micromechanics and Microengineering*, vol. 20, 055025 (8 pages), 2010.
- [89] Y-Y. Hsu, M. Gonzalez, F. Bossuyt, F. Axisa, J. Vanfleteren, and I. D. Wolf, "The effect of pitch on deformation behavior and the stretching-induced failure of a polymer-encapsulated stretchable circuit," *Journal of Micromechanics and Microengineering*, vol. 20, no. 7, 075036 (11 pages), 2010.

---

*References*

---

- [90] M. Gonzalez, F. Axisa, M. V. Bulcke, D. Brosteaux, B. Vandeveldel, and J. Vanfleteren, "Design of metal interconnects for stretchable electronic circuits," *Microelectronics Reliability*, vol. 48, issue 6, pp. 825–832, 2008.
- [91] I. D. Jhonston, D. K., McCluskey, C. K. L. Tan, and M. C. Tracey, "Mechanical characterization of bulk Sylgard 184 for microfluidics and microengineering," *Journal of Micromechanics and Microengineering*, vol. 24, no. 3, 035017 (7 pages), 2014.
- [92] R. D. Emry and G. L. Povirk, "Tensile behavior of free-standing gold films. Part II. Fine-grained films," *Acta Materialia*, vol. 51, issue 7, pp. 2079–2087, 2008.
- [93] S. Zhang, M. Sakane, T. Nagasawa, and K. Kobayashi, "Mechanical properties of copper thin films used in devices," *Procedia Engineering*, vol. 10, pp. 1497–1502, 2011.



## Achievements

### Journal Articles

- [1] **T. Koshi** and E. Iwase, “Crack-Configuration Analysis of Metal Conductive Interconnect Embedded in Elastomer,” *Micromachines*, vol. 9, issue 3, 130 (12 pages), 2018.
- [2] **T. Koshi**, Y. Nakajima, and E. Iwase, “Voltage and Current Conditions for Nanoparticle Chain Formation using Dielectrophoresis,” *Micro & Nano Letters*, vol. 12, issue 8, pp. 532–535, 2017.
- [3] **古志 知也**, 岩瀬 英治, “金属ナノ粒子の電界トラップを用いた自己修復型金属配線の粒径依存性,” *日本機械学会論文集*, vol. 82, no. 834, 15-00470 (10 pages), 2016.
- [4] **T. Koshi** and E. Iwase, “Self-Healing Metal Wire using Electric Field Trapping of Metal Nanoparticles,” *Japanese Journal of Applied Physics*, vol. 54, 06FP03 (6 pages), 2015. **【Selected for Spotlights of 2015, MNC 2015 Outstanding Paper】**

### Review Articles

- [5] **古志 知也**, 岩瀬 英治, “伸縮性電気配線および自己修復機能を有する金属配線,” *接着の技術*, vol. 37, no. 2, pp.21–25, 2017.
- [6] **古志 知也**, 岩瀬 英治, “自己修復型金属配線と伸縮デバイス応用,” *応用物理*, vol. 86, no. 12, pp. 1061–1064, 2017.

### Conference Proceedings (International Conference)

- [7] M. Kashiwagi, **T. Koshi**, E. Iwase, “High Performance Flexible Thermoelectric Device included Rigid Material,” *Proceedings of the 32th IEEE International Conference on Micro Electro Mechanical Systems (MEMS2019)*, Coex, Seoul, Korea, January 27–31, 2019.

- [8] **T. Koshi** and E. Iwase, “Stretchable Device with Repeat Self-Healing Ability of Metal Wire,” *Proceedings of the 30th IEEE International Conference on Micro Electro Mechanical Systems (MEMS2017)*, pp. 262-265, Las Vegas, Nevada, USA, January 22–26, 2017. **【Acceptance Rate (Oral): 9.0%】**
- [9] **T. Koshi** and E. Iwase, “Voltage and Current Condition on Self-Healing Metal Wire,” *Proceedings of the International Symposium on Micro-Nano Science and Technology 2016 (MNST2016)*, SuP2-B-3, Tokyo, Japan, December 16–18, 2016.
- [10] Y. Nakajima, **T. Koshi**, and E. Iwase, “Healing Process Behavior on Electric Field Trapping of Gold Nanoparticles,” *Proceedings of the International Symposium on Micro-Nano Science and Technology 2016 (MNST2016)*, SaP-2, Tokyo, Japan, December 16–18, 2016.
- [11] **T. Koshi** and E. Iwase, “Self-Healing Metal Wire using an Electric Field Trapping of Gold Nanoparticles for Flexible Devices,” *Proceedings of the 28th IEEE International Conference on Micro Electro Mechanical Systems (MEMS2015)*, pp. 81-84, Estoril, Portugal, January 18–22, 2015. **【Acceptance Rate (Oral): 9.0%, Selected for Outstanding Oral Paper Award Finalists】**
- [12] **T. Koshi** and E. Iwase, “Design and Fabrication of a Self-Healing Metal Wire using an Electric Field Trapping of Gold Nanoparticles,” *Proceedings of the 27th International Microprocesses and Nanotechnology Conference (MNC2014)*, 6C-4-3, Fukuoka, Japan, November 4–7, 2014. **【Acceptance Rate (Oral): 20%】**

#### Conference Proceedings (Domestic Conference)

- [13] 佐藤 峻, **古志 知也**, 岩瀬 英治, “粘着弾性体による押し付け圧力を利用した非加熱型電子部品実装手法の提案,” *日本機械学会 第9回マイクロ・ナノ工学シンポジウム*, 30am4-PN-58, 札幌, 北海道, October 30–November 1, 2018.
- [14] **古志 知也**, 岩瀬 英治, “繰り返し伸縮変形下における自己修復型金属配線の修復特性の評価,” *日本機械学会 第9回マイクロ・ナノ工学シンポジウム*, 30am3-PN-59, 札幌, 北海道, October 30–November 1, 2018.
- [15] **古志 知也**, 福家 加奈, 柏木 誠, 岩瀬 英治, “波形状金属配線と無機熱電素子を用いた伸縮性熱電発電デバイス,” *日本機械学会 第9回マイクロ・ナノ工学シンポジウム*, 30am3-PN-15, 札幌, 北海道, October 30–November 1, 2018.

- [16] 古志 知也, “自己修復型金属配線を用いた伸縮電子デバイス,” エレクトロニクス実装学会 関西支部 関西ワークショップ2018, 26, 吹田, 大阪府, July 12–13, 2018. **【Selected for インパクトポスター賞】**
- [17] 黄 平, 古志 知也, 岩瀬 英治, “金属ナノ粒子の電界トラップにおける電解質濃度による粒子流れの影響,” 電気学会 E 部門 総合研究会, MSS-18-22, 奈良, 奈良, July 12–13, 2018.
- [18] 武鎗 彰良, 古志 知也, 岩瀬 英治, “電界トラップによる金ナノ粒子の架橋構造における架橋形態の分類,” 日本機械学会 ロボティクス・メカトロニクス講演会, 1P2-L08, 北九州, 福岡, June 2–5, 2018.
- [19] 長村 透, 古志 知也, 岩瀬 英治, “高電圧条件下における誘電泳動力を用いたナノ粒子鎖形成,” 日本機械学会 関東支部第 24 期総会・講演会, OS0304, 調布, 東京, March 17–18, 2018. **【Selected for 若手優秀講演フェロー賞】**
- [20] 石井 智之, 古志 知也, 岩瀬 英治, “伸縮基板の剛性と波状金属配線の形状による配線の伸縮性の設計と評価” 日本機械学会 第 8 回マイクロ・ナノ工学シンポジウム, 01am2-PN-61, 広島, 広島, October 31–November 2, 2017.
- [21] 古志 知也, T. Löher, 岩瀬 英治, “伸縮基板上の波形状金属配線に生じるき裂の観察,” 日本機械学会 第 8 回マイクロ・ナノ工学シンポジウム, 31am3-PN-5, 広島, 広島, October 31–November 2, 2017.
- [22] 石井 智之, 朴 致済, 古志 知也, 岩瀬 英治, “伸縮電子デバイスのための金属部と基材部の剛性比を用いた伸縮耐性の向上” 日本機械学会 ロボティクス・メカトロニクス講演会, 1P2-K10, 郡山, 福島, May 10–13, 2017.
- [23] 黒木 雄也, 古志 知也, 岩瀬 英治, “伸縮基板上の金属配線におけるき裂の発生形態,” 日本機械学会 関東学生会 第 56 回学生員卒業研究発表講演会, 1315, 葛飾, 東京, March 16, 2017.
- [24] 朴 致済, 石井 智之, 古志 知也, 岩瀬 英治, “金属配線と伸縮基板の剛性比を用いた伸縮耐性の設計” 日本機械学会 関東学生会 第 56 回学生員卒業研究発表講演会, 1312, 葛飾, 東京, March 16, 2017.
- [25] 細谷 航平, 古志 知也, 岩瀬 英治, “金属ナノ粒子の電界トラップを用いた配線修復における周波数依存性” 日本機械学会 関東学生会 第 56 回学生員卒業研究発表講演会, 1309, 葛飾, 東京, March 16, 2017.

---

*Achievements*

---

- [26] 井筒 栄佑, 古志 知也, 岩瀬 英治, “銅ナノ粒子の電界トラップを用いた金属配線の自己修復,” 日本機械学会 関東学生会 第 55 回学生員卒業研究発表講演会予稿集, 目黒, 東京, March 10, 2016.
- [27] 古志 知也, 中島 雄太, 岩瀬 英治, “金属ナノ粒子の誘電泳動を用いた自己修復型金属配線における修復過程の直接観察,” 化学とマイクロ・ナノシステム学会 第 32 回研究会 予稿集, 1P11, 北九州, 福岡, November 26–27, 2015.
- [28] 古志 知也, 岩瀬 英治, “伸縮変形で生じた配線き裂の自己修復,” 日本機械学会 第 7 回マイクロ・ナノ工学シンポジウム 予稿集, 29pm1-F-3, 新潟, October 28–30, 2015. **【Selected for 若手優秀講演表彰】**
- [29] 中島 雄太, 古志 知也, 岩瀬 英治, “金属ナノ粒子の電界トラップ中の粒子挙動解析,” 日本機械学会 第 7 回マイクロ・ナノ工学シンポジウム 予稿集, 28am2-E-5, 新潟, October 28–30, 2015.
- [30] 辛島 龍彦, 古志 知也, 岩瀬 英治, “電解めっきを利用した自己修復機能を有する金属配線,” 日本機械学会 関東学生会 第 54 回学生員卒業研究発表講演会 予稿集, 1101, 横浜, 神奈川, March 20, 2015.
- [31] 古志 知也, 岩瀬 英治, “金ナノ粒子の電界トラップを用いた自己修復配線における粒径依存性,” 日本機械学会 第 6 回マイクロ・ナノ工学シンポジウム 予稿集, 21pm1-A3, 松江, 島根, October 20–22, 2014.
- [32] 古志 知也, 岩瀬 英治, “金ナノ粒子の電界トラップを用いた自己修復型伸縮配線,” 日本機械学会 関東学生会 第 53 回学生員卒業研究発表講演会 予稿集, 606, 小金井, 東京, March 14, 2014.

**Book Chapters**

- [33] 岩瀬 英治, 古志 知也, “自己修復型金属配線の開発とウェアラブル機器への応用可能性,” in “ウェアラブルデバイスの小型、薄型化と伸縮、柔軟性の向上技術,” pp. 146–154 (第 2 章 第 6 節), 技術情報協会, December 25, 2015.

**Patents**

- [34] E. Iwase, T. Koshi, “Self-Repairing Wiring and Stretchable Device,” 国際出願番号 PCT/JP2015/054888 (February 21, 2015), 国際公開番号 WO2015/125944 (August 27, 2015).
- [35] 岩瀬 英治, 古志 知也, “自己修復型伸縮配線及び伸縮デバイス,” 特願 2014-032182, February 21, 2014.

**Awards**

- [36] 古志 知也, “インパクトポスター賞,” エレクトロニクス実装学会 関西支部 関西ワークショップ2018, July, 2018. **【Acceptance Rate: 8.5%】**
- [37] 古志 知也, “若手優秀講演表彰,” 日本機械学会 マイクロ・ナノ工学部門, December, 2016. **【Acceptance Rate: 3.6%】**
- [38] 古志 知也, “三浦賞,” 日本機械学会, March, 2016. **【Acceptance Rate: Approximately 3%】**
- [39] 古志 知也, “小野梓記念学術賞,” 早稲田大学, March, 2016. **【Acceptance Rate: Approximately 0.06%】**
- [40] T. Koshi, E. Iwase, “MNC 2014 Outstanding Paper,” *27th International Microprocesses and Nanotechnology Conference (MNC2014)*, November, 2015. **【Acceptance Rate: 0.3%】**
- [41] T. Koshi, “Outstanding Oral Paper Award Finalists,” *IEEE International Conference on Micro Electro Mechanical Systems (MEMS2015)*, January, 2015. **【Acceptance Rate: 1.5%】**

## Acknowledgements

This thesis consists of works conducted at Micro and Nano Mechanics Laboratory, Department of Applied Mechanics, Graduate School of Fundamental Science and Engineering, Waseda University. Here, I would like to express my sincere appreciation to those who were involved in this research.

I would like to highlight my deep appreciation for the support from my supervisor, Prof. Eiji Iwase. This research could not have been established without help from him; I learned several things—those characteristics that are necessary for being a professional researcher—from him. In the future, based on these learnings, I would like to contribute to society through my research.

I also would like to thank Prof. Hiroyuki Kawamoto and Prof. Jun Tomioka for their comments and helpful discussions. I also could not have drafted this thesis without their help.

The Graduate program for Embodiment Informatics, Waseda University, has supported me with several things, such as the grant for the overseas internship program. Owing to this program, I received the valuable opportunity to interact with many people from other countries. I would like to thank all professors, staff, and my friends in this program. In particular, the experience with my friends in this program helped me grow considerably. I look forward to their continued success.

I would like to acknowledge Dr. Thomas Löher and his colleagues at Fraunhofer IZM for their support and valuable discussions on this research. The research stay at Fraunhofer IZM from April to July, 2017, was a wonderful experience for me.

I also would like to thank all members at Micro and Nano Mechanics Laboratory for their support. They gave me considerable help in the experiments and helped me with the necessary procedures for my research activities. I also look forward to their continued success.

This research was partially supported by Grant-in-aid for JSPS Fellows (Grant Number: 16J10143), JSPS KAKENHI (Grant Number: 16KT0107), and JST CREST (Grant Number: JPMJCR16Q5). In addition, I would like to thank the MEXT Nanotechnology Platform Support Project of Waseda University.

---

*Acknowledgements*

---

Finally, I would like to express my most sincere thanks to my parents, Toshinori and Hiromi, their ongoing and sacrificial support throughout my life, and I would like to express my deepest gratitude to my wife, Chihiro.

January 2019

Tomoya Koshi